28

IS-T-1832

The Structure-property Relationships of Powder Processed Fe-Al-Si Alloys

by

Prichard, Paul D.

PHD Thesis submitted to Iowa State University

Ames Laboratory, U.S. DOE

Iowa State University

Ames, Iowa 50011

Date Transmitted: February 23, 1998

PREPARED FOR THE U.S. DEPARTMENT OF ENERGY

UNDER CONTRACT NO. W-7405-Eng-82.

DISCLAIMER

DEDICATION

To Dawn, the best partner a man could have.

TABLE OF CONTENTS

ABSTRACT

Iron-aluminum alloys have been extensively evaluated as semi-continuous product such as sheet and bar, but have not been evaluated by net shape P/M processing techniques such as metal injection molding. The alloy compositions of iron-aluminum alloys have been optimized for room temperature ductility, but have limited high temperature strength. Hot extruded powder alloys in the Fe-Al-Si system have developed impressive mechanical properties, but the effects of sintering on mechanical properties have not been explored. This investigation evaluated three powder processed Fe-Al-Si alloys: Fe-15Al, Fe-15Al-2.8Si, Fe-15Al-5Si (atomic%). The powder alloys were produced with a high pressure gas atomization (HPGA) process to obtain a high fraction of metal injection molding (MIM) quality powder (D_{84}< 32μm). The powders were consolidated either by P/M hot extrusion or by vacuum sintering. The extruded materials were near full density with grain sizes ranging from 30 to 50 μm. The vacuum sintering conditions produced samples with density ranging from 87% to 99% of theoretical density, with an average grain size ranging from 26 μm to 104 μm. Mechanical property testing was conducted on both extruded and sintered material using a small punch test. Tensile tests were conducted on extruded bar for comparison with the punch test data. Punch tests were conducted from 25°C to 550°C to determine the yield strength, and fracture energy for each alloy as a function of processing condition. The ductile to brittle transition temperature (DBTT) was observed to increase with an increasing silicon content. The Fe-15Al-2.8Si alloy was selected for more extensive testing due to the combination of high temperature strength and low temperature toughness due to the two phase α + DO_3 structure. The extruded material developed higher yield strength at temperatures below the DBTT, but the sintered material developed higher strengths above the DBTT. The fracture energy of these alloys was higher at all test temperatures, which indicated the importance of grain size and pore interaction with crack propagation. This investigation provided a framework for understanding the effects of silicon in powder processing and mechanical property behavior of Fe-Al-Si alloys.

CHAPTER 1. INTRODUCTION

Background

Iron-aluminum alloys have been explored as engineering materials due to the unique combination of low cost raw materials, and environmental resistance in high temperatures. In the past 15 years, a large effort has been directed toward the development of Fe-Al alloys as a cast and wrought semi-finished product for potential replacement for stainless steels [1]. Unfortunately, a number of Fe-Al alloy compositions showing good high temperature strength were excluded due to incompatibility with cast and wrought processing. The rapid solidified processing of powders by inert gas atomization produces minimal microsegregation in the microstructure, and therefore powder processing offers considerably more flexibility in alloy design compared to the cast and wrought processing approach [2]. Although powder processing of Fe-Al alloys has been explored, the compositions examined were based on the alloys optimized for conventional cast and wrought processing [3].

Previous powder processing investigations of Fe-Al have used hot isostatic pressing (HIP) and hot extrusion as the consolidation techniques [1]. However, very little research has been conducted on the sintering behavior of iron aluminum based alloys, and the effects of sintered microstructures on the mechanical properties of those alloys. In addition, combining powder processes such as gas atomization and metal injection molding (MIM) present opportunities to manufacture net shape parts for higher temperatures. Since workability is not a criteria for MIM parts, ternary alloy additions such as silicon and titanium may be used, which have shown potent strengthening effects at room temperature and elevated temperature [4,5]. Figure 1.1 shows the yield strength developed in hot extruded powders of Fe-28Al-2Cr, compared to the yield strength of hot extruded material with a composition of Fe-15Al-5Si-1Ti-2B. The Fe-Al-Cr alloy composition was optimized for ductility, but the Fe-Al-Si-Ti-B alloy was designed for strength.. Boggs [6] has shown improvement the oxidation of Fe-Al alloys with the addition of 2.0 % atomic silicon by forming a tenacious silicon oxide film. In addition to the effects on mechanical properties, the effects of ternary alloy additions must be evaluated by powder processing criteria such as sinterability and grain size stability. This investigation examines silicon additions of 2.8 at.% and 5.0 at.% to a base alloy of Fe-15Al at%. on the initial atomized powder microstructure, the microstructural evolution during vacuum sintering, and the mechanical properties of vacuum and hot extruded material. These data demonstrate the viability of Fe-Al-Si alloys for the MIM process.

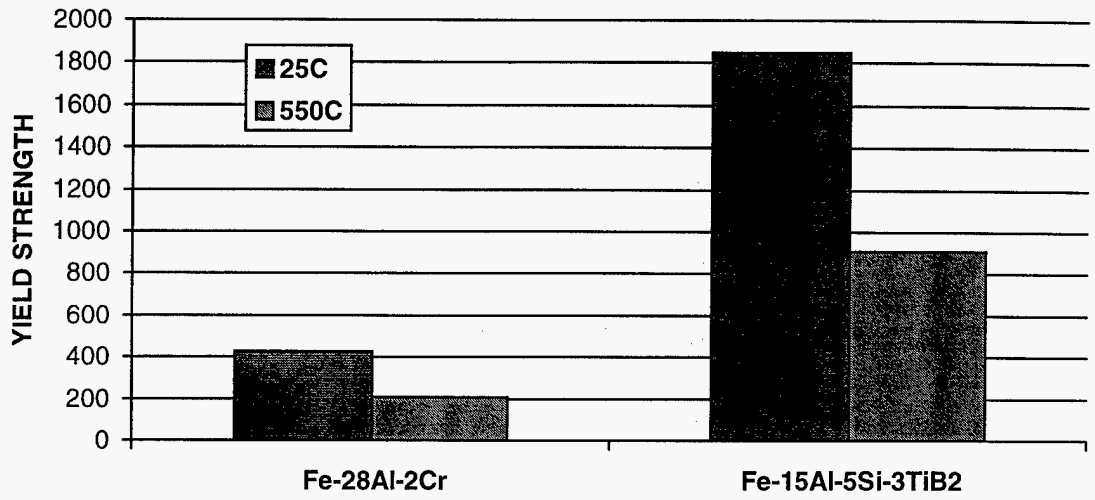

Figure 1.1 - Comparison of yield strength in P/M hot extruded Fe-Al alloys [1,6]

Iron Aluminum Alloys

Many research investigations have been conducted on iron aluminum alloys to understand the effects of the phase equilibrium, alloying, processing on the mechanical and physico-chemical properties. McKamey et al [1] have published an extensive review of this research. The most attractive features iron aluminum alloys are the abundance and low cost of the raw materials and good oxidation resistance in air to temperatures up to 1000°C. However, the use of Fe-Al alloys as structural materials has been limited by the inherent lack of ductility at room temperature, and the strength at temperatures above 500°C. Significant progress has been made in the past 10 years at Oak Ridge National Laboratories in the fundamental understanding of iron aluminides, and the development of reasonable room temperature ductility (15% elongation) with the addition of 2 at.% to 5 at.% chromium [1,7,8]. The improvement of the high temperature strength of these alloys is currently being explored. Therefore, a major challenge still remains to balance the room temperature toughness and the high temperature strength above 500°C.

A good model for the balance of low temperature toughness and high temperature strength has been achieved in nickel base superalloys by producing a high volume fraction intermetallic phase Ni_3Al in a ductile nickel matrix. Commercial nickel based superalloys contain from 20% to 60% volume fraction of Ni3Al [9]. Similarly, two phase structures of ordered Fe_3Al can be produced in a matrix of solid solution strengthened iron. However, the phase stability are different in the Fe-Al system compared to the Ni-Al system. Since the Fe_3Al phase disorders at 550°C, ternary additions

are required to produce two phase alloys, which are at equilibrium at 600°C. Previous investigations which examined phase equilibrium in the Fe-Al binary system will provide guidance for interpretation of ternary alloys. Therefore, the work on the binary system will be briefly reviewed.

Fe-Al Phase Equilibrium

A number of investigators have developed data on the phase equilibrium of Fe-Al system. The most accepted binary phase diagram published by the American Society for Metals [10] is shown in Figure 1.2. The order-disorder transformation of Fe_3Al from the $D0_3$ compound to the B2 crystal structure was determined by Swann, Fisher and Duff [11]. The phase diagram shows the aluminum solubility in the BCC α-iron up to 18 atomic %. A region of short range order described as $Fe_{13}Al_3$ was believed to exist between 18 at.% and 20.5 at.%. At compositions between 20.5 and 24 at.%, a two phase region of α + DO_3 (α') exists up to 400°C where the α' dissolves into disordered BCC α. The α' phase region exists from 24% to 28% atomic aluminum up to 550°C, where it transforms completely to a "psuedo-FeAl" B2 phase (β), and into a above 700°C. A two phase region α' + β exists between 28% and 33% atomic aluminum, which transforms into β above 400°C. The β region extends from above 33% to 52% atomic aluminum, and the β phase is ordered B2 up to the melting point.

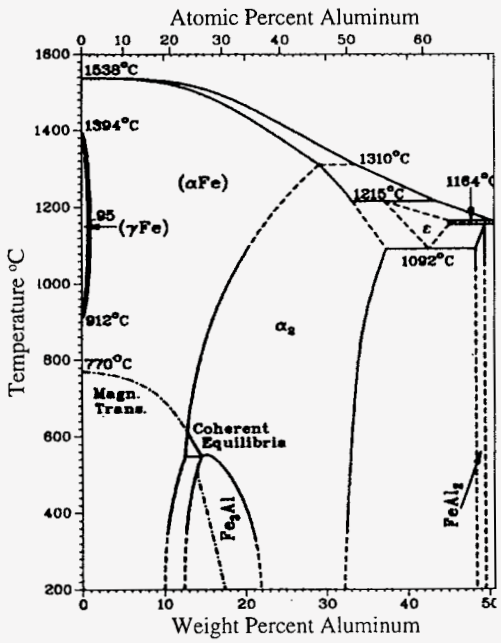

Figure 1.2 - Fe-Al Phase Diagram [7]

Order-disorder Transitions

X-ray diffraction and electron diffraction have been used most effectively to study the phase equilibrium in Fe-Al based alloys. Taylor and Jones [12] and Lawley and Cahn [13] used hot stage x-ray diffraction to study the phase equilibrium in Fe-Al. The ordered domain size was approximated by peak broadening. Swann, Duff and Fisher [11] conducted the most comprehensive TEM investigations of the order-disorder reactions in Fe-Al. The advantage of this technique was the direct observation of the ordered domains, anti-phase boundaries and deformation mechanisms. Cahn and Allen [14] were able to observed the difference between a coherent and incoherent transformation at grain boundaries and grain interiors. The use of dark field imaging with reflections from the superlattice allow the direct observation of phase relationship. The systematic reflections and absences are predicted by the structure factor calculation, which is a summation of the scattered waves of electromagnetic radiation diffracted in a material given by equation [1.1]. For a given (hkl), the structure factor predicts whether a reflection is present or absent for those planes [15].

$$F_{hkl} = \sum_{1}^{N} f_n e^{2\pi i(hu_n + kv_n + lw_n)} \qquad [1.1]$$

The unit cell is based on Fe_3Al for the description of the planes is shown in Figure 1.3, which has face centered symmetry and approximately twice the lattice parameter of pure iron.

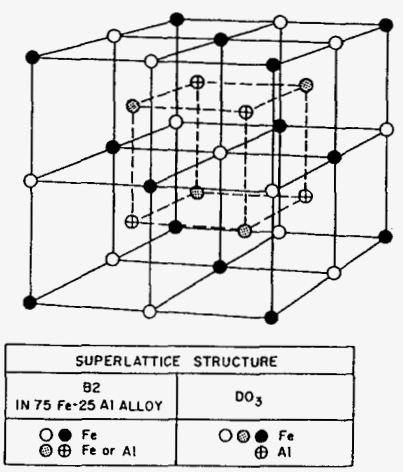

Figure 1.3 - Crystal structure of FeAl (B2) and Fe_3Al (DO_3) [21]

Effect of Silicon

Fe_3Si and Fe_3Al are isomorphous compounds which both contain the DO_3 structure [16]. A pseudo-binary of the compounds is shown in Figure 1.4. The Fe_3Si is more strongly ordered, since ordering is observed up to the melting temperature of 1250°C. However, these materials are extremely brittle and do not have structural use. The increased temperature stability of the DO_3 $Fe_3(Al,Si)$ phase has been examined by Miyazaki et al [17]. Figure 1.5 shows the phase equilibrium for Fe-Al-Si system at 600°C (873 K). These phase equilibrium diagrams will be used for reference to design alloys and heat treatments for this investigation.

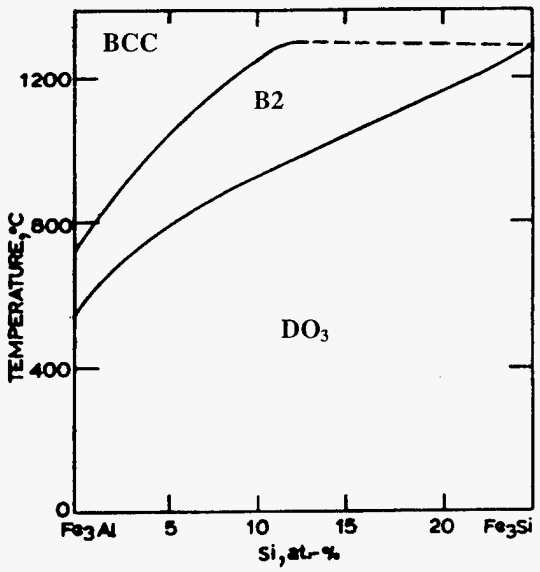

Figure 1.4- Pseudo-binary of Fe_3Al-Fe_3Si [17]

Miyazaki et al. used TEM analysis of isothermally heat treated samples to construct the iron-rich portion of the ternary Fe-Al-Si phase diagram shown in Figure 1.5 [17]. Morris and Gunther [18] demonstrated the phase stability of a new class of iron based superalloys using the order-disorder phases in Fe-Al-Si alloys. The basis for the alloy design in the Fe-Al-Si system is analogous to the alloy design used in nickel base superalloys; where an ordered intermetallic compound Ni_3Al comprises a large volume fraction (50%) in a ductile face-centered cubic matrix . For comparison, the Fe-Al-Si alloys develop an ordered $Fe_3(Al,Si)$ phase (DO_3), which can act to reduce dislocation mobility through a body centered cubic α-iron matrix. The addition of silicon stabilizes the ordered phase to higher temperatures, and broadens the composition range of the two phase field (α+DO_3).

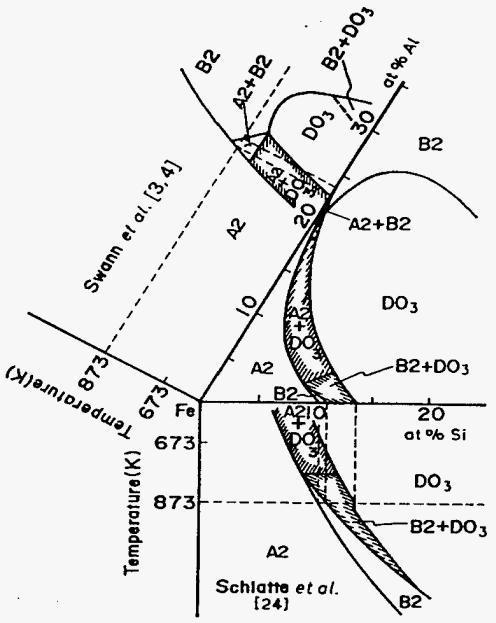

Figure 1.5 - Ternary Equilibrium Diagram of Fe-Al-Si [18]

BCC Deformation

Christian [19,20] reviewed the plastic deformation in BCC metals, which is the foundation to understanding the interaction between α and DO_3. The primary slip systems in iron are on the {110} {112} and {321} planes with a [111] slip direction. The macroscopic slip lines along {321} and irrational planes have been shown to consist of {110} and {112} segments. The elastic anisotropy in BCC metals reveals the preference to slip along particular planes. The anisotropy ratio of elastic constants, $A = 2C_{44}/(C_{11} - C_{12})$, demonstrates the range of elastic anisotropy observed in pure BCC metals. An "A ratio" equal to 1.0 shows no anisotropy, such as in tungsten. Iron has an "A ratio" equal to 2.4, shows a preference for {110} slip. However, BCC metals such as niobium have an "A ratio" less than 1.0, and the primary slip plane has been observed as {100}. The elastic anisotropy is an important consideration in determining the elastic stress field surrounding the core of the dislocation. The local stress field determines the lattice friction stress, which offers resistance to dislocation motion. The yield stress of BCC metals has been observed to be higher in single crystals oriented in the <110> direction compared to the <100> orientation [19]. Schmid's law of critical resolved shear stress has been observed to predict slip planes at higher temperatures in tension, but low temperature behavior has been more unpredictable.

Screw Dislocations

Typically, the edge dislocations are mobile on the slip planes, but the screw dislocations require cross slip onto other planes for mobility [19]. The core of the screw dislocation has been determined to be composed of three partial dislocations with 120° angular separation from each other on the {110} or {112} planes. The extensive cross slip required for screw dislocation mobility is observed on the macroscopic surface as "wavy slip" lines. At low temperatures < 0.15 T_m, the mobility of screw dislocations decreases and the flow stress increases. These characteristics are dependent on the anisotropy ratio and the melting point of the metal. At room temperature pure iron easily deforms due to easy cross slip of screw dislocations. The flow stress increases at liquid nitrogen temperatures (77K) due to the limited cross slip of the screw dislocations. Solid solution atoms or interstitial atoms in iron can substantially increase the flow stress of dislocations, which is reflected by an increase in the yield strength and an increase in the ductile to brittle transition temperature (DBTT). The substitutional or interstitial atoms produce short range elastic stress field which interact with the dislocation to reduce mobility. The increase in DBTT is a measure of the thermal activation required to overcome the solute atom with the dislocation. A more thorough description of the effect on flow stress and the effects on DBTT will follow.

Strengthening Mechanisms

The concentration of solute atoms, c, the shear modulus of the lattice, G, and the misfit strain of a solute atom, ε_s, produce an increase in the shear stress required to move a dislocation. The silicon and aluminum in solid solution iron produce a strengthening effect described by equation [1.2] which was developed by Fleischer [21]. The misfit strain can be calculated by using the difference in the atomic volume, Ω, between the solvent and solute atom.

$$\Delta\tau_{sol} = \frac{G\varepsilon_s^{3/2}c^{1/2}}{700} \qquad [1.2]$$

The size and distribution of the intermetallic phases determined the interaction with dislocations. The small ordered precipitates in as-extruded Fe-15Al-2.8Si could be treated as small particles, which may be by-passed or cut. The increase in shear stress required to bow around a dislocation around immobile objects is given by equation [1.3], where L is the interparticle distance and r is the particle radius [21].

$$\Delta\tau_B \cong \frac{Gb}{(L-2r)} \qquad [1.3]$$

Order strengthening results from the shear stress required to cut through an ordered intermetallic compound given by equation [1.4]. The energy create by a dislocation passing through a particle is a function of the cross sectional area, f, of the particles, and the anti-phase boundary energy (APBE) of the slip plane through the intermetallic phase [21]. These measurements require extensive TEM analysis with good knowledge of the foil thickness and diffraction conditions.

$$\Delta\tau_{ord} = \frac{\pi(APBE)f}{2b} \qquad [1.4]$$

DO_3 Deformation

Leamy [22] investigated 6 possible partial dislocation structures which could exist in Fe_3Al. Compression experiments on single crystal and polycrystalline samples were conducted to measure the critical resolved shear force with various compositions as a function of temperature. He concluded that only two types were energetically favorable. He also calculated the energy required to move these dislocation through the lattice as various degrees of order. Since the aluminum present has a solid solution hardening potential, the differential between a completely disordered an fully ordered material was taken into account. The movement of dislocations through a Fe_3Al precipitate required an increase in energy related to the bonding energy between first and second nearest neighbor on the slip plane of interest. The deformation and strength of these alloys results from the dislocations, which can exist in each crystal structure. The disordered a with 16% atomic aluminum undergoes the same slip phenomena observed BCC iron along the close packed (110), (112) and (123) planes. However, the ordered structure requires pairs of dislocations during deformation to preserve the nearest neighbor arrangement between iron and aluminum atoms. The DO_3 contains a number of possible superdislocations pairs shown in Figure 1.6 [22]. As temperature increases, more slip systems become active, cross slip occurs, and a polycrystalline sample exhibits plasticity. The two phase alloy of $\alpha + DO_3$ at 24 at.% aluminum develops very high yield strengths due to the interaction of dislocations between the ordered and disordered phases. As temperature increases more slip systems become active and the DO_3 disorders into α, which results in comparable yield stress to the Fe-16Al at.% alloy at 600°C. The effect of the degree of long range order on flow stress

Fe_3Al was examined by Stoloff and Davies [23] and is shown in Figure 1.7. If the second phase were stable at higher temperatures, the increase in yield strength observed at room temperatures would persist at higher temperatures.

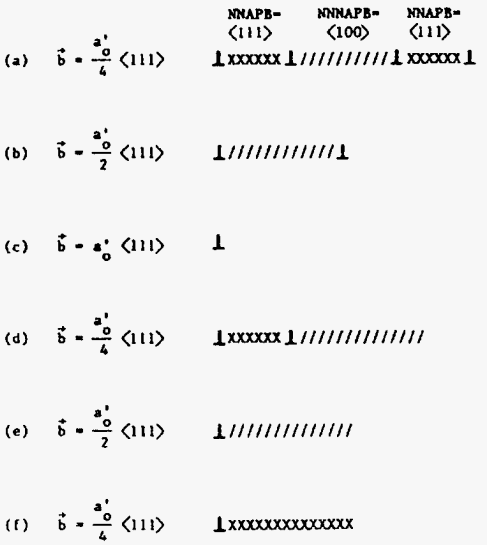

Figure 1.6 - Superdislocations which can exist in DO_3 and B2 Superlattices [22]

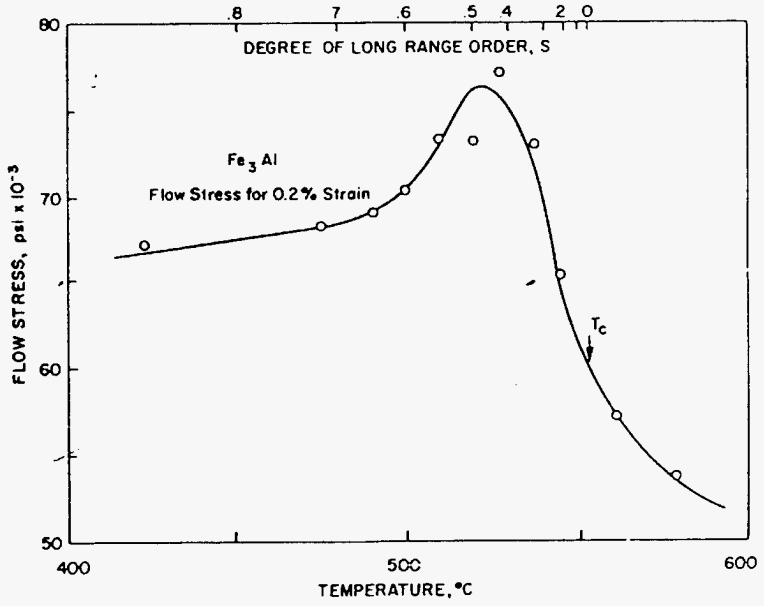

Figure 1.7- Flow stress of Fe_3Al at test temperature [23]

ORNL conducted experiments mechanical properties of cast and warm rolled Fe-Al binary alloys. The yield strength of binary iron aluminum alloys ranging from 16 at.% 35 at.% aluminum as a function of temperature [24] are shown in Figure 1.8. The alloy with 16 at.% aluminum has a moderate yield strength of 500 MPa at room temperature, and the yield strength decreased to about 300 MPa before falling off above to 150 MPa at 700°C. The alloy with Fe-24 Al atomic percent aluminum (13.2 wt.%) has a two phase structure of $\alpha + DO_3$, which shows the highest yield strength of 780 MPa at room temperature. The yield strength continuously decreases from 750 MPa at 200°C to 300 MPa at 600°C as the ordered DO_3 (α') continuously transforms to the disordered BCC–α. The two alloys which are single phase DO_3 with 28 to 30 atomic % aluminum (15.8% to 17.2% wt.) have the lowest yield strength at room temperature and elevated temperature. The alloy with 35 atomic % Al showed an intermediate strength at 480 MPa from room temperature to 400°C with a slight decrease to 430 MPa at 600°C before falling off at higher temperatures.

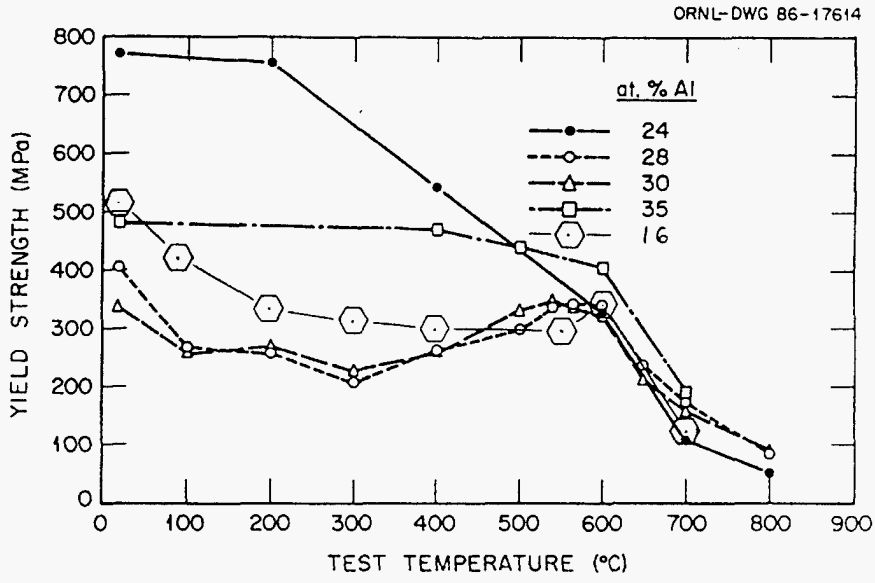

Figure 1.8 - Yield Strength as a function of temperature for binary Fe-Al Alloys [24]

Powder Processing

Powder processing methods have produced fine grain sizes (<10 μm), which increases the yield strength and fracture toughness of a material [25]. However, the powder processing techniques of iron aluminide alloys has been limited to hot extrusion and HIP. Figure 1.1 shows the wide range of properties which can be developed with iron-aluminum alloys, which have been hot extruded. An

alloy developed by Oak Ridge National Laboratory with a nominal composition of Fe-28Al-2Cr had a room temperature yield strength of 400 MPa, but a ductility of 15% elongation. Powell and researchers at Ohio State University produced rapidly solidified powders of an alloy with Fe-15Al-5Si + 3 vol% TiB_2. This alloy had a room temperature yield strength of 1850 MPa, but a ductility of only 5% elongation. While hot extrusion and HIP are the best processing techniques to achieve full density, the mechanical properties generated from these materials do not reflect those produced by low cost net shape processing, such as inert gas atomization, metal injection molding MIM and pressureless sintering. Each powder alloy needs to be evaluated to develop sintering process parameters for densification and the control of grain size for optimum properties. The mechanical properties resulting from the defects inherent in sintered powder processing such as porosity, prior particle boundaries and exaggerated grain growth must be evaluated in comparison to the hot extruded material.

P/M Hot Extrusion

Powder extrusion is the most effective method for producing full density bulk samples of powder materials, which is the reason powder extrusion is used to produce forging mults for turbine engine disks [26]. The extrusion process not only consolidates the powder, but the shear stresses on the powder surface breaks up the surface oxide inherent in high aluminum content alloys. Therefore, the potential of oxide inclusions as fracture initiation sites is minimized in the extruded orientation. The powder extrusion process has been used extensively by NASA, Oak Ridge National Laboratory and the Air Force Materials Laboratory for the consolidation of intermetallic powder alloys instead of HIP, because of the advantageous prior particle boundary distribution [3]. Since the materials are fully dense and develop fine recrystallized grains, the mechanical properties of the extruded powder alloys are expected to represent the best achievable properties from powder processing. However, a consequence of the large deformation along the extrusion direction is the development of a crystallographic texture. The texture aligns the slip planes along the extrusion axis, and typically increases the yield strength of the extruded material in the extruded orientation relative to a randomly oriented material.

Texturing is a well characterized phenomena in the working of iron alloys. Barret and Levinson [27] demonstrated the development of the {110} wire texture with the swaging of single crystal iron. Leber [28] measured a [100] circumferential texture in BCC wire by x-ray diffraction in addition to the {110} wire texture. Similar results have been reported by Khadkikar and Vedula [29] during the hot extrusion of Fe-40Al. Stout [30] reported two different textures for hot

extruded and recrystallized Fe-35Al, which developed depending on whether the starting material was powder or was a cast ingot. They examined the recrystallization textures by x-ray diffraction and orientation image mapping using the SEM technique of Dingly [31]. The powder developed a {110} texture, while the cast ingots developed a {111} texture. The major differences in the recrystallization behavior were due to the interaction of the grain boundaries with prior particles boundaries in the powder.

Metal Injection Molding

The sintering process is an important commercial process for the densification of parts made from powder metal forming processes such as metal injection molding (MIM). German [32] has written extensively on the MIM process, which will be now briefly summarized. The MIM process produces near net shape parts using a mixture of 60%-75% metal or ceramic powder with the remainder from a polymer binder. The mean powder particle diameter for MIM is typically less than 20 μm to provide a high surface area, which enhances good sinterability. A typical binder consists of a blend of a low molecular weight polymer, such as 85% paraffin wax, and a 15% of a higher molecular weight polymer, such as polyethylene. The powder and binder mixture is mechanically blended to provide a uniform feedstock for the MIM process. The feedstock is heated above the melting temperature of the binder, so the feedstock easily flows into a complex shaped cavity in a metal die. The polymer component solidifies in the injection die to form the net shape part, which is ejected for further processing. The polymer binders are removed by a dissolving them with an organic solvent or by thermal combustion and vaporization in a furnace from 300°C to 600°C. Binder selection and debinding processing is critical to produce parts with minimal carbon or oxygen contamination from the organic binders or furnace environment. Recently, vacuum debinding and vacuum sintering have been demonstrated to produce no discernible contamination in ferrous alloys [33].

The packing density of spherical powders has been shown to have comparable density to a MIM feedstock mixture [34]. Therefore, the powder packing density and sintering conditions for MIM processing can be simulated independently of binder compatibility studies to isolate alloying effects from debinding issues. The vacuum sintering of these clean tap dense powders represents the least contamination achievable, and the mechanical properties would represent optimum levels for sintered powder structures.

Sintering

The sintering process exposes a powder compact at a high temperature (>0.8T_m) to promote diffusion between adjacent particles to eliminate the porosity and produce a dense part with good mechanical integrity. The initial driving force during the sintering of fine powders are capillary effects from powder surface curvature and the high surface energy associated with the large free surface area of fine powders. The curvature at the interface of touching particles creates a driving force for neck creation. The classic Gibbs-Thompson [35] relationship in equation [1.5] describes the change in chemical potential of vacancies, μ, as a function of surface energy, γ_{SV} , atomic volume, Ω, and the radii of surface curvature, R_1 and R_2. The initial stage sintering models describe the neck formation in the early stages of sintering by the minimization of curvature at touching particles. The initial stage of sintering is dominated by surface diffusion and little densification occurs during this stage.

$$\mu = \gamma_{SV}\Omega\left(\frac{1}{R_1 + R_2}\right) \qquad [1.5]$$

The intermediate stage at the theoretical densities ranging from 65% to 92% accounts for the majority of the densification. The free surface energy driving force is due to the difference between the surface energy in the solid-vapor (γ_{SV}) and the grain boundary energy (γ_{GB}) created as the particles sinter together. Grain boundary and lattice diffusion are the major mechanisms removing vacancies to the exterior of the compact for consolidation. The change in volume due to vacancy transport from the internal pores to the external surface is described by equation [1.6] developed by German [35]. The sintering rate during the intermediate stage is strongly governed

$$\frac{\partial V_s}{\partial t} = \frac{g\gamma_{SV}\Omega D_V}{kTG^3 t} \qquad [1.6]$$

by the grain size, G. An increase in temperature, T, reduces the γ_{SV}, but exponentially increases the volume diffusion, D_v, which has the overall effect of increasing the sintering rate. Equation [1.6] also shows the sintering rate diminishes with an increasing the isothermal sintering time, t, due to the decrease curvature at powder necks and a decreases surface area. The final sintering stages are heavily dependent on grain boundary diffusion to eliminate the last pores. However, grain growth can occur during the final stage, which the grain boundaries move through pores and leave them

isolated in the grain interior. Isolated pores must be eliminated by lattice diffusion, which is 2-3 orders of magnitude less than grain boundary diffusion [36]. If these pores contain trapped gas from the sintering atmosphere, the pores are stabilized by the internal gas pressure and they will remain in the structure.

Surface Energy

As stated earlier, the surface energy is the predominant driving force for sintering, and therefore must be carefully considered during the examination of sintering phenomena. The mean grain boundary energy, γ_{GB}, is approximately 0.3 of the mean solid-vapor free energy, γ_{SV}, in most metals [37]. If the grain size remains the same as the initial powder size after consolidation, the surface energy of the compact is reduced approximately 70%. The γ_{SV} and the γ_{GB} are dependent on anisotropic properties of the crystal structure, and therefore both energies have different values as a function of crystal orientation at the solid-vapor interface or at the grain boundary. A Gibbs-Wulff surface energy plot can be constructed based on theoretical calculations or direct measurement. The change in surface energy an be calculated by accounting for the number of broken bonds along the plane of interest. This is easier for a pure metal than a multi-component alloy, since the bond energy between similar atoms are known, and local surface chemistry effects are predictable. Sundquist [38] developed a stereographic triangle for pure BCC metals, and experimentally determined the relative γ_{SV} as a function of planar orientation using the proportionality between surface energy and crystal dimension shown in equation [1.7].

$$\frac{d_{hkl}}{d_{HKL}} = \frac{\gamma_{hkl}}{\gamma_{HKL}} \qquad [1.7]$$

Sundquist [38] measured the dimensions of single grain particles on the order of 1 μm by TEM shadow graphs, and used the Wulff construction to determine the relative surface energies shown in Figure 1.9. This technique is tedious and quite difficult to prevent environmental interactions from affecting the results. It is important to recognize that while the γ_{SV} and γ_{GB} describe different quantities, the crystallographic relationships of γ_{SV} and the γ_{GB} are related by the nearest neighbor bond energy of the lattice. Therefore, alloys and ordered compounds may modify the surface energy orientation dependence when compared to the pure metal which is the primary constituent.

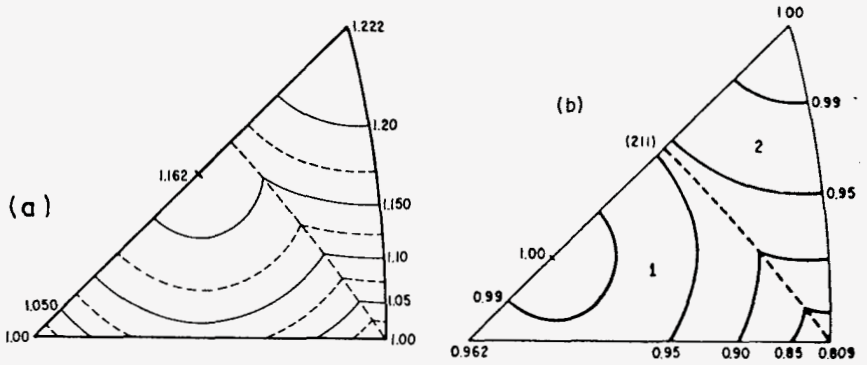

Figure 1.9 - Surface energy (γ_{SV}) for BCC iron (a) experimental (b) theoretical [38]

Grain Growth

The final stage of sintering is marked by a competition between shrinking pores and growing grains. The simplest grain growth models [39] describe the average grain size as a function of time as in equation [1.8]. The initial grain size, G_o, grows at a rate determined by k, which describes the interaction between grain boundary mobility and pore drag.

$$G_t^3 = G_o^3 + kt \qquad [1.8]$$

Uniform grain growth is uncommon, since a non-uniform distribution of driving forces and restraining forces are present locally at each boundary such as specific grain boundary energy, different inclusion sizes and populations, and a random distribution of pores. The restraining forces for grain growth are associated with the surface oxide on powder particles, and the pinning due to porosity. Zener [39] has developed an expression for the grain boundary pining force due to the particles. The Zener equation has been modified by German as shown in equation [1.9] specifically for the case of porosity pinning grain growth during sintering, where G is the grain size, d_p is the pore diameter, V_p is the pore volume, R is a pore attachment ratio and g is a geometric constant.

$$G = \frac{gd_p}{RV_p} \qquad [1.9]$$

A high volume fraction of fine pores are an effective grain boundary pinning force. As the compact is densified, the fine pores are eliminated and the volume fraction of pores decreases, which reduces the restraining force on grain boundaries and promotes grain growth. This occurs in the final stages

of sintering, and the grain growth is dependent on surface energy, grain boundary energy and diffusion rates.

During the final stages of sintering grain growth occurs to reduce the grain boundary area, and to develop the lowest energy grain boundary configuration. Equation [1.10] defines a Γ parameter [40] to predict the runaway grain growth, which is a function of the surface energy (γ_{SV}), grain boundary energy (γ_{GB}), surface diffusion (D_S) and grain boundary diffusion (D_{GB}).

$$\Gamma = \frac{D_S \gamma_{GB}}{300 D_{GB} \gamma_{SV}} \qquad [1.10]$$

The effect of the Γ parameter on the ratio of growing grains and initial grains with respect to the theoretical density is shown in Figure 1.10. As discussed earlier, the grains boundaries in a polycrystalline material have different energy depending on the crystallographic orientation with respect to the neighboring grains.

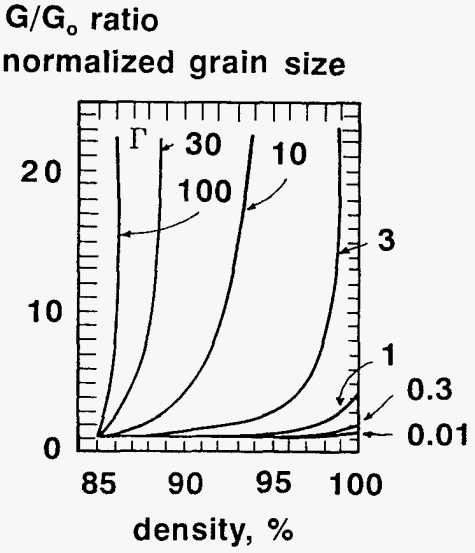

Figure 1.10 - Γ ratio for G_t/G_0 as a function of theoretical density [40]

The grain boundary energy is a function of the misorientation angle between adjacent grains. In a pure metal, the grain boundary energy increases until a tilt angle of approximately 15° [41], which is described as a high angle boundary. However, a semi-coherency between adjacent grains with specific crystallographic relationships can also reduce the grain boundary energy. Figure 1.11

shows specific high angle boundaries with a coincident site lattice (CSL) matching across the boundary have been shown to have a low energy configuration [41]. The difference between the γ_{GB} of a typical high angle grain boundary and a low energy CSL boundary is the driving force for grain growth. Any alloy additions which increase the elastic anisotropy or surface energy anisotropy would be expected to promote grain growth. In addition, the large grains observed in a sintered powder would be expected to have coincident boundaries with many adjacent grains.

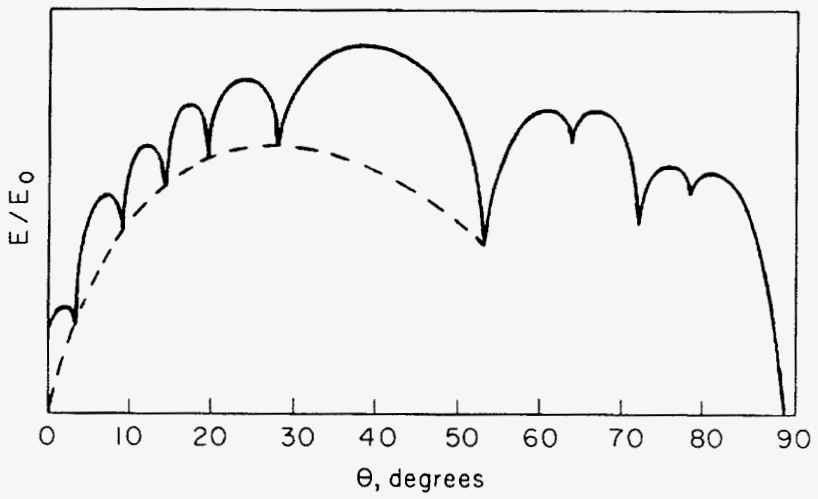

Figure 1.11 - Low energy grain boundary configurations for CLS boundaries [41]

Ductile-Brittle Fracture Transition

Since we have examined the potential intrinsic deformation mechanisms and the extrinsic microstructures which may develop from powder processing, we must now review how the intrinsic material properties and the microstructure combine to produce the mechanical properties useful to engineering function. The deformation and fracture are critical in the application of these materials. Therefore, we will discuss the aspects of brittle fracture mostly relevant to iron aluminum alloys, and related microstructural effects to the ductile to brittle transition behavior, which is a strong indication of the dislocation mobility in a material. Finally, will discuss the techniques which will be useful to measure the mechanical properties of small samples which we might use on actual MIM parts.

Brittle fracture usually has a temperature dependence due to the change of flow strength with temperature [42]. Figure 1.12 shows the yield strength and fracture strength as a function of temperature for a material that undergoes a ductile to brittle transition. Since the yield strength decreases with increasing temperature and the fracture strength only slightly decreases, at some

elevated temperature, T_{DBTT}, the material will yield prior to failure. As the difference between the yield strength and fracture strength increases, typically the amount of plastic strain prior to failure will increase. Of course, these observations apply generally to iron based alloys. The actual DBTT is dependent on intrinsic factors such as, microstructural uniformity, contamination level of grain boundary embrittling species, grain size and extrinsic factors such as, environment, test strain rate and materials stress state.

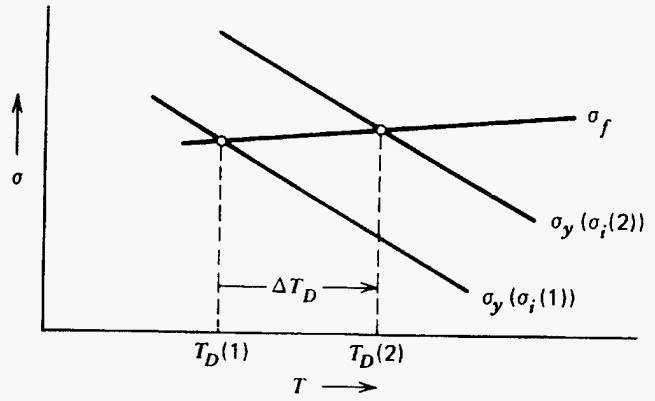

Figure 1.12 - Fracture strength and yield strength as a function of temperature [49]

The two common mechanisms of brittle failure are intergranular failure and transgranular cleavage. The intergranular failure is usually associated with the migration of impurity atoms such as sulfur and phosphorus to the grain boundary, which causes embrittlement. However, intermetallic compounds such as NiAl may exhibit intergranular failure due to meet Von Mises criteria of five independent slip system to maintain grain boundary compatibility [43]. The inability of dislocations to transmit slip through to adjacent grains has also been observed as a contribution to intergranular fracture. The ductilization of Ni_3Al has been accomplished by the small addition of boron to assist in slip transmission through the grain boundary, and increase the grain boundary cohesion energy [44,45].

Transgranular cleavage is observed in materials which have a intrinsically low cohesive energy in a preferred crystallographic orientation. The common cleavage planes in iron are the {100} type [43]. The cleavage crack is typically initiated at some defect such as an inclusion, pore or grain boundary triple point. The propagation of cleavage cracks are due to the lack of mobility of dislocations to migrate to the crack tip under tensile deformation to absorb the elastic energy of the crack. As stated previously, the dislocation mobility can be impeded by a number of intrinsic or

extrinsic factors. Ashby and Ghandi [46] a have categorized cleavage into 3 distinct fracture modes. Mode I - the propagating crack was nucleated is from a feature smaller than the grain size. Mode I cleavage is observed in ionic solids with no evidence of plastic deformation. Mode II - the propagating crack was nucleated by a feature on the order of the grain size such as a twin boundary. Mode II cleavage fractures typically show a minor amount (<3%) of plasticity before failure. Mode III- the propagating crack was nucleated from a feature that was larger than the grain size. The cleavage phenomena in Mode III exhibit extensive plasticity (>10%), but the fracture appearance contains the characteristic cleavage planes. Iron alloys have been observed to contain all three mode of cleavage, which is dependent on the substitutional alloy content, interstitial content, carbide size and volume fraction, the test temperature and strain rate. It is worthwhile to note that the introduction of second phases into the matrix of a BCC metal has two effects. The first beneficial effect is to impede dislocation motion, thereby increasing the flow stress. A second detrimental effect is to limit slip to promote embrittlement. The limit of slip is overcome by thermal activation and the strain rate of the test, which directly relates to dislocation velocity. However, the introduction of coherent intermetallic phases may have an advantage since dislocations may pass through them, if the dislocations have sufficient shear stress.

Many phenomena have been proposed for the limited ductility observed in Fe-Al such as: grain boundary embrittlement by impurities, short range order, long range order, low cleavage strength, insufficient slip systems for grain boundary compatibility, poor grain boundary cohesion and most recently hydrogen embrittlement [8, 47,48]. The tensile ductility of binary Fe-Al alloys in air were characterized by Taylor, Marcinkowski and Kayser [48] shown in Figure 1.13.

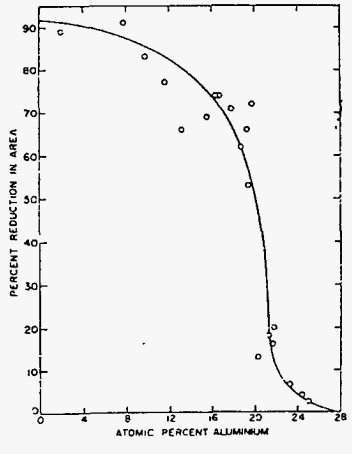

Figure 1.13 - Tensile ductility of alloys slowly cooled to 477 K and tested [44]

Recently, the researchers at Oak Ridge National Laboratories [7] have found additions of 2 at.% chromium to be beneficial to room temperature ductility, to produce a material with comparable yield strength to austenitic stainless steel. Liu [48] has shown the brittle behavior of iron and nickel aluminides to be a hydrogen assisted embrittlement, which forms due a reaction water vapor in the ambient environment with Al in the alloy at a crack tip. The chromium addition somewhat alleviates this condition by a passivation protection, but does not completely eliminate hydrogen embrittlement.

Fracture Energy

According to the Griffith-Orowan criteria two factors influence the toughening: the surface energy created by cleavage (γ_s), and the plastic deformation energy (γ_p) related to the ability of the material to absorb energy by dislocation motion. In ductile materials such as copper, the ratio γ_p/γ_s = 6-10 [42]. A material with moderate ductility will have a lower γ_p/γ_S . If the plastic deformation energy is low, then the fracture will be dominated by cleavage. If the plastic deformation energy is high, then the fracture will tend to occur by microvoid coalescence.

$$\sigma_f = \left(\frac{2(\gamma_S + \gamma_P)E}{\pi c} \right)^{1/2} \qquad [1.11]$$

The fracture strength of a material exhibiting cleavage failure improves with decreasing grain size. A grain boundary interrupts the easy propagation of a cleavage crack on the preferred cleavage planes. When the crack approaches a grain boundary, an increased stress is required to move the crack through the grain boundary into the adjacent grain. The number of dislocation sources also increases in the close proximity of grain boundary. A smaller grain size increases the frequency of the crack arresting interactions with grain boundaries. Cotrell and Petch [49] have shown the fracture strength of a cleavage dominated material to be inversely proportional to the square root of the grain size. Therefore, the toughness Fe-Al-Si alloys will depend on the mobility of dislocations to blunt the microcrack and prevent crack propagation. The grain boundary orientation relationship may effect the energy required to propagate through the boundary into an adjacent grain.

Mechanical Properties of Materials with Porosity

The fracture strength of a brittle material isotropic mechnical properties containing porosity is typically predicted by the equation [1.12]. Where the fracture strength, σ_f, is a maximum in a pore free material, σ_o, with the fraction porosity, p, equal to zero. The pore sensitivity constant, m, must be determined for each material [50]. This empirical relationship apply well to large porosity values > 0.10, but as pores become isolated the relationships are more complex. The strength depends on pore geometry, size, distribution and proximity to grain boundary. A model which examines the effects of grain size and isolated porosity on the fracture strength of brittle materials used Griffith's equation and is shown in equation [1.13]. The equation describes a pore on a grain boundary acting as crack nucleation site. The crack is assumed to easily propagate along the grain boundary until it intersected another grain boundary. The diameter of the average grain is G, the radius of a pore is R, the surface energy is γ, and the modulus of elasticity is E. The fracture strength will increase as the grain size and pore size are reduced in a brittle solid.

$$\sigma_f = \sigma_o (1-p)^m \qquad [1.12]$$

$$\sigma_f = \left[\frac{2\gamma E}{\pi(R+G)}\right]^{1/2}. \qquad [1.13]$$

The prediction of the effect of isolated pores on the fracture toughness and fracture strength of ductile materials is complex. The model for void coalescence for ductile failure has been reviewed by Ritchie and Thompson [51]. The models predict a microscopic strain density developed in the triaxial stress state between pores of a spacing. The plastic zones between pores overlap, and work hardens the material to the fracture strength. The work absorbed by the material has been related to the dimple surface microroughness, M, defined as h/W, where the width of the dimple, W, and the depth of the dimple, h. The critical local fracture strain, ε_f^*, has been defined in terms of M and the fraction of porosity, f_p, by equation [1.14]. The M factor has also been related to the fracture toughness by equation [1.15], where σ_o is the yield strength and l_o is a distance between initial pores.

$$\varepsilon_f^* \cong \frac{1}{3}\ln\left(\frac{M^2}{3f_p}\right) \qquad [1.14]$$

$$J_{IC} \approx \frac{\sigma_o}{3}\ln\left(\frac{M^2}{3f_p}\right) l_o \qquad [1.15]$$

Mechanical Property Testing

As discussed earlier, the mechanical property evaluation of powder processed iron aluminide alloys has been conducted predominantly by previous investigators on hot extruded bar [1,2,5]. Tensile testing was conducted along the extruded direction, which was affected by the texture developed during processing. Prichard, Kameda and Anderson [52] at Ames Laboratory have published the only known mechanical properties of sintered iron aluminum alloys. This testing was conducted by a small punch technique, which uses a small disk with dimensions of 6 mm in diameter and 0.5 mm thick. Small punch testing was selected as a mechanical test technique for a number of reasons. The sample preparation and test apparatus is relatively simple, which may allow it to be used as a good technique for the evaluation of small MIM parts. The punch test has been used successfully to perform life prediction evaluations of alloy steel containment walls in nuclear reactor vessels, because of the sensitivity to subtle changes in microstructure [53]. Mao and Takahashi [54] have developed an empirical correlation equation [1.16] for determining the yield strength from the load-displacement curve, where P_y is the load on yielding and t_o is the initial sample thickness.

$$\sigma_y\ [\text{MPa}] = 360(P_y / t_o)^2\ [\text{kN/mm}^2] \qquad [1.16]$$

Empirical correlation equations have also been developed for K_{IC}, J_{IC} and charpy impact testing. The use of small punch testing for the determination of the ductile-brittle transition temperature (DBTT) in steels of reactor vessel has been a reliable technique [55]. The fracture energy is determined from the integrated area under a load-displacement curve up to the maximum load. Foulds and coworkers [56] at the Electric Power Research Institute (EPRI) have used finite element models to examine the strain energy density in punch tests and correlate the behavior to uniaxial tensile tests and fracture energy values. Typically, the fracture surface of each punch sample is examined with a scanning electron microscope to determine the fracture mechanism.

CHAPTER 2. EXPERIMENTAL PROCEDURE

Alloy Exploration

Twelve different Fe-Al alloys compositions were produced by DC-arc melt casting of high purity elemental constituents of electrolytic iron, aluminum, silicon, titanium and molybdenum. The alloys shown in Table 2.1 were grouped in three categories: binary Fe-Al alloys, ternary Fe-Al-(Si,Ti) alloys and quaternary Fe-Al-Si-(Ti, Mo) alloys. Since the mechanical properties and phase equilibrium of the binary alloys have been extensively evaluated by previous investigators, they were used as a baseline reference for hardness and heat treatment response. Each 50 gram chill cast button was turned over and remelted to insure a homogenous composition throughout the button. The buttons were cut and polished for microhardness testing, metallographic analysis, and the button were crushed for chemical analysis. The major elemental compositions and the low levels of phosphorus and sulfur were determined by inductively coupled plasma- atomic emission spectroscopy. The oxygen and nitrogen levels were measured by inert gas fusion. Carbon content was determined by a combustion infrared absorption technique.

Table 2.1 - Nominal Compositions (at.%) for Vacuum Arc Melt Buttons of Iron Aluminum Alloys

Heat No.	Fe	Al	Si	Ti	Mo
PP001	Bal.	15	-	-	-
PP002	Bal.	20	-	-	-
PP003	Bal.	24	-	-	-
PP004	Bal.	28	-	-	-
PP005	Bal.	15	2	-	-
PP006	Bal.	15	5	-	-
PP007	Bal.	15	-	2	-
PP008	Bal.	15	-	5	-
PP009	Bal.	15	2	1	-
PP010	Bal.	15	5	1	-
PP011	Bal.	15	5	2	-
PP012	Bal.	15	5	-	1

The metallographic samples were mounted in Bakelite™ and polished with SiC using standard metallographic procedures. The samples were etched with a solution of 1 part HNO_3: 1part HCl and 1 part distilled H_2O. The microstructures were examined with an optical metallograph to reveal any obvious microsegregation in the chill cast button. Samples were solution heat treated at 1000°C for 24 hours in an air muffle furnace and quenched into water to allow the homogenization of the alloying elements. An ordering heat treatment was conducted at 500°C for 24 hours in an air muffle furnace with and air cooling to promote the stability of the ordered phases such as Fe_3Al. At least 100 microns was removed from the heat treated samples surfaces by 80 grit SiC abrasive paper to remove the oxide scale and the underlying base metal. The ground surfaces were polished through 600 grit SiC paper prior to microhardness testing. The diamond pyramid microhardness was determined using a load of 500 grams. An average DPH value and standard deviation was determined for each sample using 5 indentations spaced approximately 1 mm apart.

Atomization Processing

The melt for powder atomization was prepared by direct alloying in the atomization melt crucible for the majority of Fe-Al-Si. High purity grade electrolytic iron (99.99%), commercial aluminum pellet (99.9%), and electronic grade silicon (99.99%) was used to formulate the alloys. The granular elemental constituents were mixed randomly and directly introduced into the Norton Alundum™ melt crucible. The charge mixture was melted and superheated to 1725°C for 5 minutes prior to pouring. The powder was produced by high pressure gas atomization (HPGA) [Anderson] at Ames Laboratory. The melt was fed into the gas atomizing nozzle at 1.5 to 2.0 kg/min, while the argon gas flow rate was approximately 8.49 m^3/min at a gas supply pressure of 7.4 MPa.

The resulting atomized powders were sieved through a 106 μm screen to remove the very coarse irregular material, and sieved through a 45 μm sieve to remove a coarse fraction of regular powder. A pneumatic classifier was used to produce a fine fraction of powder with $D_{84} < 32$ μm, which was suitable for sintering experiments simulating binder free MIM processing. The Acucut air classifer was used with a rotor speed of 480 rpm, a blower pressure of 3.4 KPa, and an ejector gas pressure of 345 KPa. The coarse powder fraction from this pneumatic classification was used for the P/M hot extrusion product.

Powder Characterization

The fraction of fine powders produced by pneumatic classification were analyzed by an automated laser light scattering technique. A gram sample of powder was dispersed in 50 ml of a isopropyl alcohol solution with 1.0 gram of hexadecatrimethyl ammonium bromide. The sample was

run three times and the data was combined to improve the accuracy. The aluminum and silicon contents in the powders were determined by inductively coupled plasma (ICP-AES) technique, while the oxygen, nitrogen, carbon and sulfur were determined as described earlier. Differential thermal analysis was performed with a Perkin Elmer instrument at heating at a rate of 10°C/min in argon to determine the melting and solidification behavior of each alloy. Helium pycnometry determined the density of each of the powder alloy sample, after sieving to a size distribution of less than 45 μm. The density was determined to within 0.005 g/cm^3. The apparent density and tap density were determined by filling a 50 ml graduated cylinder with approximately 50 grams of powder. The tap apparatus firmly fixed the graduated cylinder in place and used an eccentric cam to lift the cylinder approximately 1 cm at 200 cycles per minute. The mass of the powder was measured with a high precision balance to ± 0.001 gram. The volume was measured to ±0.05 ml after the initial fill to determine the apparent volume, and the powder volume was measured again after running for 20 minutes on the tap apparatus.

Scanning electron microscopy (SEM) was used to examine the grain sizes and cell sizes in powders ranging from 1 μm to 100 μm in diameter for each alloy. The powder particles were mounted in epoxy, and were polished and etched to reveal microstructure using the etchant described above. Measurements were made on at least three powder particles at each size by the line intercept method to determine the grain size. The cell size was determined by the line intercept method from the examination of SEM images of the powder exterior surface. The powder surfaces were examined by Auger electron spectroscopy. The atomized surfaces were examined for carbon, oxygen, nitrogen, sulfur, phosphorus, aluminum, silicon. The powders were sputter cleaned with argon for 3 minutes to remove approximately 100 nm of the exterior surface. The change in composition was monitored every 15 seconds to measure the composition as a function of the depth below the initial powder surface.

Vacuum Sintering

Two approaches were used to evaluate the sintering response of Fe-15Al, Fe-15Al-2.8Si, Fe-15Al-5Si (at.%) atomized powders. The first was for a quantitative measurement of bulk sintered density. The second was a qualitative comparison of the sintered surface microstructure as a function of temperature. The bulk density samples were produced by filling a high density alumina crucible 20 mm in diameter and 25 mm tall with powder, and tap consolidating with 100 firm taps on a hard surface. The tap density was approximately 65% of the theoretical density for each powder prior to sintering, which was comparable to the typical volume loading of powder present in MIM feedstock.

The tap dense powders were heated at a rate of 60°C/min at a vacuum of (10^{-6} torr) and held at 1200°C, 1250°C, 1300°C for 2 hours. The effect of time on densification was investigated on each of the compositions at 1200°C for times of 0.2, 0.5, 1.0, 2, 5, 10 and 20 hours. The sintered samples were machined to 15 mm diameter and 15 mm long. Density was determined by measuring specimens machined from the sintered cylinders to an accuracy of ± 0.01 mm and weighing the samples to the ± 0.001 grams. The sintered samples were mounted in epoxy using vacuum infiltration, and polished by standard metallographic techniques, and grain sizes were determined by the line intercept method on representative areas.

Image analysis was performed using Image Pro software to measure the areal fraction of porosity in the samples sintered from 1100°C to 1200°C. The samples were examined in the unetched condition. The black and white spectra contain 255 shades of gray, which correspond to specific microstructural features. The software allows the user to select a spectrum range and highlights the image features at those levels of gray. The spectra for porosity was determined was by selecting the range of channels that highlighted the porosity. The software counts the pixels for the selected range and the areal fraction was calculated by dividing the porosity pixels by the total image pixels. The technique worked reasonably well for high levels of porosity, but not at lower levels of porosity. Microstructural features with similar gray levels as porosity such as inclusions and polishing artifacts introduced noise into the measurement. Therefore, the automated image analysis was not used for the samples sintered at temperatures above 1200°C where samples contained less than 10% porosity. Instead, the quantitative porosity level of powders sintered above 1200°C was determined by the bulk density measurements described above.

The observation of the sintered surface topology has been shown an effective method to discern differences between powder sintering characteristics. Vacuum sintered samples were produced by the same tap consolidation technique described previously. However, the crucible were filled with only 5 grams of powder to produce a sintered disk no greater than 0.5 cm thick. The sintering temperature range was increased from 1100°C to 1300°C in 50°C increments to observe the evolution of densification. A scanning electron microscope was used to observe the surface of these sintered samples to show the surface topology of the three alloys at each sintering condition.

Hot Powder Extrusion

Extrusion experiments were conducted by using the coarse powder fraction described above from each HPGA powder batch. Approximately 900g of powder was placed in a stainless steel can, 5 cm diameter and 7.5 cm length, with a 1.5mm wall thickness, shown in Figure 2.1. The powders

were tapped to pre-consolidate, evacuated to 10^{-7} torr, and sealed with an electron beam weld. A mild steel outer can with a wall thickness of 0.5 cm and a 45 degree tapered nose cone was welded to encase the stainless steel can to prevent die chill. The extrusion die diameter had an entry of 7.5 cm with an exit of 2.0 cm to give an extrusion ratio of 14:1. The powder can assembly was preheated for 3 to 4 hours at 1000°C in an air muffle furnace prior to extrusion through a tool steel die preheated to 300°C. The preheated can was processed by the force of a 40 ton hydraulic extrusion press in less than 15 seconds after removal from the muffle furnace to minimize heat loss. After extrusion, the hot bars were allowed to naturally cool to room temperature in still ambient air. Metallographic samples were prepared from the extrusions as described previously in the transverse and longitudinal orientations. A vibratory polisher with colloidal silica was used for final polishing. The samples were chemically etched with a solution of 1 part HNO_3: 1 part HCl: 1 part H_2O. The grain sizes were measured by the line intercept method in accordance with ASTM E112.

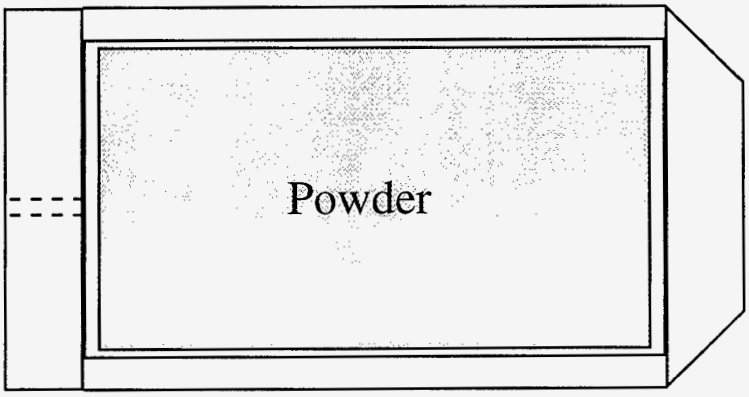

Figure 2.1 - Schematic of powder extrusion can assembly

Mechanical Property Characterization

The punch test apparatus is shown in Figure 2.2. Small punch testing was conducted on samples extracted from the sintered bars and extruded rod. The test samples were prepared by lathe machining a 6 mm diameter cylinder from each extrusion or sintered sample. A number of disks with a 0.6 mm thickness were cut from each cylinder by a high speed wet abrasive saw. Heat treatments were performed on disks from each extrusion by placing them in evacuated quartz vials and heating them to 600°C for 7 days and water quenching on removal. Approximately 50 μm of thickness was removed from each side of the heat treated samples by using wet SiC paper with the final polishing using 1200 grit SiC. The average thickness varied from 450 μm to 530 μm. The punch test

temperature was controlled using an induction coil surrounding the test fixture to regulate the temperature within ±5°C. The test disk was clamped into the test fixture to eliminate lateral movement during testing. The 2.4 mm radius SiC hemispherical punch was compressed onto the test disk at a rate of 10^{-3} mm/sec. The punch disk stress state is complex and changes during the test.

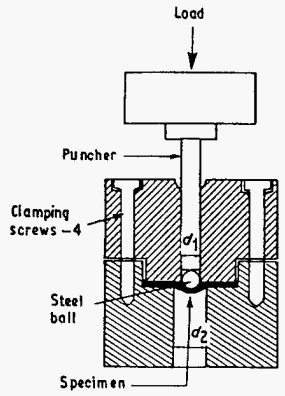

Figure 2.2 - Small punch test apparatus

The disk surface on the opposite side of the punch/disk interface experienced a multiaxial tensile stress as the punch moved into the disk. Microscopically the disk had a distribution of tensile stress levels from a minimum at the punch/disk interface to the maximum stress on the opposite disk surface. The macroscopic load was recorded by a load cell as a function of the crosshead displacement as shown in Figure 2.3. A typical load-displacement curve has four characteristic regimes: regime I - elastic bending, regime II - plastic bending, regime III - plastic stretching and regime IV plastic instability [53].

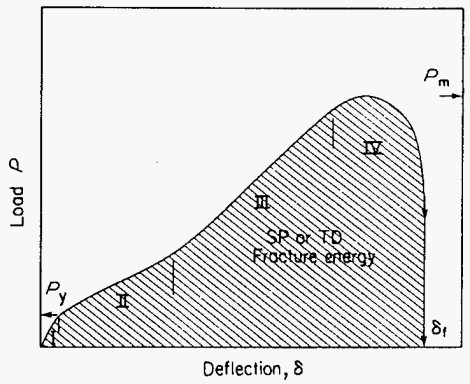

Figure 2.3 - Load-Displacement curve for small punch test

Mao and Takahashi [40] have developed an empirical correlation equation [2.1] for determining the yield strength from the load-displacement curve, where P_y is the load on yielding and t_o is the initial sample thickness. The fracture energy is determined from the integrated area under a

$$\sigma_y \text{ [MPa]} = 360(P_y / t_o)^2 \text{ [kN/mm}^2\text{]} \qquad [2.1]$$

load-displacement curve up to the maximum load to determine the millijoules of energy absorbed by the sample prior to failure. The fracture energy was plotted as a function of temperature to determine the ductile to brittle transition temperature for the Fe-15Al-xSi alloys. The fracture surface of each punch sample was examined with a scanning electron microscope to determine the fracture mechanism. Samples were tested from the extruded alloys of Fe-15Al, Fe-15Al-2.8Si and Fe-15Al-5Si from 25°C to 550°C. The disks were tested from the as-extruded alloys, extruded alloys with a 600°C/wk heat treatment and the Fe-15Al-2.8Si alloy sintered at 1200°C and 1300°C with a 600°C heat treatment for 24 hours.

Limited tensile testing was conducted on the extruded alloy bars for comparison with the punch sample. The bars were tested in the as-extruded condition or with a 600°C/24 hr/WQ heat treatment. The bars were heat treated in an air muffle furnace for 24 hours and quenched into a bath of water prior to machining. The tensile tests employed a threadless tensile bar configuration shown in Figure 2.4, which was designed for brittle materials to be compatible with a MTS hydraulic collet grip. The tensile bars were tested at room temperature and 550°C. The bars were heated by a high frequency induction power supply and held constant for 5 minutes to allow the system to thermally equilibrate before testing. The crosshead speed was 2.12×10^{-3} mm/sec up to the yield point to discern the transition from elastic to plastic flow, and then continued at 21.2×10^{-3} mm/sec until the failure of the bar. The strain was measured by an extensometer, and the load was measured by a load cell. The data were recorded by a data acquisition system. The tensile data and the punch data for each alloy and condition were compared to evaluate the accuracy of the generalized correlation equation. However, to conduct the punch test in the same extrusion orientation as the tensile bars the punch test samples were taken in the longitudinal orientation from the grip sections of the tensile bars. The samples were prepared and tested with the same procedure as described earlier. The data analysis was also conducted using the same techniques.

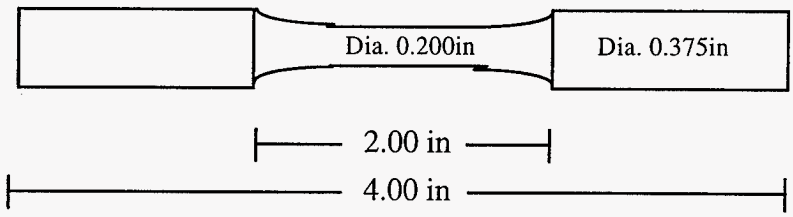

Figure 2.4 - Threadless tensile bars for extruded material

Texture Measurement

Since the extrusion process has been observed to produce texture, the texture measurement of the extrusion was conducted on each powder alloy of this investigation. The texture orientation is an important consideration in comparison of tensile properties in extruded material. The properties for iron alloys, and iron aluminide can be enhanced with a preferred orientation. However, the properties are anisotropic and do not represent the isotropic properties such as those in a metal injection molded and sintered part. The crystallographic texture was measured by x-ray diffraction on a transverse section from each extruded alloy. The samples were cut approximately 5 mm thick and ground parallel with a special platten. The examined surface was polished through 600 grit papers and etched with a 80% methanol + 20% volume nitric acid solution. A Phillips 1760 x-ray generator unit was powered at 40 kV and 30 mA. A Cu-Kα radiation source was used and directed through a collimator. The two theta peak for the (110) planes was determined by scanning through 43 to 46 degrees. The highest intensity two theta was used to generate a texture map of the transverse orientation.

Figure 2.5 shows a goniometer with the phi angle ranging from 0 to 80 degrees, with a slow scan rate of 240 rpm, 6 degree increment rotations with a spiral of 2.5 degrees per rotation using a 4 second exposure at each increment. Examination of the texture perpendicular to the extrusion axis was conducted using the same sample preparation and the (110) two theta peak. These values were compared with the extrusion axis to indicate any preferred secondary texture. The intensity for each angular orientation was measured using a scintillator detector with a wide slit. The ratio of the intensity to the background was determine and contours were plotted at various intensity ratios. A value of 1.0 represented complete randomness. Values greater than 1.0 indicate a texture with a specific angular relationship to the extrusion axis. The strength of the texture is determined by the maximum values and the angular breadth surrounding those peak values. The data is commonly represented in a strereographic projection or pole figure, or a modified inverse pole figure.

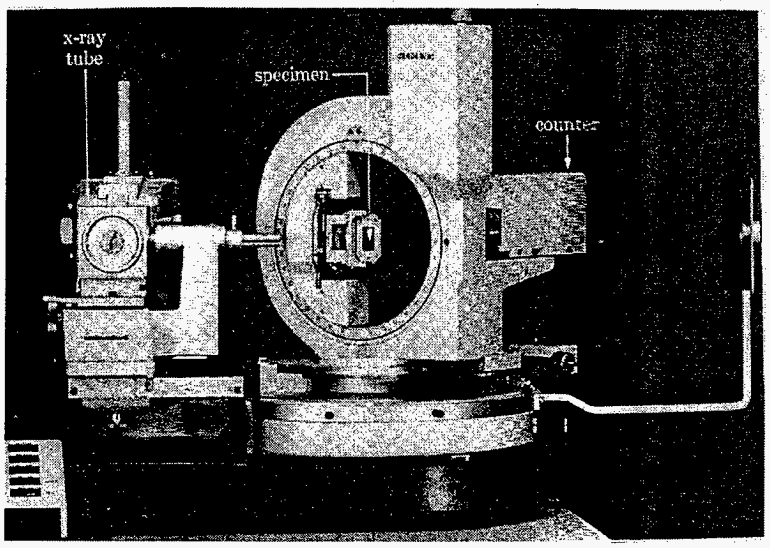

Figure 2.5 - Pole figure goniometer for X-ray texture measurement [15]

Hot Stage TEM

Wafer slices 300 microns thick were cut from the extrusions by a high speed abrasive saw. The wafers were mounted with crystal bond and polished with SiC paper to 100 microns or less thickness. TEM disks were extracted by a 3mm punch. The disks were further thinned by a twin jet electropolish unit with a solution of 70% methanol and 30% nitric acid. The acid bath was kept at a temperature of -40°C with a current of 25 milli-amperes and a DC voltage of 50 V. A hole took approximately 2 to 3 minutes to form.

Each 3 mm disk was mounted in a double tilt sample holder with a hot stage of resistively heated platinum. A chromel-alumel thermocouple was used to control the temperature of the sample to within ± 5°C. The Phillips 100CV microscope used a LaB_6 filament operated at 300kV. The sample was examined at room temperature to find appropriate thin areas and then tilted to a major zone axis. The zone axis of (001), (110) and (111) were examined and micrographs were taken of the SAD patterns. Images were taken in the bright field condition, dark field condition and a two beam condition to highlight the ordered regions. The dark field was taken in the (001) and (110) orientations using the fundamental reflections and superlattice reflections. The superlattice reflections of the Fe_3Al phase were not observed in the (111) zone axis due to the overlap with fundamental reflections. Images were produced with a two-beam condition using a primary and superlattice reflection. The magnification of the images ranged from 10,000x to 200,000x to resolve the small ordered regions.

The sample was heated to 200°C, 400°C and 600°C and 800°C for 1 hour while at a (110) zone axis to observe the superlattice reflection intensity. SAD patterns, bright field images and dark field images were taken at the elevated temperatures similar to the room temperature procedure described previously. Indications of the transformation were given by the superlattice reflections in the SAD patterns. Figure 2.5 shows the pattern for a (110) zone axis of the fundamental peaks and the expected superlattice reflections. There exist 3 possible configurations of BCC derivative lattices with the Fe-Al system: the B2-CsCl, the DO_3-Fe_3Al and the B32-NaTl system. The superlattice reflections appear at half the distance between the fundamental reflections. In the (110) zone axis the presence of only the (200) superlattice spots indicate the B2 structure, whereas the presence of on the (111) superlattice reflections indicate the B32 structure and the presence of both the (200) and the (111) indicate the presence of the DO_3 structure.

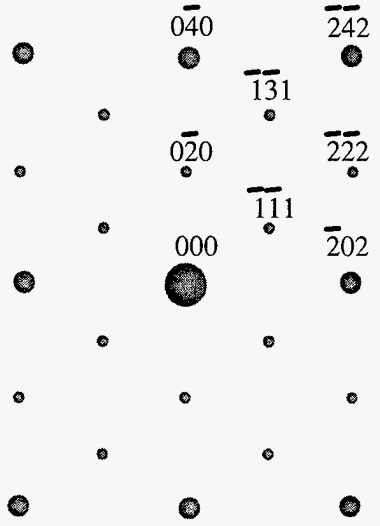

Figure 2.6 - Superlattice Reflections in (101) zone axis [54]

CHAPTER 3. RESULTS

Arc Melted Buttons

The initial results from arc-melted buttons and cold hearth cast were used to assess the most viable alloy additions to study on a baseline composition of Fe-15Al atomic percent. The chemical analysis of arc melt and cast buttons are shown in Table 3.1. Although the major elemental chemistry is reported in atomic % to consider the composition related to compound stoichiometry (i.e., 3 to1), the normal reporting practice for impurity elements is reported as parts per million by weight (ppmw). The measured chemistry was close to the aim compositions with a slight reduction in aluminum content perhaps due to some volatilization during melting. The impurity and interstitial content were generally quite low with carbon = 40±20 ppm, nitrogen = 20±5 ppm, oxygen ranging from 36 ppm to 553 ppm, sulfur = 50±10 ppm and phosphorus = 40 ppm. The oxygen contents appeared to have no correlation with aluminum, silicon or titanium content. The variation in oxygen was probably due to either the introduction of slightly oxidized electrolytic iron or non-ideal casting environment.

Table 3.1 - Chemical Analysis of arc Cast Buttons (at%)

Heat	Al	Si	Ti	Mo	P	S	C	N	O
001	15.20	<0.01	0.002	<0.005	<40 ppm	50 ppm	54 ppm	24 ppm	290 ppm
002	18.84	<0.01	0.001	<0.005	90 ppm	90 ppm	58 ppm	23 ppm	339 ppm
003	23.12	<0.01	0.002	<0.005	<40 ppm	60 ppm	40 ppm	11 ppm	57 ppm
004	26.57	<0.01	0.002	<0.005	<40 ppm	50 ppm	25 ppm	20 ppm	128 ppm
005	15.24	1.81	0.001	<0.005	<40 ppm	60 ppm	67 ppm	17 ppm	75 ppm
006	15.36	4.50	0.001	<0.005	<40 ppm	60 ppm	47 ppm	23 ppm	553 ppm
007	15.14	<0.01	1.940	<0.005	<40 ppm	60 ppm	25 ppm	18 ppm	217 ppm
008	15.31	<0.01	4.820	<0.005	<40 ppm	50 ppm	26 ppm	21 ppm	328 ppm
009	15.25	1.79	1.010	<0.005	100 ppm	50 ppm	25 ppm	19 ppm	36 ppm
010	15.38	4.56	1.000	<0.005	<40 ppm	40 ppm	31 ppm	20 ppm	79 ppm
011	15.25	4.72	2.590	<0.005	<40 ppm	50 ppm	25 ppm	14 ppm	79 ppm
012	15.51	4.77	0.001	1.035	<40 ppm	60 ppm	39 ppm	22 ppm	308 ppm

The microhardness results in the as-cast, solution and ordered condition are shown in Table 3.2. Figure 3.1 shows the microhardness of the binary Fe-Al alloys, Figure 3.2 shows the microhardness of the ternary Fe-15Al-(Si,Ti) alloys, and Figure 3.3 shows the microhardness of the quaternary Fe-15Al-Si-(Ti,Mo) alloys. Each binary alloy showed a slight increase (10 to 30 DPH) in hardness with the solution heat treatment at 1000°C. The increase was believed to be due to the homogenization of the aluminum in the as-cast microstructure.

Table 3.2 - DPH Hardness of Vacuum Arc-cast Buttons

Alloy (at.%)	As-cast	Solution (1000°C/24 hrs)	Ordering (500°C/24 hrs)	Qualitative Toughness
Fe-15Al	192 ± 6.4	206 ± 6.3	237 ± 14.2	good
Fe-20Al	226 ± 8.6	252 ± 7.8	260 ± 10.0	fair
Fe-24Al	286 ± 8.7	304 ± 5.5	318 ± 0.6	fair
Fe-28Al	262 ± 9.3	292 ± 4.5	377 ± 7.8	good
Fe-15Al-2Si	270 ± 18.0	283 ± 7.0	341 ± 9.1	fair
Fe-15Al-5Si	390 ± 11.0	382 ± 13.0	428 ± 10.4	poor
Fe-15Al-2Ti	410 ± 15.1	254 ± 11.5	496 ± 14.2	poor
Fe-15Al-5Ti	525 ± 15.9	504 ± 16.3	683 ± 32.4	nil
Fe-15Al-2Si-1Ti	422 ± 9.4	337 ± 9.9	448 ± 30.5	poor
Fe-15Al-5Si-1Ti	399 ± 7.2	411 ± 16.3	469 ± 17.5	nil
Fe-15Al-5Si-2Ti	516 ± 18.5	402 ± 21.8	518 ± 28.7	nil
Fe-15Al-5Si-1Mo	385 ± 8.1	399 ± 11.8	421 ± 11.2	poor

The alloys containing titanium were observed to decrease in hardness with the 1000°C heat treatment possibly due to the dissolution of complex intermetallic compounds in the as-cast microstructure such as $Fe_3(Al,Ti.)$. The 500°C heat treatment produced the largest hardening effect in the alloys with titanium additions compared to the Fe-15Al baseline condition. The alloys containing titanium showed an increase of 260 DPH with 2 at.% and an increase of 446 DPH with a 5 at.% addition compared to the Fe-15Al baseline condition. The silicon additions produced a substantial hardening effect after the 500°C heat treatment with an increase of 104 DPH with 2 at.% and an increase of 191 DPH with the addition of 5at.% compared to the Fe-15Al baseline condition. Unfortunately, the alloys which had a microhardness greater than 400 DPH developed microcracks at the corners of the diamond indentations. Since the Fe-Al-Si alloys exhibited a suitable range of microhardness and toughness with heat treatment, they were selected as materials for further exploration by powder processing.

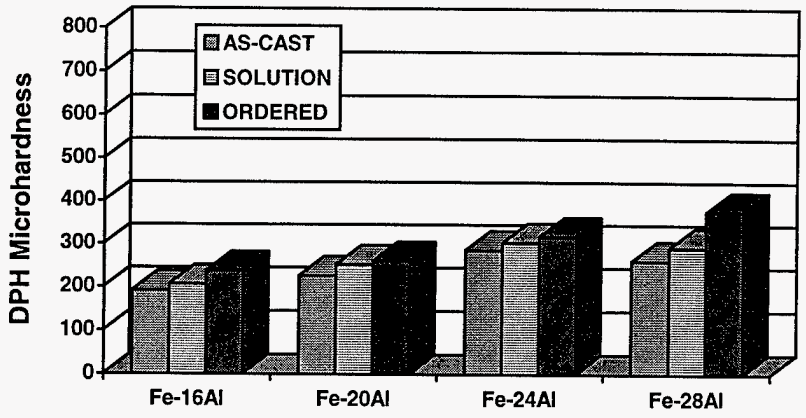

Figure 3.1 - Microhardness of Fe-Al arc melted buttons

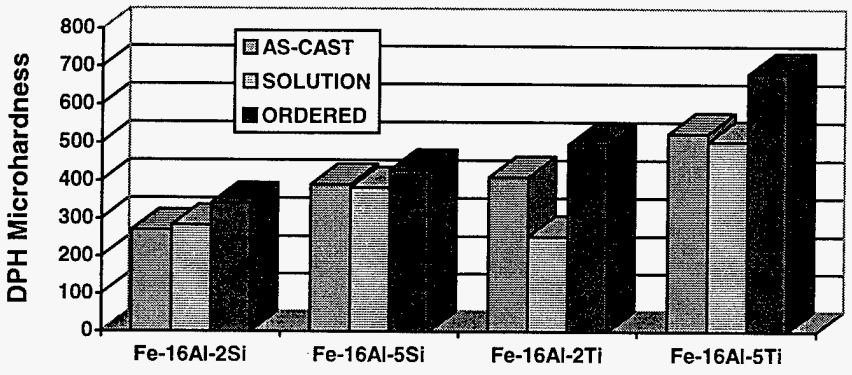

Figure 3.2 - Microhardness of Fe-Al-(Si,Ti) arc melted buttons

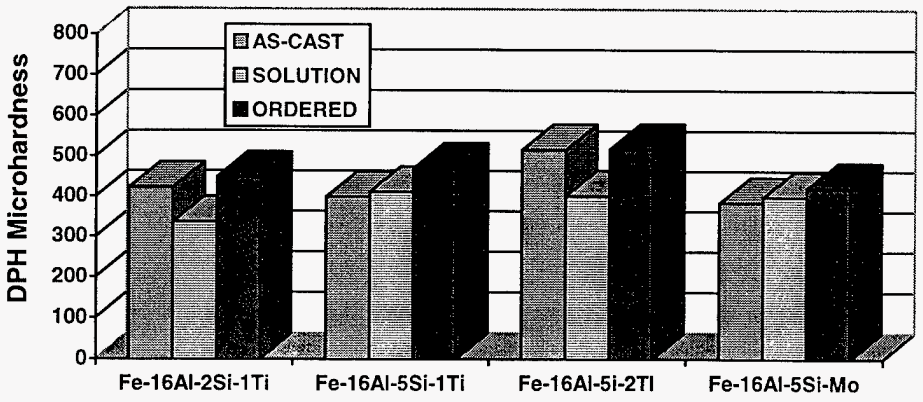

Figure 3.3 - Microhardness of Fe-16Al-Si-Ti arc melted buttons

Powder Processing

The chemistry results shown in Table 3.3 reveal a slight reduction from the aim aluminum and silicon contents in fine powders. The aluminum and silicon values are consistent within the 1% error of the ICP-AES technique. The impurity contents of carbon, nitrogen, sulfur and phosphorus were exceptionally low by commercial standards due to the high quality grade of electrolytic iron used. The oxygen chemistry ranged from 232 ppm to 343 ppm, which was excellent for fine powders containing 15 at.% aluminum. Oxygen levels have been shown to be associated with the powder surface for aluminum containing alloys. Therefore, the observed levels of oxygen are very reasonable for finely divided powder less than 45 microns.

Table 3.3 - Chemistry of HPGA Powders (ICP)

Nominal Composition	Al (wt%)	Si (wt%)	O (ppm)	N (ppm)	C (ppm)	S (ppm)	P (ppm)
Fe-15Al	15.03	0.02	343	11	66	10	40
Fe-15Al-2.8Si	15.12	2.87	339	6	56	9	50
Fe-15Al-5Si	14.73	5.06	232	3	64	20	30

The specific nature of the surface oxygen in these Fe-Al-Si powders was examined by Auger electron spectroscopy (AES). Figure 3.4 shows the AES data for a powder surface of Fe-15Al-5Si which revealed an enrichment in oxygen and carbon. The oxygen concentration at the surface of the powder was approximately 50 at.% and the carbon concentration was approximately 25 at.%. The analysis during argon sputtering indicated a sharp reduction in oxygen concentration at 100 Å and the oxygen was reduced to the matrix level after approximately 250 Å of powder surface was removed. The initial surface layer appeared to be slightly enriched with silicon. The ratio of iron to silicon was 5:1 at the surface, but the Fe:Si ratio was reduced to 6:1 after 250 Å. Whereas, the iron to aluminum ratio was 5:1 at the surface, but the Fe:Al ratio increased to 3:1 after 250 Å of argon sputtering. The transition between silicon enrichment and aluminum The depth of the oxygen enrichment was similar for the Fe-15Al-2.8Si alloy. Of course the Fe-15Al had no silicon present. but the Fe:Al ratio's were similar to the ternary alloys. The presence of this oxide film on the surface is suspected to be the source of the oxygen for the prior particle boundaries, which are observed during sintering. At higher temperatures, the aluminum and silicon will preferentially react with the oxygen due to the thermodynamic stability of their oxides relative to iron.

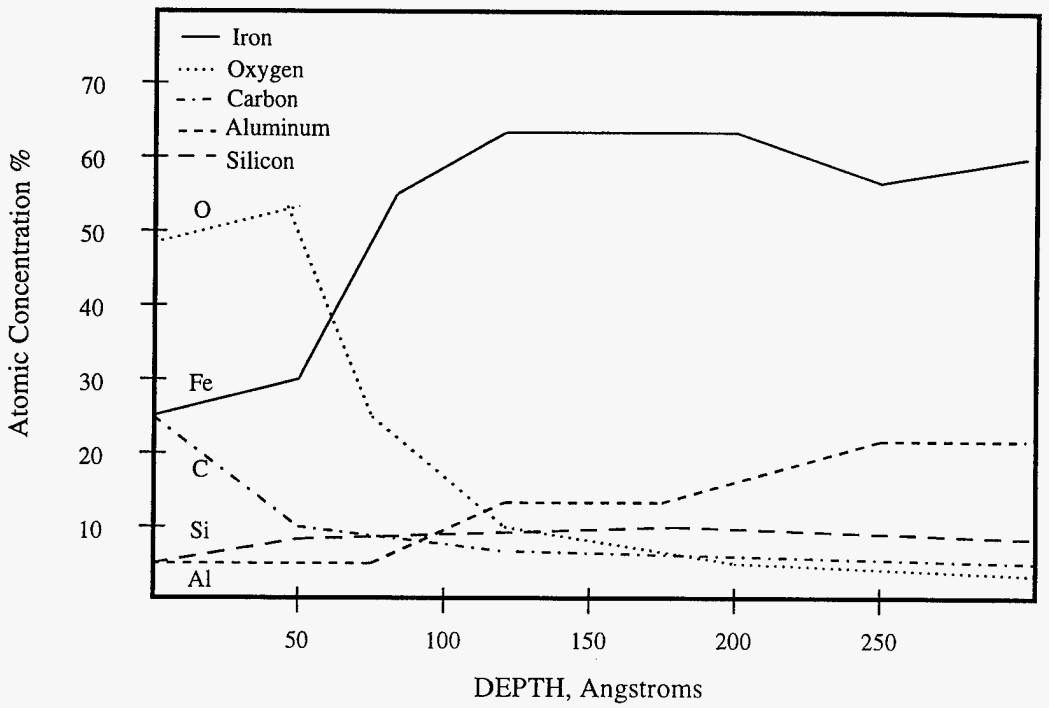

Figure 3.4 - Auger electron spectrograph of Fe-15Al-2.8Si with sputtering distance

The powder distribution used for sintering evaluation was examined by SEM shown in Figures 3.5. The powders appear uniform and spherical with no obvious geometric anomalies. The air classified size distributions used for vacuum sintering is shown in Figure 3.6 and the powder size distribution used for P/M extrusion is shown in Figure 3.7. The sintered powder size distributions in Figure 3.6 had median particle sizes (D_{50}) ranging from 16 μm to 18 μm. However, the powder size distributions were narrower for the Fe-15Al-2.8Si and Fe-15Al-5Si in comparison with the Fe-15Al alloy powder. The D_{84} for the finer sintering powders ranged from 27 μm to 34 μm. These subtle differences in size distribution may account for the different tap densities. The size distribution of coarser powders shown in Figure 3.7 were used for extrusion had median particle size of 32 μm. The coarse powders had a lower oxygen content of 150 ppm compared to the 300 ppm in the fine powder due the increased surface area. The oxygen reacts with the aluminum to form aluminum rich oxides, which can increase the flow stress and reduce the ductility. The morphology of the oxide has an important effect on mechanical properties, and the oxide is developed during the consolidation processing. The oxide distribution will be discussed as part of the consolidated product characterization.

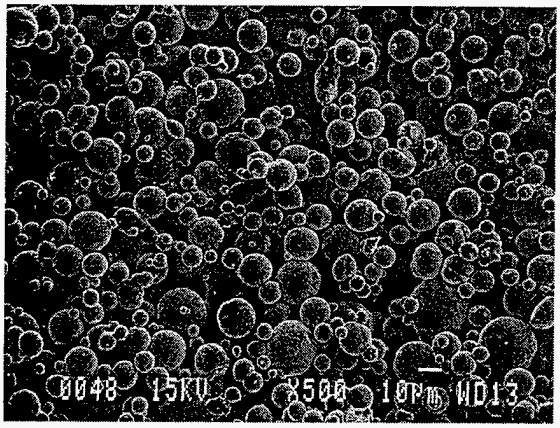

Figure 3.5 - SEM micrograph of Fe-15Al-2.8Si powder distribution

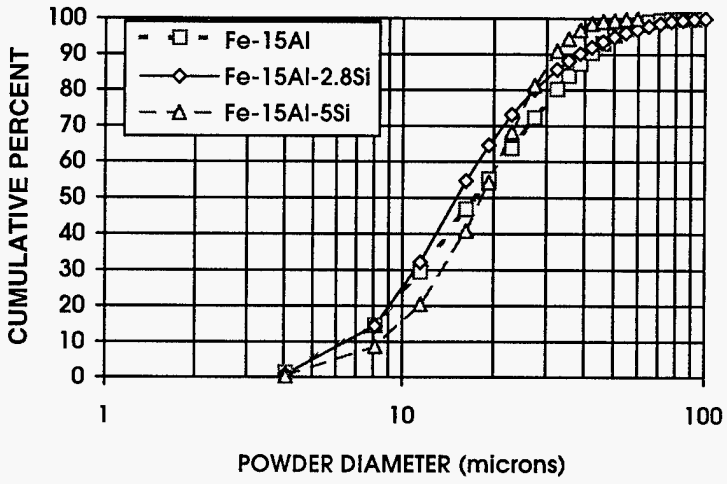

Figure 3.6 - Powder size distribution for sintering from air-classified Fe-Al-Si alloys

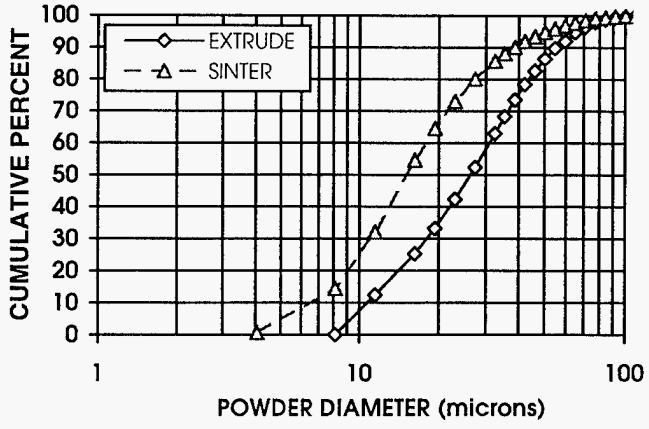

Figure 3.7 - Powder size distributions of Fe-15Al-2.8Si for Acucut air classified fine powder used in vacuum sintering and coarse powder used for powder extrusion

Powder Solidification Structure

The SEM examination of the atomized powders to determine cell size and grain size revealed a strong dependence on alloy content shown in Figure 3.8 and Figure 3.9. Figure 3.8 shows the grain size and cell size observed by SEM examination in a few typical particles approximately 20 μm in diameter for all three alloys. The binary alloy powder had a grain size of approximately 20 μm and a cell size of 10 μm. The powder grain structure in the Fe-Al-Si alloys were similar each having grain sizes less than 10 μm and cell sizes less than 3 μm. The silicon appeared to change the energy balance between chemical potential and solid/liquid interfacial energy, and promoted refinement of the as-solidified microstructure. The finer initial grain sizes in the powders were anticipated to improve the densification rate due to higher driving forces from smaller microstructural features and the higher diffusivity along increased grain boundary area.

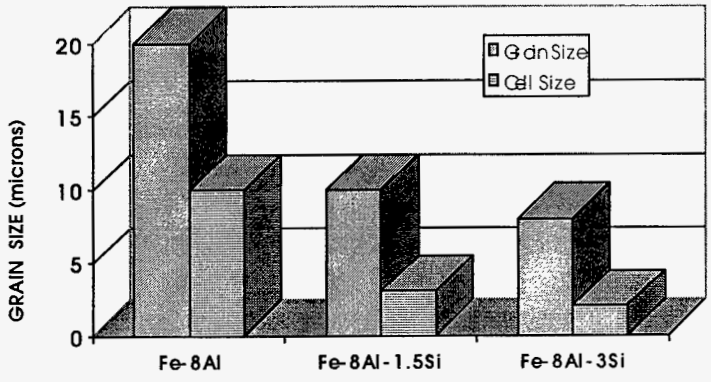

Figure 3.8 - Average grain size and cell Size for a 20 micron as-solidified powder particle

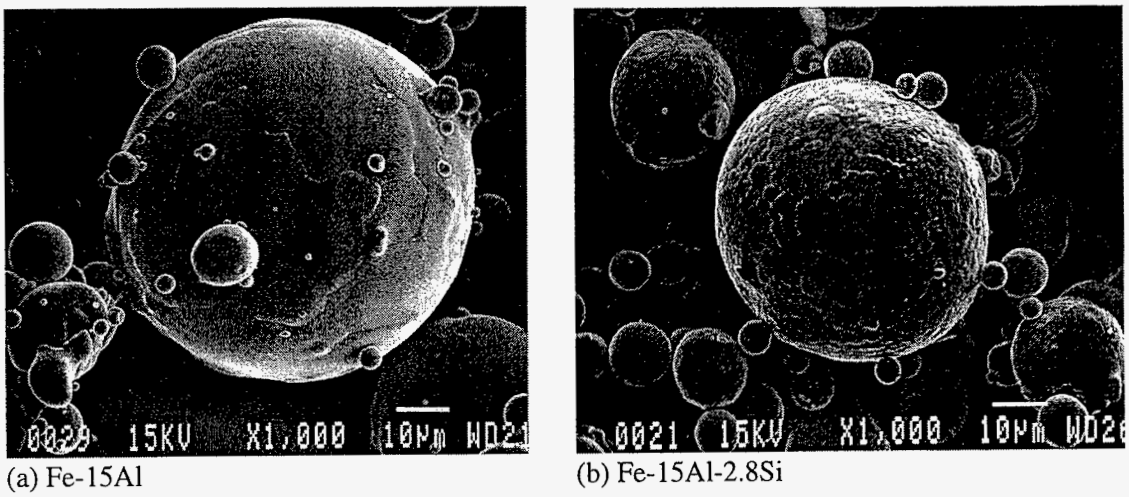

(a) Fe-15Al (b) Fe-15Al-2.8Si

Figure 3.9 - SEM micrograph of effect of silicon addition on cell size in HPGA powder particles

The differential thermal analysis (DTA) of the binary alloy of Fe-15Al was consistent with the published values for Fe-Al phase binary phase diagram. The differential thermal analysis results shown in Table 3.4 revealed a liquidus reduction of 10°C per atomic percent silicon and a solidus depression of 18°C per atomic percent silicon to a maximum of 53°C. The melting range also increased approximately 18°C per atomic percent silicon addition.

Table 3.4 - DTA Melting Data for HPGA Powders
(Heating Rate: 10°C/min)

Alloy	Solidus	Liquidus	Melting Range
Fe-15Al	1518°C	1528°C	10°C
Fe-15Al-2.8Si	1468°C	1500°C	32°C
Fe-15Al-5Si	1430°C	1475°C	45°C

The DTA results show that there was no liquid present below 1430°C, which assured that all vacuum sintering experiments below 1400°C were conducted in the solid state. Since the liquidus was reduced with silicon, and the melt pouring temperature for atomization was fixed at 1725°C for all alloys, the relative superheat of the silicon containing alloys was higher. Although not likely, the difference in superheat may have affected the solidification structure within each powder particle, and the physical properties of the liquid such as surface tension and viscosity, which play a role in particle size distribution.

The theoretical density of each alloy was determined on machined as-extruded bars by a helium pycnometer and precision balance. The addition of silicon reduced the theoretical density of the Fe-15Al powder from 7.08 g/cm^3 to 6.97 g/cm^3 in the Fe-15Al-5Si. The apparent density and the tap density for each alloy powder on the size distribution used for vacuum sintering are shown in Table 3.5. The tap density ranged from 63% in the Fe-15Al powder to 67% of theoretical density for the Fe-15Al-5Si powder. Although the HPGA powders are generally spherical, the tap density can be affected by surface anomalies such as satellites. The tap density may also be affected by particle packing efficiency of the size distribution of the powder sample. A tap density of approximately 65% reasonably simulates a loading fraction from a typical MIM product. Although the tap density is a reasonable predictor of sintering behavior, other factors such as surface energy, diffusivity of active species and total surface area may play a more dominant role.

Table 3.5 - Density of Fe-Al-Si Powders

Alloy	Theoretical Density [g/cm^3]	Apparent Density [g/cm^3]	Tap Density [g/cm^3]	Tap Density % T.D.
Fe-15Al	7.08	3.35	4.45	63%
Fe-15Al-2.8Si	7.01	3.77	4.58	65%
Fe-15Al-5Si	6.97	3.82	4.69	67%

Chemistry of Consolidated Powers

The chemistry of the consolidated powders is shown in Table 3.6. The aluminum and silicon contents were unchanged from the atomized powder. The oxygen levels ranged from 280 ppm to 375 ppm, and the sulfur content was maintained at less than 20 ppm. The extruded powder showed an increase in carbon level compared to the base powders in all three alloys of approximately 50 ppm to up to a maximum of 228 ppm in the extruded Fe-15Al-2.5Si. The increase in carbon of the extruded samples was potentially from the pre-consolidation heat treatment after canning.

Table 3.6 - Chemistry of Consolidated Alloys (ICP)

Nominal Composition	Al (at%)	Si (at%)	O (ppmw)	N (ppmw)	C (ppmw)	S (ppmw)	P (ppmw)
Fe-15Al	14.94	0.015	375	19	139	10	40
Fe-15Al-2.8Si	15.02	2.85	280	7	228	9	50
Sinter 1200°C	15.02	2.85	339	6	56	10	40
Fe-15Al-5Si	14.63	5.03	284	6	76	20	30

Vacuum Sintering

The densification response of the vacuum sintered Fe-Al-Si alloys is shown in Figure 3.10 and Figure 3.11. Figure 3.10 shows the densification measured by dimensional change of each alloy sample held for 2 hours at each temperature. The Fe-15Al alloy developed the highest theoretical density of 95% at the 1200°C, while the silicon bearing densified to less than 90% of theoretical density. Figure 3.11 shows the effect of time at 1200°C on the densification of each alloy measured by dimensional analysis of the sintered and machined cylinders. The binary alloy densified more rapidly during the initial stages of sintering, but the ternary alloy achieved similar density after 5 hours at temperature. As an influence on sintering, the significance of the silicon level is unclear from these data, but the presence of silicon does distinctly depress the intial stages of sintering.

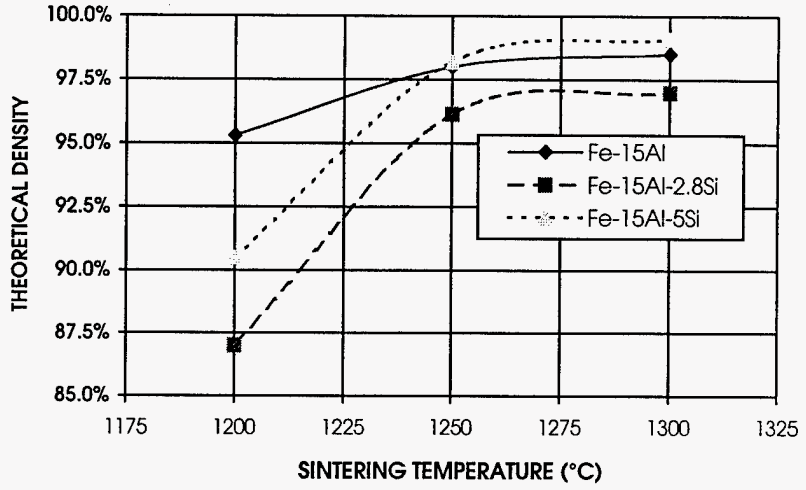

Figure 3.10 - Temperature effect on theoretical density of Fe-Al-Si powder alloys with a 2.0 hour sintering cycle in 10^{-6} torr vacuum

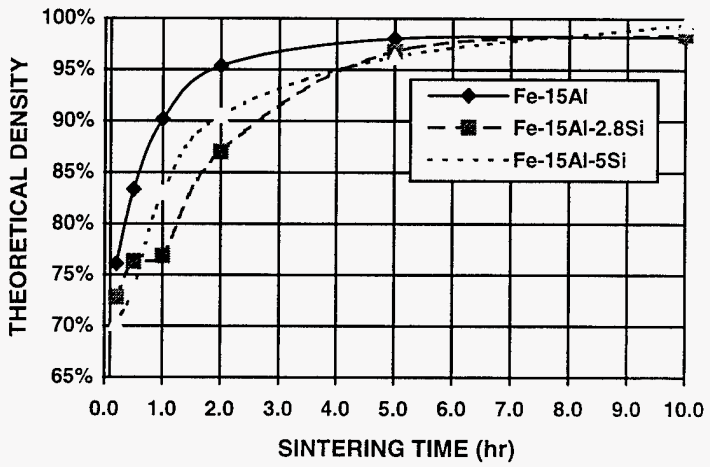

Figure 3.11 - Time effect on theoretical density of Fe-Al-Si powders at 1200°C at10^{-6} torr

Figure 3.12 shows the measured grain size at each sintering temperature, while Figure 3.13 and Figure 3.14 shows the ranges of grain sizes developed in the Fe-15Al and Fe-15Al-5Si alloys at 1200°C, 1250°C and 1300°C. The grain sizes in samples sintered at 1200°C were uniformly equiaxed and similar in size ranging from 29μm to 37 μm . The pores in the 1200°C samples were observed at grain boundaries, which apparently assisted grain boundary pinning. At 1250°C, the grain size appeared duplex as pores were reduced, and non-uniform grain growth was observed randomly throughout the microstructure. At 1300°C, the pores throughout the microstructure were almost completely eliminated and most grains grew to greater than 100 μm.

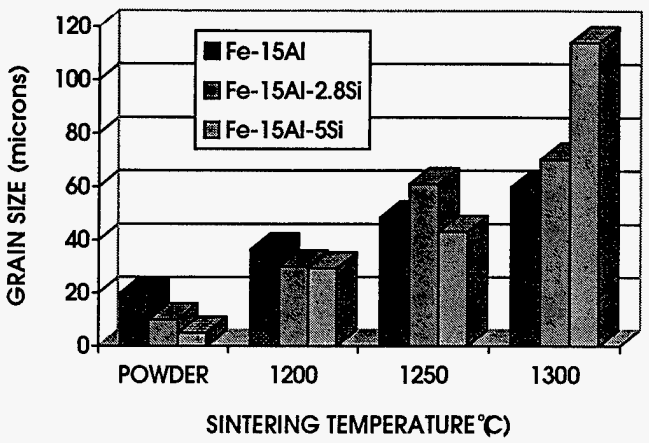

Figure 3.12 - Grain Growth of Fe-Al-Si Powder Alloys vacuum sintered 2 hours

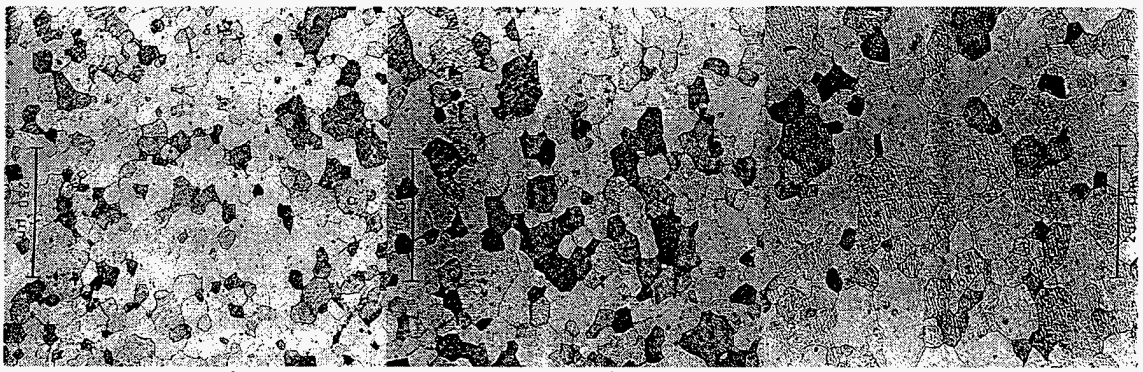

(a) 1200°C (b) 1250°C (c) 1300°C

Figure 3.13 - Grain Size of Vacuum Sintered Fe-15Al

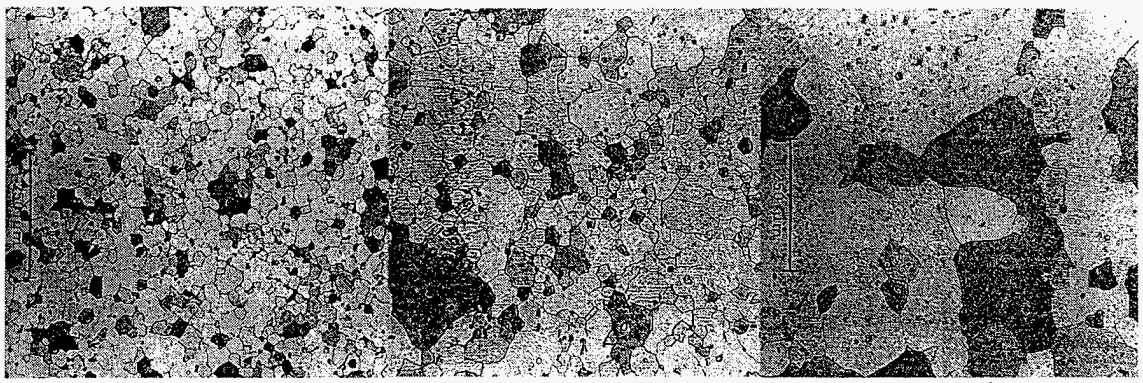

(a) 1200°C (b) 1250°C (c) 1300°C

Figure 3.14 - Grain Size of Vacuum Sintered Fe-15Al-5Si

The SEM images of the surfaces of isothermally sintered samples of the Fe-Al-Si samples are shown in Figure 3.15, Figure 3.16 and Figure 3.17. The surface of the 1100°C sintered sample shows neck formation between adjacent powder particles. The surface of the 1200°C sample shows a more dense material with isolated pores. The grain boundaries were observed at neck regions between coarsening particles. The surface of the samples sintered at 1300°C had less porosity, and an interesting faceting feature characteristic of the silicon containing powders. A gradual curved faceting was observed in the Fe-15Al sample, but a sharper and more angular faceting was observed in the Fe-15Al-5Si sample. Such "thermal faceting" is a result of a change in surface energy as a function of specific crystallographic orientation [37].

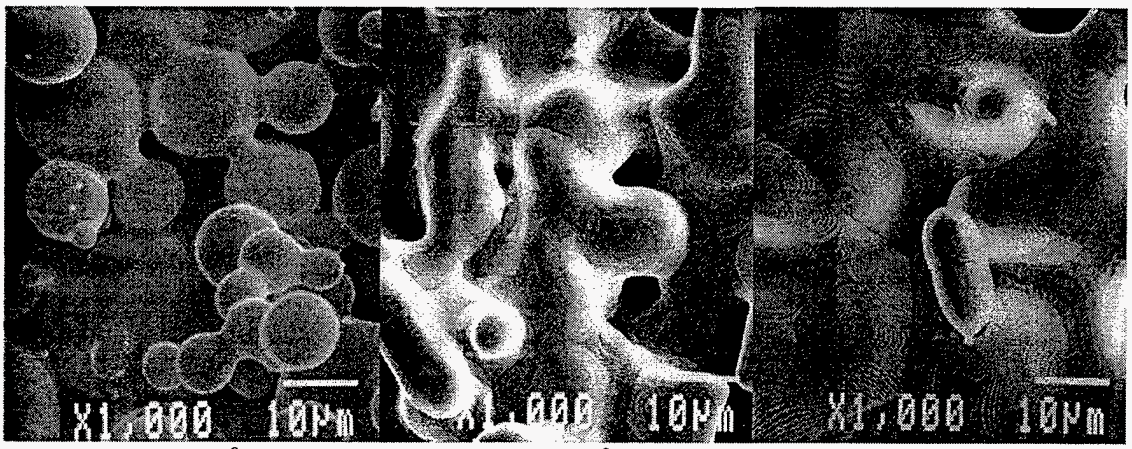

(a) 1100°C (b) 1200°C (c) 1300°C

Figure 3.15 - SEM of Surface Topology for Vacuum Sintered Fe-15Al

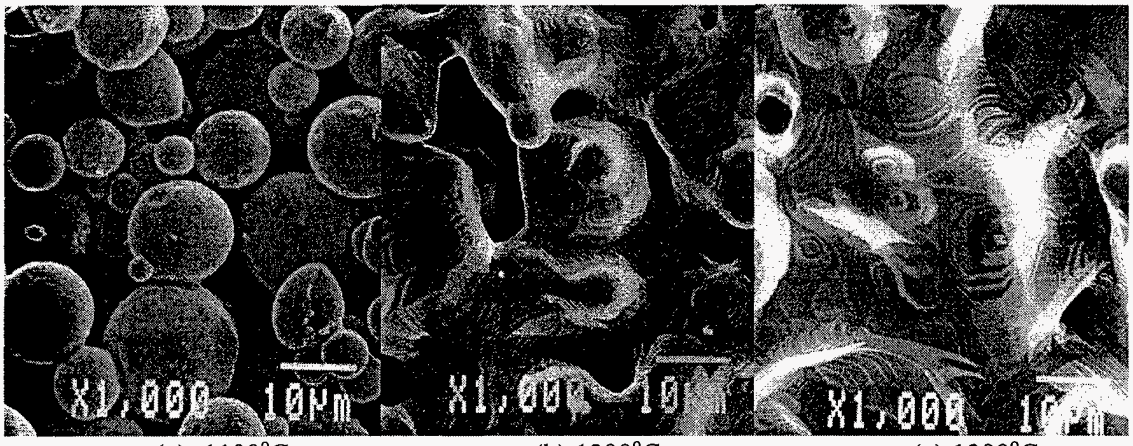

(a) 1100°C (b) 1200°C (c) 1300°C

Figure 3.16 - SEM of Surface Topology for Vacuum Sintered Fe-15Al-2.8Si

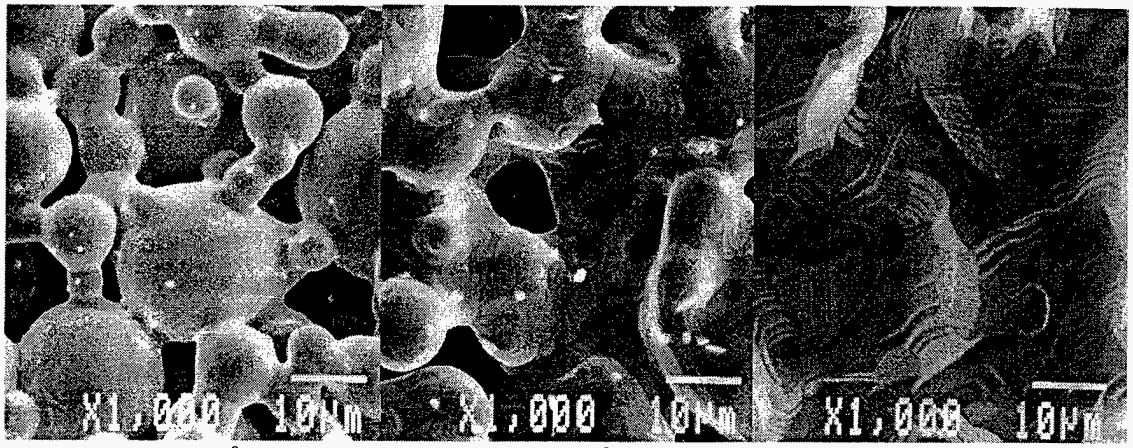

(a) 1100°C (b) 1200°C (c) 1300°C

Figure 3.17 - SEM of Surface Topology for Vacuum Sintered Fe-15Al-5Si

The addition of silicon appeared to reduce the surface energy along a number of low index planes compared with only a very few low energy planes in the Fe-15Al alloy. The change in surface energy may have affected on both the densification rate and the grain growth. Figure 3.18 shows isolated powder particles in Fe-15Al-2.8Si, which have the faceting planes identified by crystal symmetry. The 3-fold symmetry of the (111) plane and the 4-fold symmetry of the (100) plane are very distinctive.

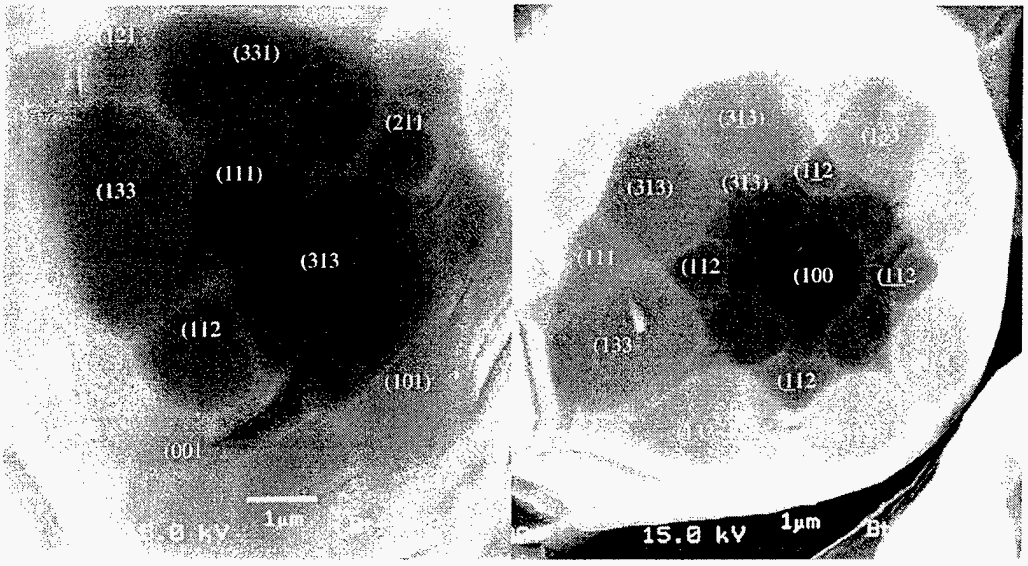

(a) 3-fold symmetry (111) normal (b) 4-fold symmetry (100) normal

Figure 3.18 - Index planes of Fe-15Al-2.8Si sintered powder particles

Table 3.7 - Image analysis on theoretical density in Fe-15Al-xSi

Alloy	Sintering Temperature	% Theoretical Density (Ave. ± std. dev.)
Fe-15Al	1100 °C	73.1 ± 1.9
	1150 °C	82.2 ± 2.6
	1200 °C	94.2 ± 2.2
Fe-15Al-2.8Si	1100 °C	64.2 ± 3.0
	1150 °C	73.6 ± 0.2
	1200 °C	93.5 ± 0.5
Fe-15Al-5Si	1100 °C	62.9 ± 2.9
	1150 °C	76.8 ± 2.4
	1200 °C	81.7 ± 1.8

A secondary point of interest in SEM surface images are the small oxide particles, which appeared to increase in frequency with the silicon content. The small particles, less than 1 micron in diameter, are not random inclusions, but are believed to be an equilibrated product of the thin surface oxide (100 Å) that existed on the surface on the as-atomized powder. A possible mechanism of formation involves the cracking of the oxide layer to form discrete islands of oxide due to incompatible thermal expansion at the metal/oxide interface. The islands of oxide film probably minimized their surface energy by coarsening forming the observed spherical particles. The particles were not observed at temperatures above 1250°C. This may indicate an absorption into the metal, or volatilization at higher temperatures in the high vacuum environment. The understanding of the process conditions, and mechanisms for formation and elimination for these particles may provide insight on reduction of prior particle boundary oxides in sintered powders of this alloy family.

P/M Extrusion

The hot P/M extrusion was successful in consolidating the powders to essentially full density. The grain structures are shown in the longitudinal orientation in Figure 3.19, Figure 3.20 and Figure 3.21. The equiaxed grain structure viewed in this orientation indicated a dynamically recrystallized structure common to such hot worked products. The grain sizes in the extrusion ranged from 32 μm in the Fe-15Al extrusion to 50 μm in the Fe-15Al-2.8Si extrusion. The grain size of the extrusions and sintered samples are shown in Table 3.8.

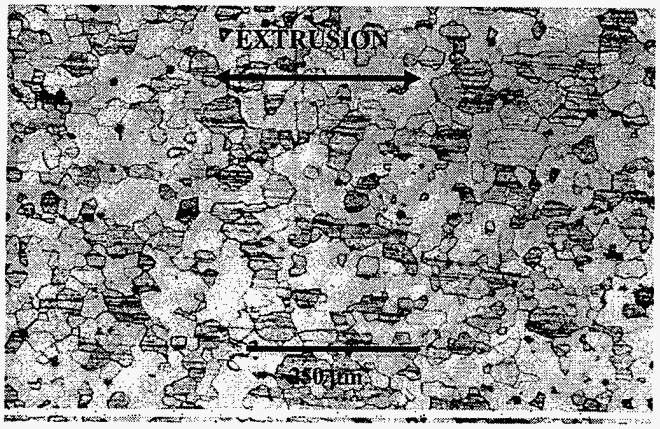

Figure 3.19 - Longitudinal orientation of grain structure of extruded Fe-15Al

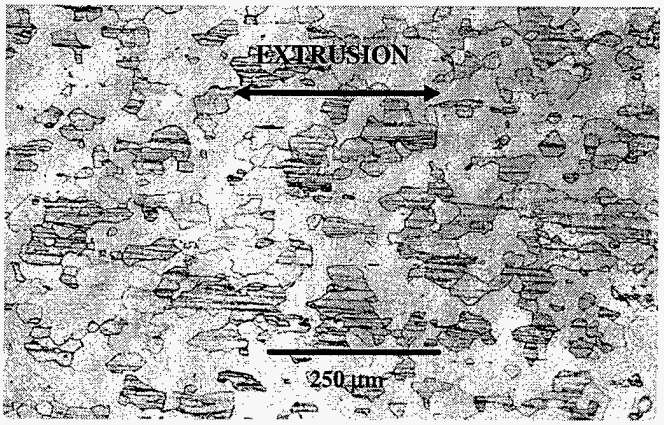

Figure 3.20 - Longitudinal orientation of grain structure of extruded Fe-15Al-2.8Si

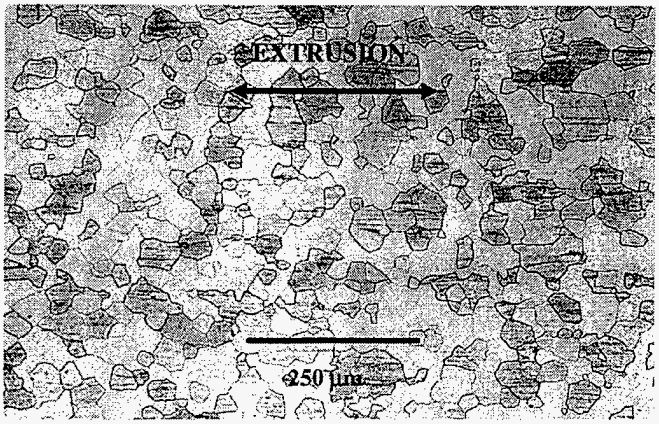

Figure 3.21 - Longitudinal orientation of grain structure of extruded Fe-15Al-5Si

Table 3.8 - Grain Size and Theoretical Density of Fe-15Al-xSi Extrusions and Sintered Powders

ALLOY	SINTERING TEMPERATURE	GRAIN SIZE (microns)	% THEORETICAL DENSITY
Fe-15Al	extrusion	32.3 ± 2.7	100
Fe-15Al-2.8Si	1200°C	26.7 ± 4.3	87
	1300°C	73.6 ± 6.7	97
	extrusion	50.0 ± 3.5	100
Fe-15Al-5.0Si	extrusion	33.8 ± 4.6	100

Dark streaks appeared in the extrusion direction in the structures of all three alloys. Examination by SEM, shown in Figure 3.22, revealed the dark lines to extend through grains and across grain boundaries, which correspond to the elongation of prior particle oxides boundaries. The surface relief between grains was generated by the differential etching conditions of grain orientation. The EDS analysis of these particles, shown in Figure 3.23, show the enrichment of oxygen, iron aluminum and silicon. The EDS suggests the formation of the ferro-alumino-silicate on the powders contained within steel cans during heating prior to extrusion.

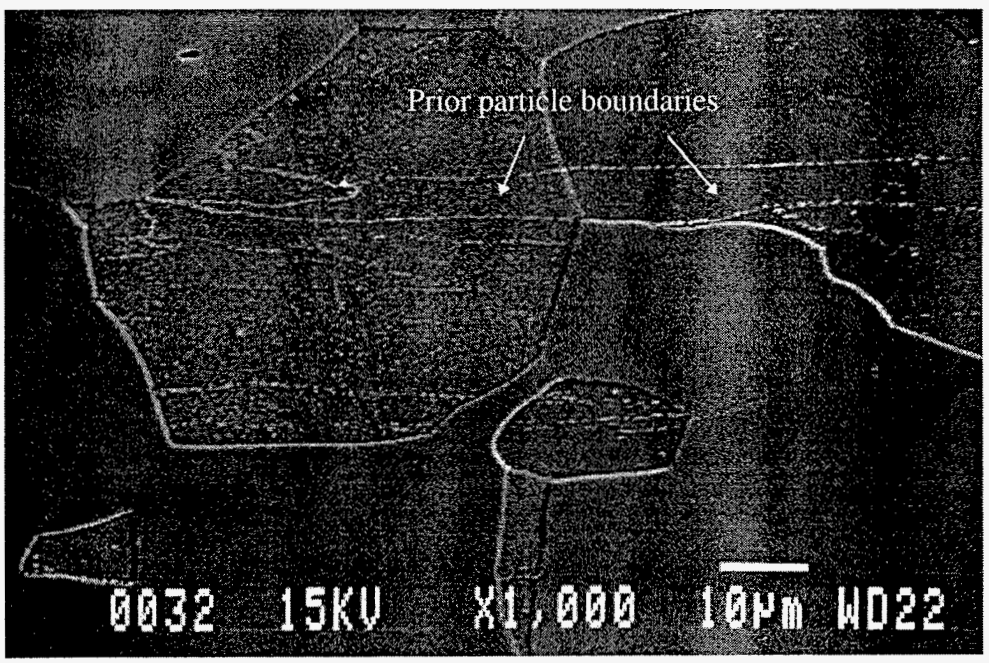

Figure 3.22 - SEM of prior particle boundaries in extrusion

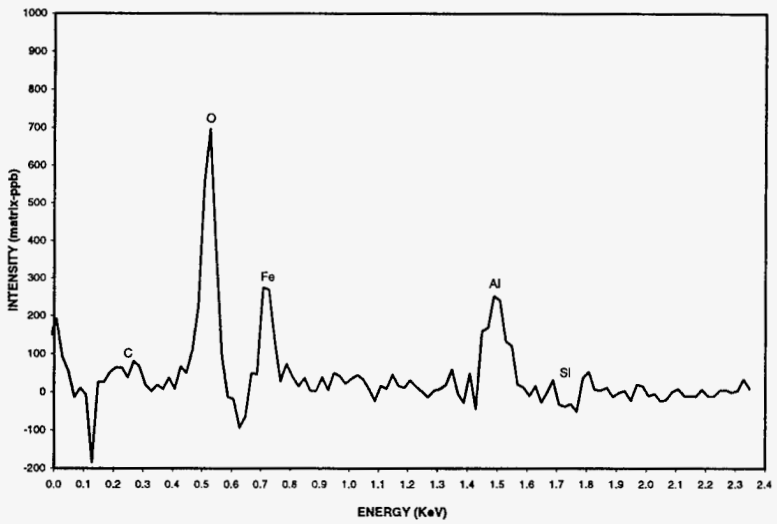

Figure 3.23 - EDS spectra of prior particle boundaries - matrix spectra at 5 kV

Texture Measurement

Figure 3.24 shows a summary of x-ray diffraction data comparing the Bragg reflections over the same range of two theta range of as-extruded samples, sectioned in the longitudinal and transverse orientations to the extrusion direction, and a vacuum sintered sample. The sintered sample represents a baseline of randomly oriented grains, so the diffraction data reveals a relative peak intensity profile similar to the standard pattern for BCC iron. The solitary {110} peak observed in the data taken parallel to the extrusion indicated that in the extruded bar the {110} planes are aligned in the extruded direction. Pole figures of each alloy taken on longitudinal sections of extruded samples also revealed a strong {110} wire texture, which is common for BCC metals [23]. Table 3.9 shows the enhanced magnitude intensity of the peak intensity at the central pole. The detailed comparison between the two theta x-ray diffraction scans at the various extrusion orientations and the sintered sample was performed only on the Fe-15Al-2.8Si alloys, because this alloy was subject to the most subsequent testing of mechanical properties. Since tensile samples of single crystal BCC metals aligned in {110} orientation have been observed to produce yield strengths up to two times the yield strength observed in the soft orientations such as the {100} [28], sample texture must be taken into account when comparing mechanical property test results.

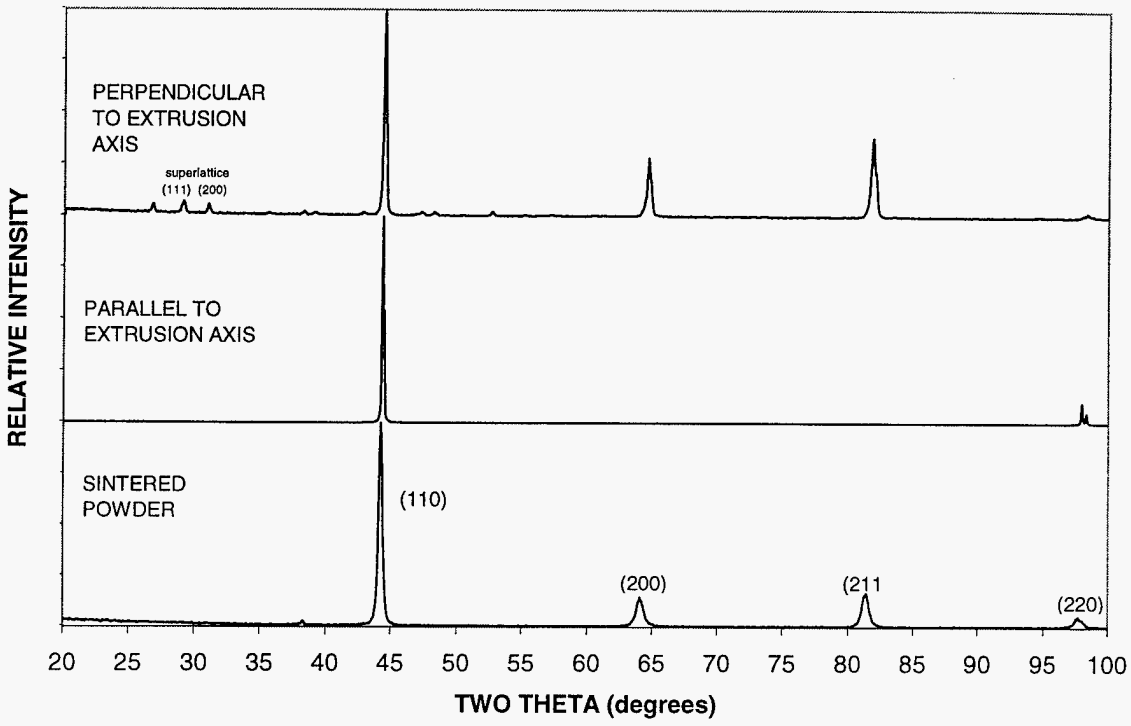

Figure 3.24 - X-ray diffraction of Fe-15Al-2.8Si in the as-extruded and sintered condition

Figure 3.9 - Intensity enhancement randomness at origin in (110) pole figure

ALLOY	INTENSITY ENHANCEMENT RATIO
Fe-15Al	14.12
Fe-15Al-2.8Si	14.29
Fe-15Al-5Si	3.34

The superlattice peaks for Fe_3Al were observed at 26.75° and 30.95° in the perpendicular direction in the as-extruded sample, which may indicate some preferred orientation relationship between the ordered α and disordered DO_3. The antiphase boundaries have been determined by other investigators to be a matching along (100) planes, which may explain the slightly higher peaks for the (200) and (211) planes. The additional small peaks were found to correspond to $FeAl_2O_4$ (hercanite)and $FeSi_2O_4$ (fayalite) as shown in Table 3.10, and mentioned previously in the description of the extruded microstructures in Figure 3.22.

Table 3.10 - X-ray diffractometer scan of extruded Fe-15Al-2.8Si in the transverse direction

Two Theta (degrees)	Intensity (percent)	D-spacing (angstrom)	Fe - BCC	Fe_3Al	$FeAl_2O_4$	Fe_2Si0_4
26.75	6	3.33		111		111
29.05	7	3.07			220	
30.95	6	2.89		200		O31
35.55	1.5	2.52			311	211
38.25	2	2.35				221
39.15	2	2.30				O41
42.80	2	2.11			400	
44.40	100	2.04	110	220		
47.20	2	1.92			331	
48.20	2	1.89				311
52.65	2.5	1.74		311		
55.10	1	1.67		222		
57.25	1	1.61			511	
64.70	28	1.44	200	400		
81.75	37	1.18	221	422		
98.35	2.5	1.02	220	440		

Hot Stage TEM

Microstructural analysis of the as-extruded Fe-15Al-2.8Si at ambient temperature shows very small (<10 nm) spherical ordered regions using TEM dark field imaging shown in Figure 3.25. Selected area electron diffraction patterns from Fe-15Al-2.8Si and Fe-15Al-5Si at ambient temperature also show superlattice reflections for DO_3. Figure 3.26 shows the 111 and 200 superlattice reflections of the DO_3 phase were visible in Fe-15Al-2.8Si up to 400°C. At 600°C the superlattice reflections became nearly extinct, which indicated nearly complete disorder. Figure 3.27 shows microstructure at ambient temperature of the Fe-15Al-5Si extrusion in the heat treated condition of 600°C/7days, which developed a basket weave microstructure comprised of rectangular shaped features approximately 200 nm across, and narrow bands of another phase approximately 50 nm thick between the broad bands. Identification of the phases was conducted by imaging with various beam condition. The best contrast was observed with dark field using the 220 g-vector of the fundamental reflection, which illuminates the disordered material between the blocky ordered phases.

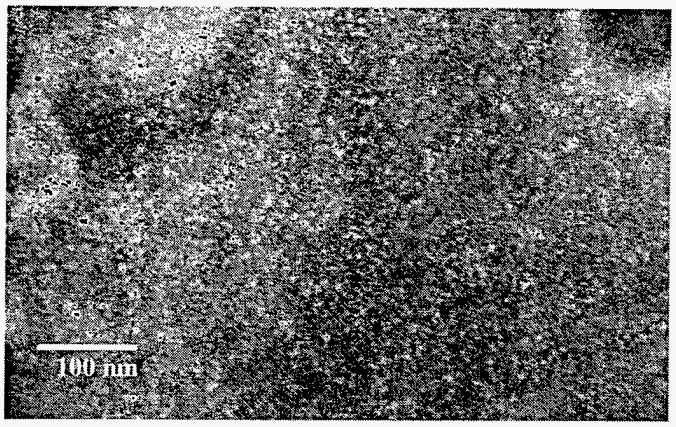

Figure 3.25 - TEM dark field image (g =111) DO_3 regions in as-extruded Fe-15Al-2.8Si

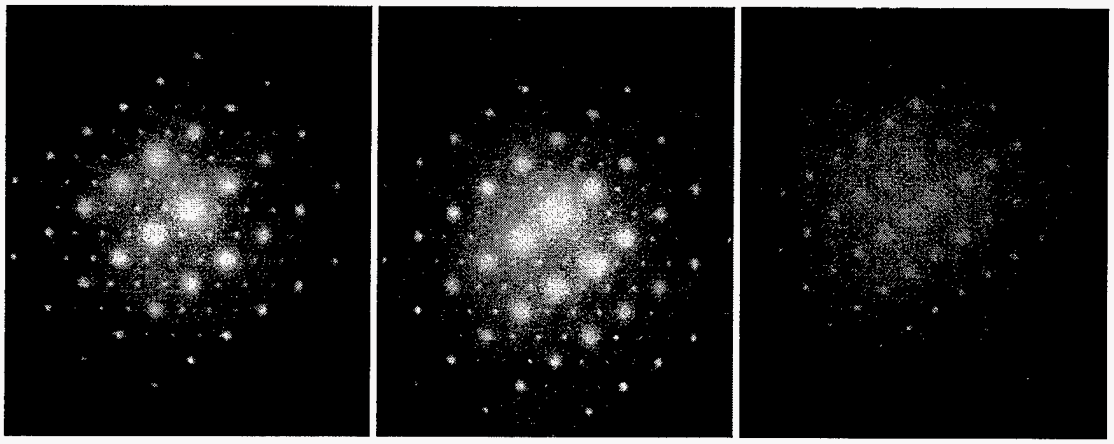

(a) Room Temperature (b) 400°C/1 hour (c) 600°C/1 hour

Figure 3.26 - Hot stage SAD pattern of the 110 zone axis Fe-15Al-2.8Si at temperature

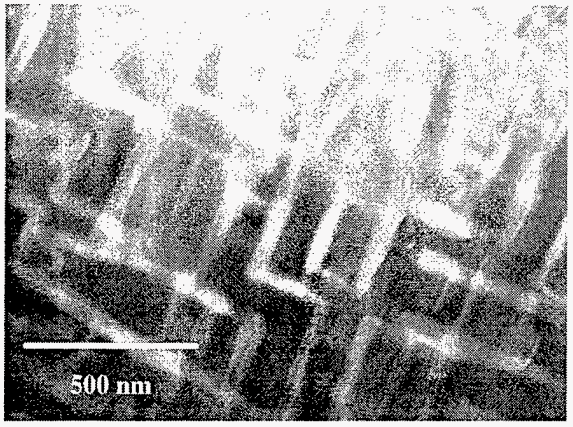

Figure 3.27 - TEM dark field 220 images of Fe-15Al-5Si (α+DO_3) structure at 600°C/ 7 days

Figure 3.28 shows the 111 and 200 superlattice reflections for the DO_3 phase, which were observed from room temperature up to 600°C. The 111 reflections disappeared at 800°C, which left the 200 reflections. This indicated the transition to the ordered B2 structure with a primitive cubic lattice between 600°C and 800°C. The transition to complete disorder was believed to occur above 800°C. Table 3.12 shows the observed reflections for the two materials analyzed. These results were important to help discern the effects of phase stability on the mechanical properties.

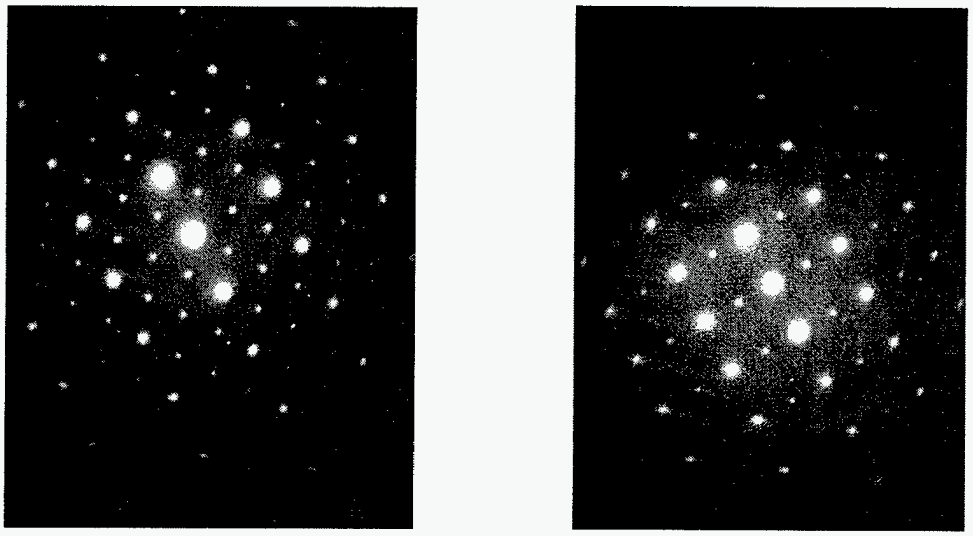

(a) 600°C/ 1.0 hour (b) 800°C/1.0 hour

Figure 3.28 - SAD patterns of 110 zone axis for Fe-15Al-5Si indicating $DO_3 \rightarrow$ B2 transition

Table 3.12 - Superlattice Reflections observed by Hot Stage TEM

Temperature (°C)	Fe-15Al-2.8Si	Fe-15Al-5.0Si
25 °C	med 111, 200	strong 111, 200
200 °C	med 111, 200	strong 111, 200
400 °C	med 111, 200	strong 111, 200
600 °C	very weak 111 200	med 111, 200
800 °C	n/a	weak (200)

Mechanical Properties

The punch test measurements of yield strength for each extruded alloy with a 600°C/7 day/WQ heat treatment is plotted as a function of temperature in Figure 3.29. The Fe-15Al alloy had the lowest yield strength of 300 MPa at 25°C, which decreased to less than 200 MPa above

300°C. The addition of 2.8 at.% silicon substantially increased the yield strength to 500 MPa at 25°C, and the yield strength was observed to continuously decrease above 200°C to 200 MPa at 550°C. The addition of 5 at. % silicon promoted transgranular cleavage from 25°C to 255°C, and the fracture occurred prior to plastic yielding. Presumably, if transgranular cleavage could be avoided, the yield strength trend would follow the dashed curve in Figure 3.29. At 355°C, the Fe-15Al-5Si material exhibited plastic yielding and the yield strength was observed to be 500 MPa. The high yield strength was observed to persist to 330 MPa at 550°C.

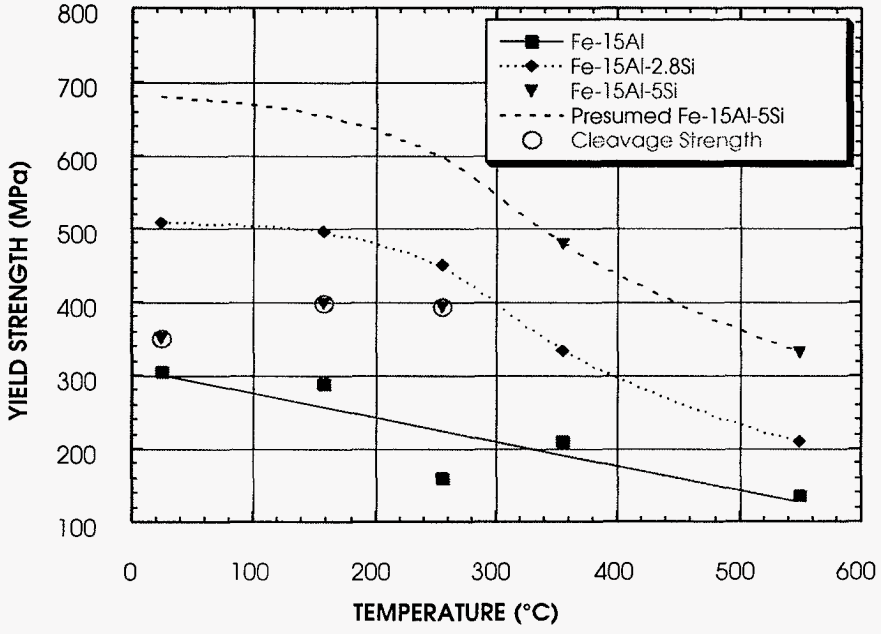

Figure 3.29 - Yield strength as a function of temperature for extruded Fe-15Al-xSi alloys (heat treatment: 600°C/7 days/WQ)

A dramatic difference was observed in the fracture energy as a function of temperature for the different alloys shown in Figure 3.30. The ductile-brittle transition temperature (DBTT) was determined as the temperature midway between the temperature bounding the lower energy shelf and the elevated temperature bounding the upper energy shelf. The DBTT for Fe-15Al was not observed during testing and was assumed to be below 25°C. The DBTT for Fe-15Al-2.8Si was approximately 80°C, and approximately 320°C for Fe-15Al-5Si. Above 155°C the fracture energy values of Fe-15Al and Fe-15Al-2.8Si were essentially the same, which may indicate a similar deformation mechanism at elevated temperatures. However, the fracture energy for Fe-15Al-5Si was 300 to 500 millijoules lower than the other alloys, which suggests a different deformation phenomena in this alloy compared with the other two.

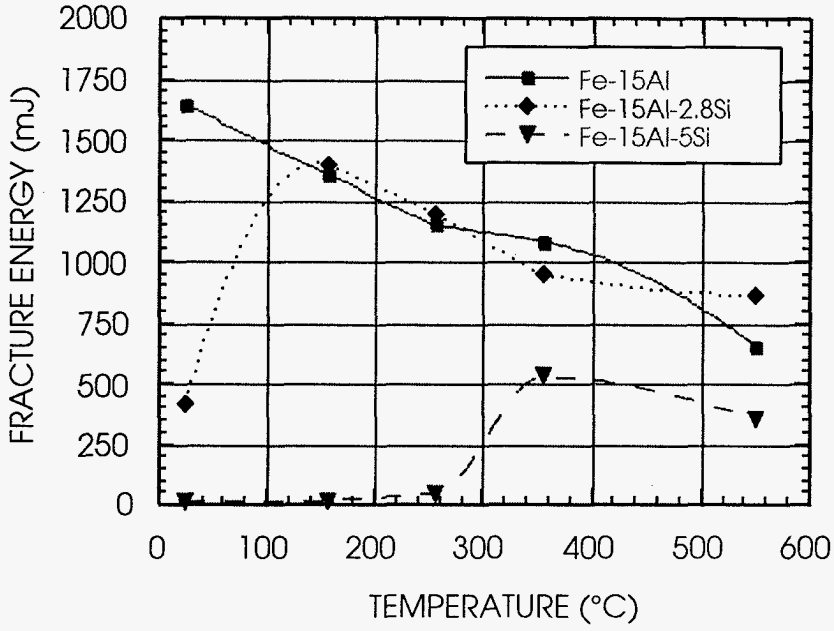

Figure 3.30 - Fracture energy of extruded Fe-15Al-xSi Alloys (heat treated at 600°C/7days/WQ)

Figure 3.31 shows the difference between the punch test yield strength of the as-extruded material and the alloys heat treated at 600°C for 7 days to develop an equilibrium structure. In both the Fe-15Al-2.8Si and Fe-15Al-5Si alloys the yield strength increased with the heat treatment. The highest yield strength at room temperature was observed in Fe-15Al-2.8 alloy due to the low cleavage strength of the Fe-15Al-5Si alloy as described previously. As the test temperature increased, an interesting phenomena was observed in the as-extruded material. A sharp drop in punch test yield strength from 500 MPa to 300 MPa was observed at about 150°C, while the heat treated material showed a modest decline in yield strength with increasing temperature.

Figure 3.32 shows the effects of the heat treatment at 600°C/7days/WQ on the extruded Fe-Al-Si alloys. The fracture energy for the Fe-15Al-2.8Si alloy improved, while the fracture energy reduced in the Fe-15Al-5Si with heat treatment at 600°C. The change in both fracture energy and yield strength was probably due to the change in long range order, which was observed by TEM as detail above. These alloy effects would be expected to follow the same behavior in sintered material. Therefore, the punch test behavior of only one alloy, Fe-15Al-5Si, was used to compare the differences in mechanical properties due to differences ordering of the microstructure from processing.

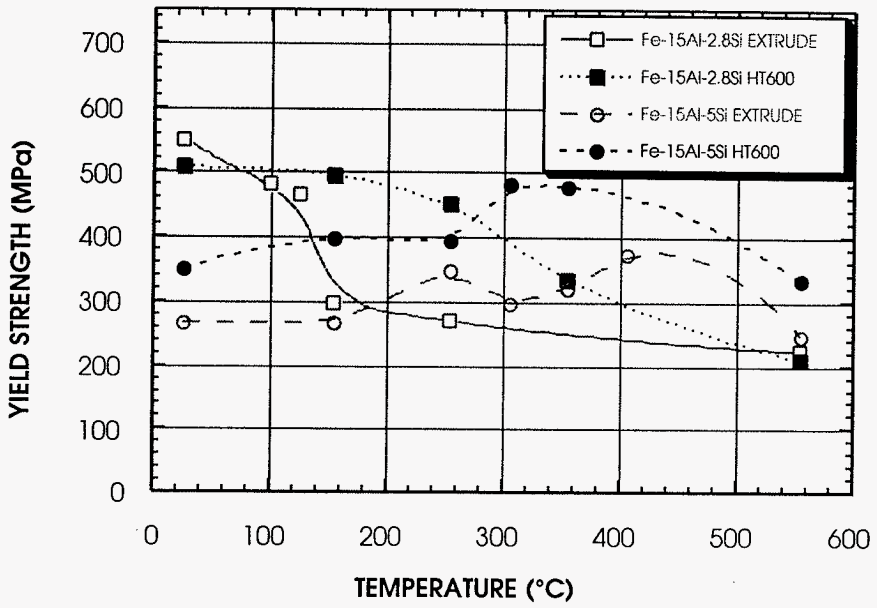

Figure 3.31 - Effect of 600°C heat treatment on punch Y.S. of extruded Fe-15Al-xSi alloys

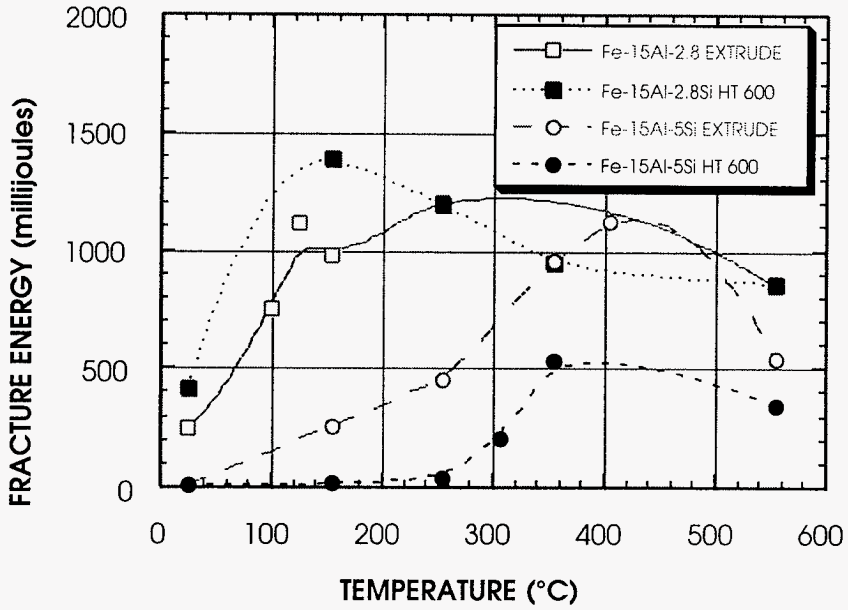

Figure 3.32 - Effect of 600°C heat treatment on punch E_f of Fe-15Al-xSi alloys

Figure 3.33 shows the effect of sinter processing on punch test yield strength of the Fe-15Al-2.8Si alloy, a representative alloy for this study, compared with the extruded material in the heat treated condition of 600°C/24hr/WQ. The sintered samples at 1200°C/2 hr and 1300°C/2 hr had porosity contents of 13% and 3% respectively. The average grain sizes were 27 μm for 1200°C sintered samples and 74 μm for 1300°C sintered samples. The pores were located primarily at grain boundaries in the sample sintered at 1200°C and the pores were approximately 10 μm in diameter. Since the grains had grown significantly while sintering at 1300°C, the pores were observed in grain interiors similar to those shown in Figure 3.13 (c). The punch test yield strength at 25°C of both sintered conditions was 400 MPa, compared with 500 MPa in the extruded material. However, both sintering conditions retained a yield strength of 300 MPa at 550°C, while the yield strength of extruded material was reduced to approximately 200 MPa at 550°C. Since texture was observed in the extruded material, the mechanical property dependence on sample orientation must be considered. The sintered samples contained a random grain orientation. Other differences in mechanical property behavior may be related to oxide distribution, or residual dislocation structure in the worked structure.

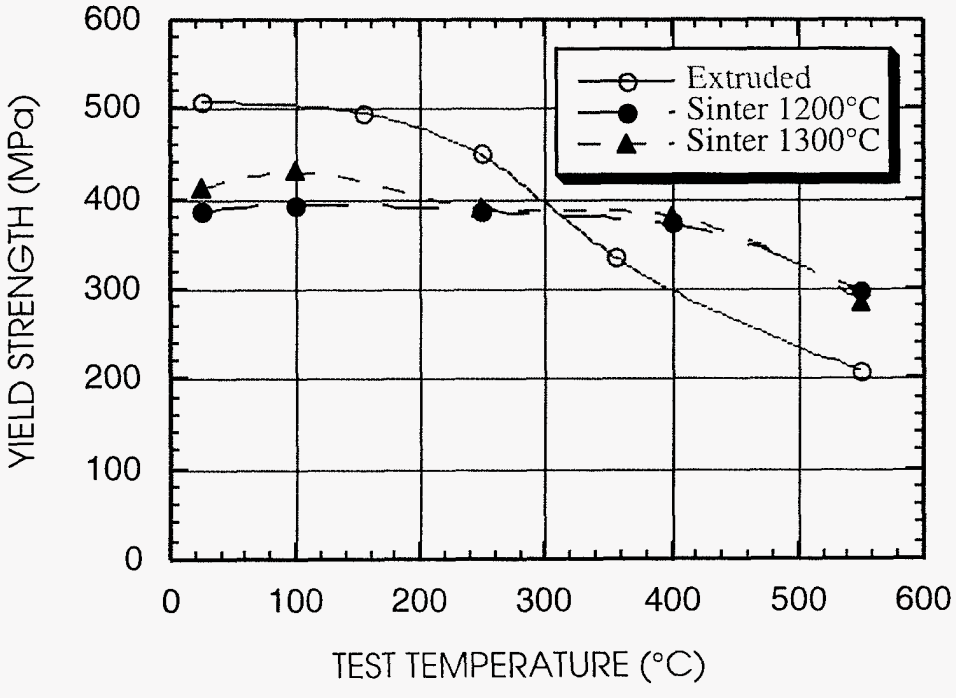

Figure 3.33 - Effect of processing on punch yield strength of Fe-15Al-2.8Si heat treated at 600°C

Figure 3.34 shows the fracture energy as a function of temperature for the same three process conditions described above. The extruded material obtained the highest room temperature fracture energy of 400 mJ, which was comparable to the increased yield strength presented in Figure 3.34. The sample sintered at 1200°C had much better fracture energy at 25 °C than the fracture energy of the sample sintered at 1300°C. The fracture energy advantage of the 1200°C sintering process continued at all test temperatures. The grain size, pore size and volume fraction are all suspected to play a role in determining the fracture behavior of these alloys.

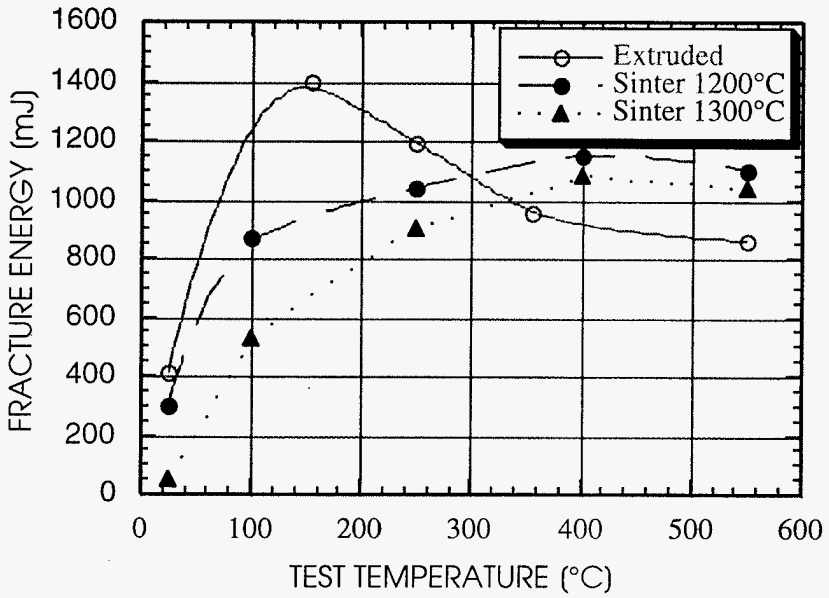

Figure 3.34 - Effect of processing on fracture energy Fe-15Al-2.8 Si powders (HT: 600°C)

SEM Fracture Examination

The fracture surface of the punch tested disks were examined using a scanning electron microscope. The crack location and orientation was observed at low magnifications of 20x, while the microscopic fracture features were observed at magnifications greater than 500x. The two fracture features which indicated fracture toughness in a punch test were the radial distance of the crack from the center, and the surface slip lines or cleavage features. The room temperature fractures are shown in Figure 3.35 for as-extruded Fe-15Al, Figure 3.36 for as-extruded Fe-15Al-2.8Si and Figure 3.37 for as-extruded Fe-15Al-5Si. Figure 3.35 shows the characteristics of the ductile fracture observed in Fe-15Al. The rumpled surface texture that developed was characteristic of "wavy slip" resulting from easy cross slip from the {110} planes to the {112} planes during extensive plastic

deformation [28]. The failure developed as a circumferential crack concentric with the specimen toward the outer edge of the disk. Figure 3.36 shows the limited plastic deformation developed in the Fe-15Al-2.8Si alloy at 25°C. The crack was elliptical in shape and closer to the center of the disk. The fracture surface revealed slip lines surrounding the crack with cleavage facets within the crack. Figure 3.38 indicates the very brittle nature of the Fe-15Al-5Si alloy. The radial cracks originated at the center of the disk, and the crack propagated toward the disk's outer edge. The fracture surface reveals the distinct transgranular cleavage mode. The crack was observed to change direction at grain boundaries to continue along the planes with the lowest cleavage strength. These room temperature fracture surface observations correlate to the fracture energy values shown in Figure 3.30 with Fe-15Al at 1640 mJ, Fe-15Al-2.8Si at 420 mJ and Fe-15Al-5Si at 14 mJ. At 550°C, intergranular failure was observed in the Fe-15Al-5Si sample, as shown in Figure 3.39, which corresponded to a decrease in fracture energy. A ductile transgranular fracture was observed in the other alloys tested at 550°C, and an example of the ductile-dimple features in Fe-15Al-2.8Si is shown in Figure 3.39.

Tensile Testing

The tensile tests on extruded Fe-15Al-xSi alloy powders showed similar trends as the punch tests, but the values for 0.2% yield strength and ultimate tensile strength were higher. Comparisons were made between the alloy effects and the heat treatment effects on each alloy. The addition of 2.8 at.% silicon produced a large increase in the yield strength at 25°C from 500 MPa to 865 MPa. A linear extrapolation of the silicon hardening trend predicted a yield strength of 1200 MPa for a 5 at.% addition. However, the addition of silicon to this level substantially lowers the cleavage strength , and the Fe-15Al-5Si alloy fails by transgranular cleavage prior to yielding. The tensile 0.2% offset yield strength of Fe-15Al was 500 MPa in the as-extruded condition, but the yield strength was reduced to 433 MPa upon heat treatment at 600°C for 24 hours. The UTS and ductility were unaffected by the heat treatment of this alloy. The tensile yield strength of Fe-15Al-2.8Si was 865 MPa in the as-extruded condition and was reduced to 846 MPa with the heat treatment at 600°C for 24 hours. The UTS at room temperature was slightly reduced from 941 MPa to 927 MPa. However, the room temperature ductility was significantly improved with the heat treatment of Fe-15Al-2.8Si at 600°C for 24 hours. The elongation increased from 2.9% to 7.5%, and the reduction in area increased from 5.9% to 11.7%. No room temperature data was determined on the Fe-15Al-5Si bars, because the bars failed in the hydraulic collet grips.

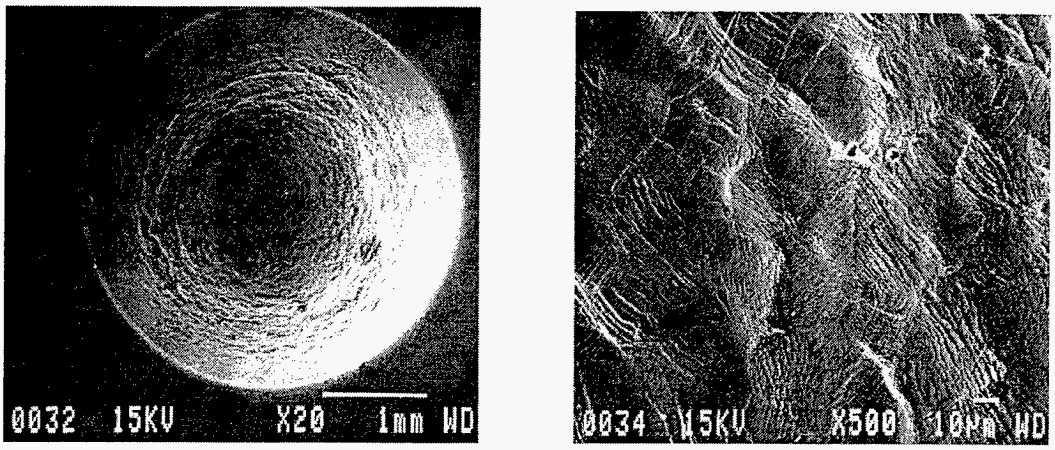

Figure 3.35 - SEM fracture of as-extruded Fe-15Al tested at 25°C

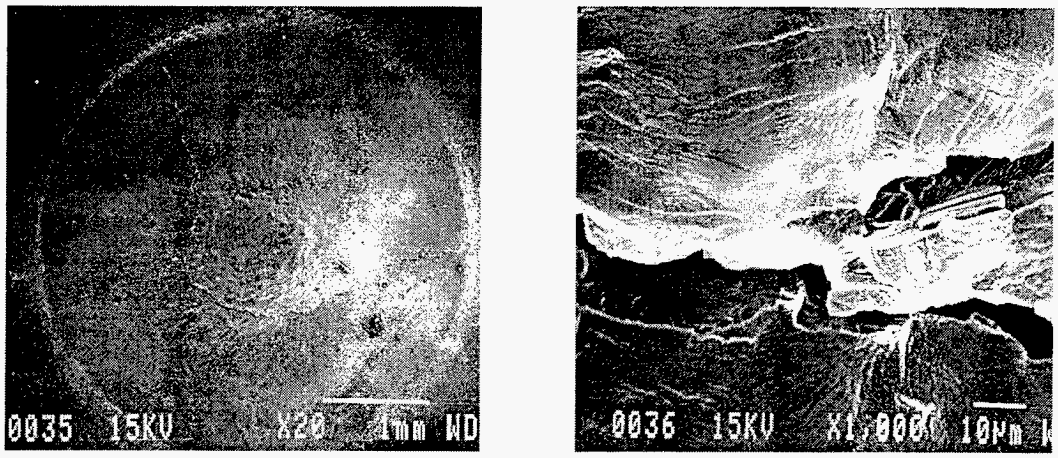

Figure 3.36 - SEM fracture of as-extruded Fe-15A-2.8Si tested at 25°C

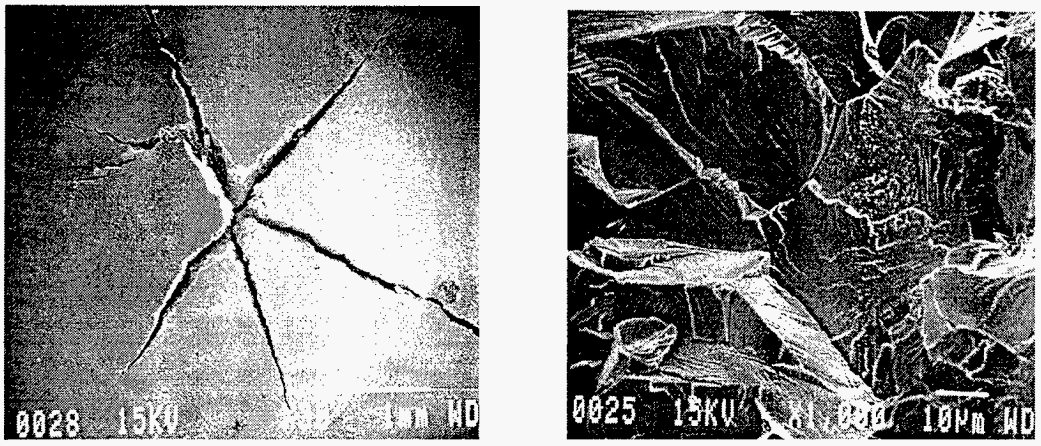

Figure 3.37 - SEM Fracture of as-extruded Fe-15Al-5Si tested at 25°C

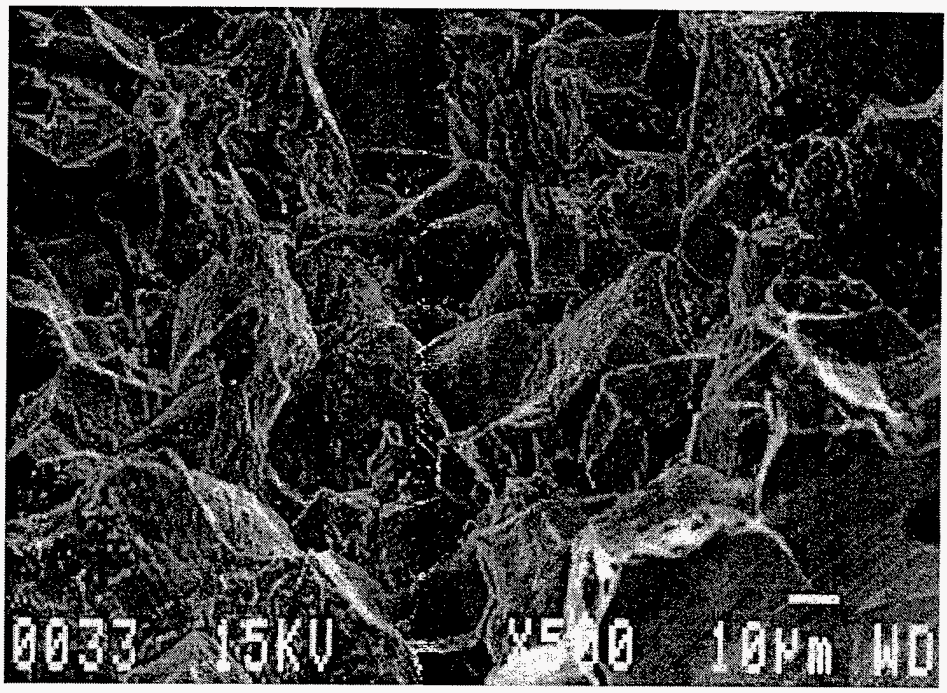

Figure 3.38 - Intergranular fracture in punch sample of Fe-15Al-5Si at 550°C

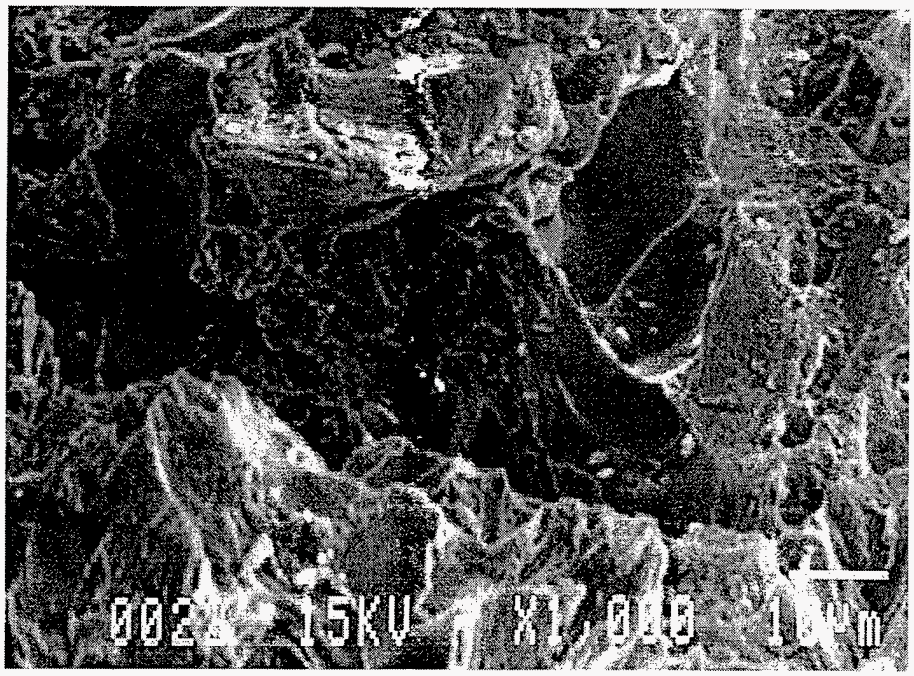

Figure 3.39 - Mixture of Ductile and transgranular cleavage fracture in Fe-15Al-2.8Si at 550°C

Table 3.9 - Tensile Test results for P/M extruded bars

ALLOY	CONDITION	TEST TEMP (°C)	UTS (MPa)	0.2% Y.S. (MPa)	%ELONG	% R of A
Fe-15Al	As-extruded	25 °C	573	500	28.9	80.2
	600°C/24hr	25 °C	572	433	28.7	80.4
	600°C/24hr	550 °C	254	254	16.4	26.3
Fe-15Al-2.8Si	As-extruded	25 °C	941	865	2.9	5.9
	600°C/24hr	25 °C	927	846	7.5	11.7
	As-extruded	550 °C	494	416	24.7	85.4
Fe-15Al-5Si	As-extruded	25 °C	na	na	nil	nil
	600°C/24hr	25 °C	na	na	nil	nil
	As-extruded	550 °C	670	572	21.9	89.0

The 0.2% yield strength at 550°C showed a marked increase with silicon additions. The effects of heat treatment could not be observed, because the bars designated for testing failed during machining. The trend was for the yield strength to increase from 254 MPa in the Fe-15Al alloy to 416 MPa in the Fe-15Al-2.8Si alloy to a maximum of 572 MPa in the Fe-15Al-5Si alloy. The ductility was consistent with the silicon bearing alloys between 22% to 25% elongation, while the binary alloy had a reduced ductility of 16.4 % elongation. However, the reduction in ductility may be an effect of the heat treatment, which promotes segregation of impurity species such s sulfur and phosphorus to the grain boundaries. The precipitation of oxides and carbides may be another embrittling effect.

CHAPTER 4. DISCUSSION

Alloy Screening

The diamond pyramid microhardness (DPH) data from arc cast buttons provided an initial indication of the flow stress and the toughness of the alloys. This hardness data quantified the strengthening effect of each elemental addition, and the DPH was useful for indicating the degree of ordering developed when evaluating the response to heat treatment. The Fe-15Al alloys with Si and Ti additions showed the highest resistance to indentation after a heat treatment at 500°C, consistent with the development of ordered intermetallic compounds described by Mikkola [4]. The material surrounding the diamond indentations for these alloys showed either microcracks or slip lines. The microcracks at the indent corners were a qualitative indication of easy cleavage fracture, whereas the slip lines revealed a degree of plasticity. Although the alloys containing titanium additions had the highest DPH values, microcracks developed at corners of the indentation. The Fe-Al binary alloys and Fe-Al-Si alloys developed revealed slip lines at the corners. A significantly increased DPH hardness with Si additions and evidence of plasticity made the Fe-Al-Si alloys better candidates for powder processing than the Fe-Al-Ti alloys.

Powder Solidification

The powder cell size was reduced by the addition of silicon to Fe-15Al. A good review of the rapid solidification of alloy powders is given by Cohen, Kear and Mehrabian [2]. Figure 4.1 shows the competition between the temperature gradient and the velocity of the growth front. At high temperature gradients, G (K/cm), and low growth velocity, R (mm/sec), the planar growth front is preserved. At the other extreme, the low temperature gradient and high growth velocity produce the conditions for dendrite growth. Between these extremes, a cellular solidification develops, which is observed in Figure 3.9 from the HPGA powders produced during this investigation. The break down of the planar front is promoted by localized solute gradients. The addition of 15 atomic % aluminum to iron produces these solute gradients during solidification, but the addition of silicon develops solute gradients which further refine the structure. Typically, the chemical homogeneity is decreased as the number of components increased. In addition, the silicon content may have changed the surface energy of the solid-liquid interface, which may increase the nucleation rate to also refine the structure. The refined structure within each powder particle of the Fe-Al-Si alloys was expected to increase the densification rate during vacuum sintering.

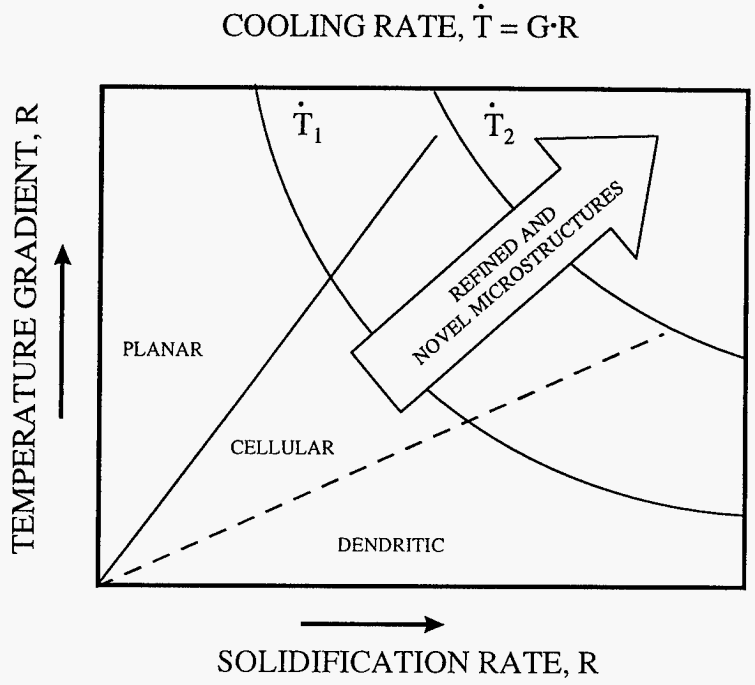

Figure 4.1 - Relationship of Cooling rate and Microstructure [2]

Sintering Densification

We have observed that the addition of silicon to Fe-15Al results in a reduction of the densification rate at temperatures ranging from 1200°C to 1300°C. The densification rates at 1200°C as a function of time clearly show the retarding effect of silicon on densification for both levels of Si that were studied. German [35] reviews the common sintering models at all stages, beginning with the neck formation in the early stages of sintering to minimize the curvature of touching particles. The initial stage of sintering is dominated by surface diffusion and little densification occurs during this stage. The intermediate stage accounts for the majority of the densification as the theoretical densities increase from approximately 65% to 92%. Grain boundary diffusion and lattice diffusion are the primary mechanisms for transporting vacancies from internal pores to the exterior of the compact for consolidation. Effective consolidation during the final stage of sintering is heavily dependent on grain boundary diffusion to eliminate the remaining porosity. Since porosity acts as a restraining force to grain growth, the grain size can increase as the size and volume of pores decrease. The grain boundaries move through remaining pores, and leave them isolated in the grain interior. The pores isolated in grain interiors must be eliminated by lattice diffusion, which is

typically 2 to 3 orders of magnitude less than grain boundary diffusion. If the pores contain residual gas from the sintering environment, they may be stabilized by internal gas pressure.

The driving force contributions for sintering are capillary effects from curvature, reduction in free surface area, reduction in surface energy (γ_{SV}), reduction in grain boundary area and grain boundary energy (γ_{GB}) which promote grain growth. As stated previously the reduction of curvature by neck formation and growth occurs by surface diffusion during the initial stages of sintering. Although the majority of densification occurs during the intermediate stage sintering, the effects a diminished initial stage sintering will affect the subsequent stages. Therefore, a good portion of discussion will examine the contributions of anisotropy in surface energy, which affects the overall sintering densification and the grain growth behavior.

A major difference was observed in the SEM surface topography of vacuum sintered powders of Fe-15Al and Fe-15Al-xSi. The distinct angular faceting observed in the alloys with silicon was attributed to the change in surface energy, γ_{SV} , as a function of crystallographic orientation. The change in surface energy an be calculated by equation [4.1], which accounts for the number of broken bonds along the plane of interest at an angle θ along the close packed plane with interatomic distance, a, and bond energy, ε [37].

$$\gamma(\theta) = \gamma_o \cos\theta + (\varepsilon/a)\sin\theta \qquad [4.1]$$

Sundquist [38] developed a stereographic triangle for BCC metals, and experimentally determined the γ_{SV} as a function of planar orientation. Sundquist measured the dimensions of single grain particles on the order of 1 μm by SEM, and he used the Wulff construction to determine the relative surface energies shown in Figure 1.9. In BCC iron a relative surface energy minimum of γ_{hkl}/γ_o = 0.809 was observed on the (110) planes. Since the Fe-15Al-Si alloys showed such a pronounced faceting on many low index planes, a number of low energy cusps would be present in the γ-plot as a function of crystallographic orientation for these alloys.

If facets on low energy planes effectively reduced the local surface energy, and the surface area remained constant, then the total free energy of the sintered sample would be reduced proportional to the relative surface energy reduction. Consequently, the driving force for densification would be reduced, and therefore the densification rate would be reduced. If we use the example of BCC iron, a faceted which exposed all low energy γ_{SV} orientations at the surface would

reduce the total surface energy by 20% without any change in surface area. If the surface energy had no orientation dependence, the powder surface area would have to be reduced by 20% during neck formation between touching particles to produce the same total surface energy reduction as faceting. Although surface area reduction occurs in the initial stage of sintering contributes only a minor amount to densification, the grain boundaries are formed between particles to establish paths of high vacancy transport for further consolidation. As soon as the grain boundaries form, the densification accelerates due to the high diffusion paths. The SEM surface topography of Figure 3.15, Figure 3.16 and Figure 3.17 shows these differences between the early neck formation and increases in densification rate. Although the initial densification was retarded by the presence of silicon, the overall densification eventually achieved the same level as the binary alloys. Figure 3.11 shows sintering experiments comparing the densification of the Fe-15Al, Fe-15Al-2.8Si and Fe-15Al-5Si powder alloys, which revealed that all alloys achieved the same theoretical density after 20 hours at 1200°C.

Grain Growth

The addition of silicon to Fe-15Al was observed to promote grain growth. The effect was primarily attributed to the anisotropic grain boundary energy, γ_{GB}, which is related to the anisotropic surface energy described previously. The grain boundary energy is a function of the misorientation angle between adjacent grains [21]. In a pure metal the grain boundaries reach a maximum energy at a tilt angle of approximately 15°. However, a semi-coherency between adjacent grains with specific crystallographic relationships can also reduce the grain boundary energy. Figure 1.11 shows specific high angle boundaries with a coincident site lattice (CSL) matching across the boundary have been shown to have a low energy configuration [21]. In fact, Shewmon [41] has shown that during the sintering of unconstrained copper powder particles on a copper plate, the particles will rotate to a preferred grain orientation. In a sintered aggregate, the powder particles have the constraint of multiple adjacent particles, and do not have the freedom to rotate to accommodate each adjacent particle. Therefore, the grain boundaries must minimize their energy by grain growth. The mean grain boundary energy, γ_{GB}, for α-iron is given by Shewmon [41] as 520 ergs/cm^2 compared to a surface energy, γ_{SV} , of 2090 ergs/cm^2. This difference indicates the strong driving force for sintering to eliminate free surface. The low energy boundaries such as incoherent twins have been measured with an energy of 430 ergs/cm^2. The low energy CSL grain boundaries mimic the configurations of incoherent twin boundaries, and therefore have similar energy values. Mullins [41] has observed that

a grain boundary energy difference $\Delta\gamma_{GB} > 0.03\ \gamma_{GB}$ sustains grain growth, but a grain boundary energy difference of $\Delta\gamma_{GB} < 0.015\ \gamma_{GB}$ will not sustain grain growth.

Grain growth studied during secondary recrystallization can provide insight into potential low energy grain boundary configurations developed during sintering. Although the grain growth observed during secondary recrystallization is not completely random as is the case for grain growth observed during sintering, both phenomena are strongly affected by the grain boundary energy. The phenomena of secondary recrystallization in Fe-5Si at.% was observed to prefer the grain boundary along [100] planes [41]. Secondary recrystallization occurred in cold rolled sheet after primary recrystallization. Since the cold work driving grain growth was eliminated, the grain boundary anisotropy drives grain growth. However, the typical high angle grain boundaries resulting from primary recrystallization have a relatively high energy, so secondary recrystallization produces low energy grain boundaries which further reduced the free energy of the system. In addition to the CSL boundaries described by Figure 1.11, the addition of silicon to iron promotes a strong "cube-oriented" texture. The silicon addition to Fe-15Al no doubt has a similar effect, which induces exaggerated grain growth to develop preferred low energy boundaries due to anisotropy in grain boundary energies. The large grains reduce toughness and yield strength of a material by reducing the number of dislocation sources. A large grain permits the easy propagation of cleavage cracks along the cleavage planes. A fine grain size will generate more dislocations in a ductile material to impede crack propagation and interrupt the crack propagation at the grain boundaries of brittle materials.

The potential restraining forces for grain boundary growth are solute drag, inclusions and porosity. The impurity drag is a major concern for species which have a low solubility in the matrix. These impurity atoms are rejected to the grain boundaries to produce much higher concentration, which can impede grain growth by a few orders of magnitude at a very low level. The aluminum or silicon atoms have a high solubility in iron, and therefore would not be probable to exhibit a strong solute drag effect. The more likely restraining forces are associated with the oxides particle pinning and the pinning due to porosity. Zener [39] has developed an expression for the grain boundary pining force due to the particles. Assuming the 300 ppm oxygen was converted into $FeAl_2O_4$, the volume fraction of the 1 μm particles observed by SEM would be less than 0.5%. Obviously, the 10 volume % porosity would have a larger pinning effect than the negligible volume fraction of oxides. The intentional introduction of fine particles such as oxides, carbides and borides can have the benefit of limiting grain growth. Porosity also has the effect of pinning grains to prevent growth.

The Zener equation has been modified shown in equation [4.2] specifically for the case of porosity pinning grain growth during sintering, where G is the grain size, d_p is the pore diameter, V_p is the pore volume, R is a pore attachment ratio and g is a geometric constant.

$$G = \frac{gd_p}{RV_p} \qquad [4.2]$$

Shaw [40] developed a Γ ratio relationship between grain growth and the surface energy,γ_{SV},, grain boundary energy, γ_{GB}, and breakaway grain growth occurs shown in Figure 1.10. As the Γ ratio increases the level of porosity at which breakaway grain growth occurs will decrease. Equation [4.3] indicates that a high γ_{GB}/γ_{SV} ratio will increase Γ ,and therefore promotes grain growth. The grain boundary orientations with the highest γ_{GB}/γ_{SV} ratios will grow by consuming other grains. According to equaiton [4.3], a reduction in γ_{SV} would produce an increased G ratio and promote grain growth regardless whether the material exhibited grain boundary anisotropy. Although the Fe-15Al powder sinter sample had a low level of porosity, the grain growth rates were slower than the Fe-15Al-5Si sintering sample with a higher level of porosity. This reflects the influence of the reduced γ_{SV} with silicon additions.

$$\Gamma = \frac{D_S\gamma_{GB}}{300D_{GB}\gamma_{SV}} \qquad [4.3]$$

Extrusion and Texture

Barret and Levinson [27] demonstrated the development of the {110} wire texture with the swaging of single crystal iron. The rotation of {110} slip planes toward the working direction was responsible for the texture. Similar results have been reported by Khadkikar et al. [29] from the hot extrusion of Fe-40Al. Stouts and Crimp [30] reported two different textures for extruded Fe-35Al which developed depending on whether the starting material was powder or was a cast ingot. The powder developed a {110} texture, while the cast ingots developed a {111} texture from the extrusion. Stouts and Crimp examined the recrystallization textures by x-ray diffraction and orientation image mapping using the SEM technique of Dingly [31]. The major differences in the recrystallization behavior were due to the interaction of the grain boundaries with prior particles boundaries in the powder.

The extruded materials examined in this investigation developed fully equiaxed grain structures resulting from recrystallized grains, which had grown through the prior particle boundaries as shown in Figure 3.23. Although the prior particle boundaries may play a role in the fracture of the samples taken in the longitudinal orientation, they were not suspected to affect the texture development. The prior particle boundaries were not suspected of playing a large role in the punch testing in the transverse orientation, because of the small aspect ratio of the particles with the intersection of the surface.

The [110] pole figures in the longitudinal direction of each powder alloy extrusion revealed a large peak in center of the map. The Fe-15Al and Fe-15Al-2.8Si had a slightly higher (14.6) relative intensity peak ratio than the Fe-15Al-5Si extrusion (6.5). This may be due to the relative ease of slip for the different alloys at the extrusion temperature of 1000°C. The higher silicon content may have an effect on the slip even at 1000°C. The wire drawing of BCC metals has been shown by Levy to produce a [100] circumferential texture in addition to the [110] wire texture. The x-ray diffractometer scan comparing the Bragg reflections of the longitudinal and transverse orientations, shown in Figure 3.35, indicate the strong [110] wire texture, but do not conclusively reveal a [100] circumferential texture. However, the analyzed surface did not represent atomic planes tangential to the radius, but atomic planes an array of angles from the flat surface through the center of the extrusion. Figure 4.2 shows the difference between an exterior sample labeled as "A", an mid-radius

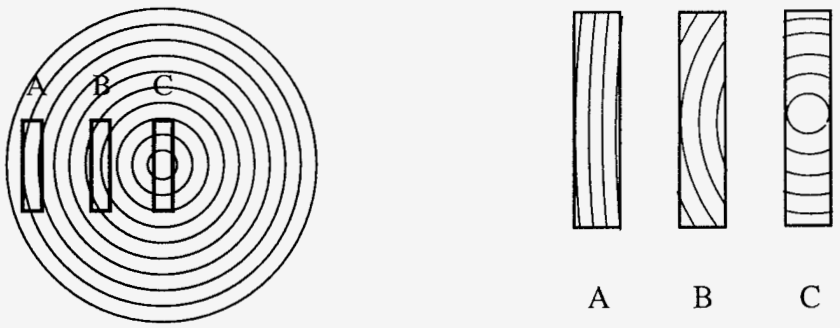

Figure 4.2 - Circumferential texture effect on punch disks texture with radial distance

sample labeled as "B" and a central sample labeled as "C". The wide variety of the circumferential orientations represented by a flat sample illustrate the difficulty of measuring the circumferential texture in a large cross section work piece. The extrusion texture was expected to affect the tensile yield strength. However, the punch test yield strength probably was measured from samples taken at

different orientation relationships to the extrusion direction, and hence did not exhibit a consistent effect of the extrusion texture.

Order-Disorder Phase Equilibrium

Many investigators have observed the strong ordering effect of silicon additions to iron aluminum alloys. The ternary alloy system of Fe-Al-Si alloys has been well examined by Miyazaki [17] and is shown in Figure 1.5. Mendiratta and Lipsitt [5] demonstrated the increase in the order-disorder transition temperature with additions of Si and Ti. Fortnum and Mikkola [4] showed the improvement of creep rupture life at 600°C with the addition of Ti and Si to multi-component cast alloys due to the increased stability of the DO_3 phase. Recently, Morris and Gunther [18] have examined the phase equilibrium of alloys with a potential for structural applications. They have noted a special interest in the development of stable two phase alloys with a coherent interface. The alloys investigated in this study consist of a pure BCC solid solution strengthened Fe-15Al alloy, a slightly ordered Fe-15Al-2.8Si alloy and a strongly ordered Fe-15Al-5Si alloy. Although the degree of order was not quantified, the qualitative degree of order can be observed by the relative strength of the fundamental reflections compared to the superlattice reflections. Figure 3.27 show the faint superlattice spot for the 111 and 200 reflections. However, the long exposure times to reveal the very faint superlattice reflections indicate a small volume fraction of DO_3 phase. In contrast, the black background in Figure 3.27(a) indicate strong superlattice reflections and a large volume of DO_3 ordered phase as shown in Figure 3.28.

The effect of increasing temperature was to disorder the alloys by increasing the entropy component of the free energy, $\Delta G = \Delta H - T\Delta S$. The DO_3 compound in extruded Fe-15Al-2.8Si alloy was observed by electron diffraction to disorder to α between 400°C and 600°C. The DO_3 compound was stable in the Fe15Al-5Si alloy up to at least 600°C, but transformed into the B2 compound at 800°C. According to the pseudo-binary Fe_3Al-Fe_3Si diagram, the B2 compound should disorder above 1000°C. The atom sites for Al and Si on the DO_3 lattice have been shown to be the same by Mossbauer spectroscopy and x-ray diffraction [4]. Therefore, the 8 first-nearest-neighbors iron atoms along the <111> direction and the 6 second-nearest neighbor iron atoms along the <100> directions are more strongly attracted to the silicon than aluminum. Since there are 4 potential sites per lattice for the Al or Si and the atomic ratio of aluminum to silicon was 3 to 1 in Fe-15Al-5Si, a superstructure is possible in which the Si atom occupies the same position in every lattice cell. However, the selected area electron diffraction patterns provided no evidence for a larger superlattice structure.

The concentration of solute atoms, c, the shear modulus of the lattice, G, and the misfit strain of a solute atom, ε_s, produce an increase in the shear stress required to move a dislocation. The silicon and aluminum in solid solution α contributed a strengthening effect described by equation [4.4] which was developed by Fleischer [42].

$$\Delta\tau_{sol} = \frac{G\varepsilon_s^{3/2}c^{1/2}}{700} \qquad [4.4]$$

The atomic radii of the atoms involved are the following: aluminum is 1.43 angstroms, silicon is 1.32 angstroms and iron is 1.27 angstroms. Equation [4.4] predicts an increase in flow stress of 19% for each additional atomic % of aluminum, but silicon is predicted to increase the flow stress by 6% for each atomic percent. The punch tests reveal that silicon is a much more potent strengthening addition than aluminum. Therefore, factors other than atomic size increase the flow stress, such as the short range interaction. The influence of silicon on the ordering stability implies a stronger short range atomic interaction even without the formation of ordered phase.

After intermetallic particles form in the matrix, the strengthening mechanism changes. The size and distribution of the intermetallic phases determined the interaction with dislocations. The small ordered precipitates in as-extruded Fe-15Al-2.8Si could be treated as small particles, which may be by-passed or cut. Dislocations which bypass the particles have the following relationship. The increase in shear stress required to bow around a dislocation around immobile objects is given by equation [4.5], where L is the interparticle distance and r is the particle radius.

$$\Delta\tau_B \cong \frac{Gb}{(L-2r)} \qquad [4.5]$$

The energy for a dislocation to move through an ordered intermetallic compound is given by equation [4.6]. The energy create by a dislocation passing through a particle is a function of the cross sectional area, f, of the particles, and the anti-phase boundary energy (APBE) of the slip plane through the intermetallic phase.

$$\Delta\tau_{ord} = \frac{\pi(APBE)f}{2b} \qquad [4.6]$$

Both equations [4.5] and [4.6] require an accurate knowledge of the volume fraction, precipitate size and the measurement of the APBE. The measurement of APBE for each alloy requires an intensive TEM investigation, which was beyond the scope of this work. The addition of silicon appear to reduce the dislocation mobility, so it appears the DO_3 phase was bypassed. As the volume fraction of DO_3 phase increased as observed in Fe-15Al-5Si the 600°C heat treatment, the mechanical property behavior was dominated by the ordered DO_3 phase which exhibited cleavage.

Mechanical Properties

The influence of silicon on the mechanical properties was primarily due to the influence of solid solution strengthening, increased ordering and decreased cleavage strength. As the degree of order increased, the tendency of Mode I cleavage increased. The TEM micrographs in Figure 3.28 show the "basket weave" DO_3 phase with narrow regions of disordered-α sandwiched between them. The interface between the ordered and disordered phases has been shown to lie along the (001) planes. The boundary can be viewed in either the (001) zone axis or the (110) zone axis with the superlattice reflections (111) or the fundamental reflections (110). If an APB exists on the (100) planes, then the energy for cleavage along those planes may be reduced. However, if an APB resides along the (110) planar interface, the dislocations may travel along the interface to cause failure.

The Fe-15Al-2.8Si punch samples vacuum sintered at 1200°C compared with the samples sintered at 1300°C showed no significant difference in the yield strength, but showed an improvement fracture toughness at all test temperatures as shown in Figure 3.33. This was unexpected, since vacuum sintering at 1200°C had more than 10% porosity compared to only 3% porosity in the sample sintered at 1300°C. However, the grain size developed at 1200°C was 26 μm compared to 76 μm developed at 1300°C. Typically, an increased porosity level reduces the fracture toughness of a structure member [50]. The immediate effect is to reduce the cross-sectional area supporting the load. The pores can act as stress concentration sites from which a crack can propagate. However, in a material with quasi-brittle behavior the pores can blunt cracks to reduce the stress concentration at the crack tip by increasing the tip radius as shown in equation [4.7], where σ_{max} is the localized stress resulting from and applied stress σ_a with a crack length, a, with a tip radius, ρ. As an example a sharp crack may naturally have a tip radius on the order of 10 nm, while a remnant pore from sintering has a radius of 10 μm. For a given crack length, equation [4.7] predicts a reduction in localized stress by a factor of 30.

$$\sigma_{max} = \sigma_a [1+ 2(a/\rho)^{-1/2}] \qquad [4.7]$$

The blunting mechanism can complement the toughness when the dislocation mobility is limited. Grain boundaries provide resistance to transgranular cleavage crack propagation, by requiring additional stress to initiate cleavage in the adjacent grains. If grain boundaries have developed low energy CSL configurations such as those suspected in samples sintered at 1300°C, the stress required to propagate a crack into adjacent grains may also be reduced.

The ductile to brittle transition in BCC metals has been attributed to the lack of mobility of screw dislocations at low temperatures [19]. Microcrack initiation and propagation are impeded by the migration of dislocations to defects to minimize the stress ahead of the crack tip. One of the effects of silicon additions to iron is to restrict dislocation cross slip, which is important for the mobility of screw dislocations. The cross slip becomes more important as the screw dislocations encounter obstacles in the slip planes, such as the order precipitates observed in Fe-Al-Si alloys. Therefore, the silicon additions have a two-fold effect in limiting dislocation mobility. Namely, limiting cross slip by short range atomic interaction and producing small ordered precipitates to block movement.

Slip in BCC Metals

Christian [19,20] reviews the plastic deformation in BCC metals, which is the foundation to understanding the interaction with two phases. The primary slip systems in iron are on the {110} {112} and {321} planes with a [111] slip direction. The macroscopic slip lines along {321} and irrational planes have been shown to consist of {110} and {112} segments. The elastic anisotropy in BCC metals reveals the preference to slip along particular planes. The "A" ratio of elastic constants, $A = 2C_{44}/(C_{11}- C_{12})$, demonstrates the range of elastic anisotropy observed in pure BCC metals. An "A" ratio equal to 1.0 shows no anisotropy, such as in tungsten. Iron has an A ratio equal to 2.4, shows a preference for {110} slip. However, BCC metals such as niobium have an A ratio less than 1.0, and the primary slip plane has been observed as {100}.

The elastic anisotropy is an important consideration in determining the elastic stress field surrounding the core of the dislocation. The local stress field determines the lattice friction stress, which offers resistance to dislocation motion. The yield stress of BCC metals has been observed to be higher in single crystals oriented in the <110> direction compared to the <100> orientation [19] . Schmid's law of critical resolved shear stress has been observed to predict slip planes at higher temperatures in tension, but low temperature behavior has been more unpredictable [20].

Typically, the edge dislocations are mobile on the planes, but the screw dislocations require cross slip onto other planes for mobility [19] . The core of the screw dislocation has been determined to be composed of three partial dislocations with 120° angular separation from each other on the {110} or {112} planes. The extensive cross slip required for screw dislocation mobility is observed on the macroscopic surface as "wavy slip" lines. At low temperatures < 0.2 T_m, the mobility of screw dislocations decreases and the flow stress increases. Experiments by Sestak and Blahavic [19] measured slip planes in single crystal Fe-5 Si at.% to exhibit predominantly {110} slip. The Fe-15Al alloys with silicon would also have restricted cross slip and make the screw dislocations immobile without thermal activation.

The thermal activation is demonstrated in iron based materials by the ductile to brittle transition behavior. Typically, the dislocations are impeded by carbides in steels or the small ordered precipitates in the case of Fe-Al-Si alloys. If the dislocations cannot cut the obstacles or move around them, then cracks are nucleated which result in transgranular cleavage. When the lattice has enough thermal energy, the screw dislocations can cross slip and by-pass the ordered precipitates. Although a thermal activation model proposed by Kameda [57] describes this behavior, the unknown effects of strain rate and dislocation dynamics prevent the quantitative application of his model to the DBTT behavior.

The DBTT in the as-extruded Fe-15Al-5Si was higher than the ordered materials produced by the heat treatment at 600°C. Apparently, the increase volume fraction of DO_3 phase prevented dislocation motion, the temperature dependence of slip in the Fe_3Al compound dominated the mechanical property behavior of Fe-15Al-5Si alloys. Leamy [22] showed that the primary slip system in single crystal Fe-Al alloys, ranging from 15 to 30 Al at.%, was of the <111>(110) type. However, he demonstrated that 6 different combinations of partial dislocations were energetically possible. All dislocations were observed, but they were dependent on the elastic anisotropy of the material at a specific composition and test temperature. The primary finding was that the superdislocations could not cross slip onto (112) or (123) slip planes, but at a higher temperature a/2<111>{110} unit dislocations were observed to be the primary deformation mechanism. The stress required to move the complex superdislocations in the ternary compound was higher than the cleavage strength, and therefore we observe cleavage at room temperature prior to plastic yielding in Fe-15Al-5Si alloys. The heat teament extruded Fe-15Al-5Si increased the punch yield strength approximately 100 MPa at temperatures above 300°C, which indicates the higher energy required for a dislocation to cut through the ordered compounds after heat treatment. However, the difference in

fracture energy of 500 mJ at 300°C indicated the less ordered Fe-15Al-5Si was more effective in absorbing deformation.

Punch and Tensile Yield Strength

The {110} texture developed in all three alloy was responsible for the observed increase in yield strength in uniaxial tension compared to the multi-axial punch test. Since a shear stress is required for the movement of dislocations the lowest yield strength is predicted to be observed when the {110}[111] slip systems are 45° from the tensile axis. Easy slip would occur in a {100} texture with 12 slip systems active at the maximum Schmid factor. When the {110} planes are parallel and perpendicular to the tensile axis the resolved shear stress is zero on those planes. However, four slip systems are active with the slip planes at 60° to the tensile axis, and with the slip direction the 45°. These slip systems may show little microplastic deformation, but may be restricted due elastic incompatibility with adjacent grains. The grains which have the largest misorientation will deform and other slip systems such as the {112} may be activated to alleviate elastic stress incompatibility across grain boundaries. Von Mises and Taylor [43] originally developed the idea that 5 independent slip systems are required to maintain compatibility across high angle grain boundaries in polycrystals. In the absence of 5 independent slip systems, intergranular failure will occur as is observed in many intermetallic compounds. Since only 4 slip systems are activated in a strongly oriented {110} BCC metal, at least one other slip system must be present on satisfy von Mises criteria for grain boundary compatibility. Therefore, a textured material with a majority of grains aligned along the {110} orientation in the tensile direction will have a high flow stress.

Hirsch [58] observed the activation of {112} planes at the grain boundary during the tensile testing of a Fe-5Si bicrystal in the {110} orientations, which is schematically shown in Figure 4.3. The {112} slip system had the lowest Schmid factor, and therefore controlled the magnitude of the yield strength in the bicrystals. If a sufficiently large number of grains are oriented properly with the surface in the highly stressed region of a punch test disk, then slip systems in addition to the {110}<111> must be initiated for plastic flow. Therefore, the resulting yield strength for a {110} textured polycrystalline material in uniaxial tension would increase proportionally. The large dislocation interactions which may occur in certain orientations may also play a role in the larger yield stress values. A extensive analysis by TEM would be necessary to verify the dislocation reactions.

The tensile yield strengths were considerably higher than those measured by the punch specimen. Figure 4.4 shows a plot of the tensile yield strength corresponding to punch yield strength

in the transverse and longitudinal orientations. Most of the punch test samples were taken perpendicular to the extrusion axis, and therefore the {110} type planes would lie parallel to the disk face. High angle grain boundaries were expected based on the differences in rotational symmetry about the circumference. The large difference in etching contrast between adjacent grains observed in Figure 3.23 provides evidence for high angle grain boundaries. However, one might expect to observed punch yield strength values similar to the tensile yield strength values in the orientation parallel to the extrusion axis. Unfortunately, this was only observed in 2 cases out of 10, and the results were strongly dependent on the proximity of the sample to the central axis as is shown in Figure 4.2

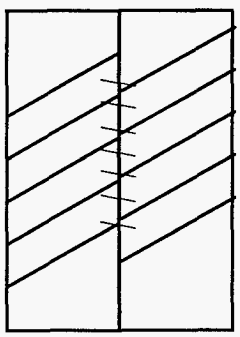

Figure 4.3 - Schematic of (110) slip lines in grains and (211) slip lines observed in bi-crystal Fe-5Si at a low angle grain boundary [58]

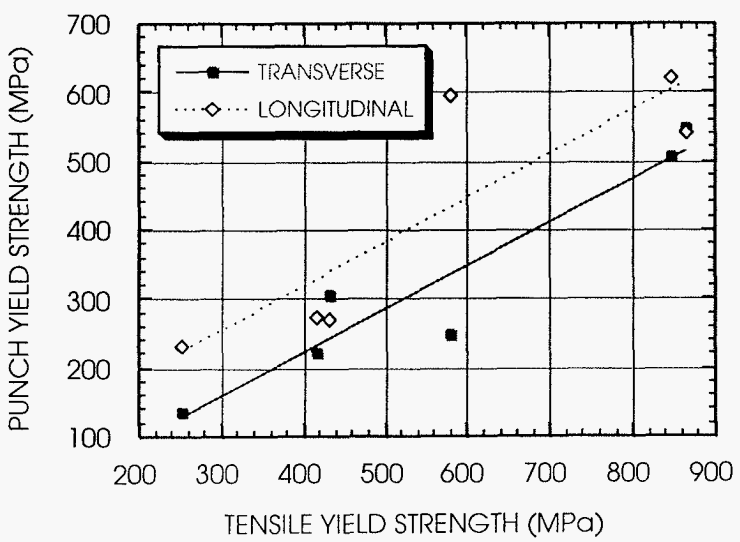

Figure 4.4 - Comparison of tensile and punch testing yield strength in Fe-Al-Si extrusions

One of these conditions was duplicated, and the yield strength values from all tests of a Fe-15Al-5Si extruded alloy tested at 550°C are shown in Figure 4.5. Only the punch yield strength (596 MPa) of the axial sample "A" showed a similar yield strength as the tensile test. The axial sample "B", apparently taken closer to the central axis of the extrusion, had a lower punch yield strength (450 MPa), but not as low as the punch yield strength of the transverse sample (247 MPa). The circumferential texture distributions illustrated in Figure 4.2 are difficult to measure in a large cross section extrusion. However, an orientation image mapping technique with a specially equipped SEM may be used to measure the differences [31].

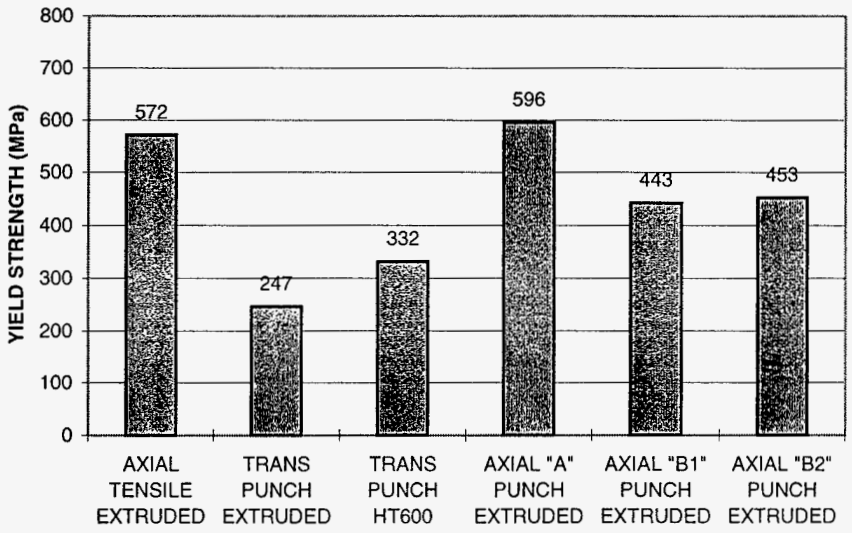

Figure 4.5 - Comparison of yield strength in Fe-15Al-5Si

The localized strain distribution during punch testing probably exacerbated the differences in the yield strengths observed. Another factor in comparing the tensile test yield strengths compared to the punch test yield strengths was the test volume in the tensile sample of 58.42 mm^3 compared to the test volume in the punch sample of 6.28 mm^3. In addition, the inhomogeneity of strain in the punch sample must be considered when examining the yield strength data determined by the punch specimen. A much smaller volume of the punch sample was deformed at the point of plastic yielding than the whole volume tested, as shown in Figure 4.6.

The maximum tensile forces at plastic yielding were on the bottom face of the punch sample at the very center. A volume approximated by a hemisphere with a radius from 50 μm to 250 μm was estimated as the strained material at plastic yielding. This volume was approximately 6.5 x 10^{-2} mm^3 to 2.6 x 10^{-4} mm^3, or a factor of 1.1x10^{-3} to 4.5 x 10^{-6} less than the tensile bar test volume. Since the average grain diameter of these materials was approximately 50 μm, a single spherical grain volume was calculated to be 6.5 x 10^{-5} mm^3. Therefore, as few as 4 grains or as many as 1000 grains were involved in determining the yield strength from the punch disk. The orientations of these grains with respect to each other and the sample surface may have strongly affected the yield strength. Since the extruded samples were strongly textured, the probability the central surface grains were of similar orientation was high.

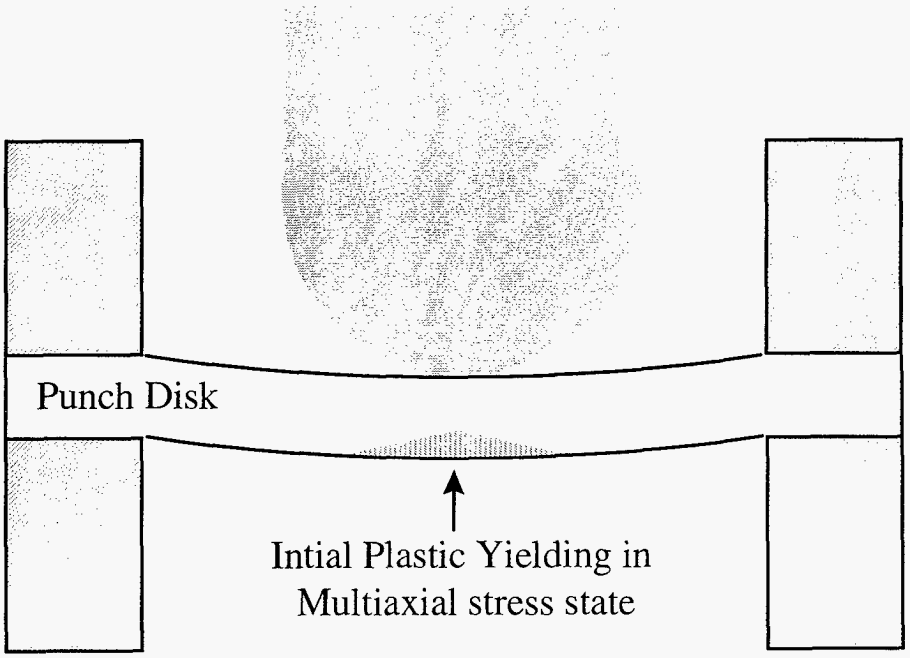

Figure 4.6 - Punch disk volume plastically deformed at yield strength

CHAPTER 5. CONCLUSIONS

The addition of silicon to Fe-15Al at.% produced faceting on powder particle surfaces during vacuum sintering above 1200°C. The faceting planes occurred on the low index planes with high symmetry. The faceting was due to a change in the solid-vapor surface energy, γ_{sv}, as a function of crystallographic orientation. The γ_{sv} anisotropy in Fe-Al-Si alloys reduced the densification rate at early stages of sintering, but after 10 hours of exposure at 1200°C the effect was indistinguishable. The addition of silicon to Fe-15Al also promoted grain growth at elevated temperatures, which suggests that the grain boundary energy was affected by the silicon additions.

The addition of silicon to Fe-15Al at.% increased the yield strength from room temperature to 550°C, which indicates an increase in flow stress for the principle slip system. The silicon addition increased the volume fraction of the DO_3 phase, and increased the phase stability to higher temperature as observed by TEM at elevated temperatures. The DBTT was raised with the increase volume of the DO_3 phase. In addition, silicon additions promoted transgranular cleavage by lowering the cleavage strength below the dislocation flow stress. At temperatures above 300°C, the Fe-15Al-5Si alloy deformed plastically, and produced a yield strength approximately 200 MPa higher than the Fe-15Al alloy.

The extrusion of Fe-Al-Si alloys produced a {110} wire texture, which nearly doubled the yield strength of the material in the extrusion direction compared to the transverse direction. Although the extruded alloy was fully dense, the tensile properties in the extruded direction do not represent the mechanical properties of a sintered microstructure with randomly oriented grains. The yield strength of sintered powders was comparable to the extruded powders in the same heat treatment condition. The yield strength and fracture energy of the fine grain (30 μm) material with approximately 10% porosity exceeded the yield strength and fracture energy of coarse grain (75 μm) material with approximately 3% porosity. Therefore, the processing parameters are broad enough to develop desirable mechanical properties with a wide range of microstructures. The next phase of development would be to incorporate these processing parameters into an MIM process to address the interaction of the powder with binder systems. The uniform porosity and fine grain size of the sintered Fe-15Al-2.8Si alloy, which was heat treated at 600°C, developed the best combination of strength and toughness. This indicates the silicon atoms are more beneficial in a solid solution rather than in an ordered precipitate.

The potentially wide variety of microstructures which could develop during MIM processing would have similar mechanical properties. The variation in mechanical properties of a given part may be directly measured using the small punch test. The small punch test successfully measured the differences in the yield strength and fracture energy of alloys and heat treatments of sintered parts. The punch test may be used on MIM parts at specific locations on the part, to measure the mechanical property variation in a part. The punch test was an accurate and consistent method for the testing of the DBTT phenomena of the various alloys and heat treatments. However, the texture effects on the yield strength were difficult to isolate, because of the multi-axial stress state of the small punch test.

A number of important questions remain to be answered for the Fe-Al-Si alloys to be useful as engineering materials. The stability of the solid solution silicon at temperatures ranging from 200°C to 500°C. If the silicon were to cause local ordering, then the material may become embrittled. The addition of chromium might provide the same ductilizing benefit to Fe-Al-Si that it has shown with the Fe-28Al alloys. Chromium might provide the additional benefit of reducing the ordering kinetics to make the Fe-Al-Si more stable, and further improve the oxidation resistance.

The grain growth effect of silicon presents a few other interesting questions. For instance: What are the grain boundary configurations which are produced during coarsening? Do these low energy configurations have less resistance to crack propagation across a grain boundary? How can the grain coarsening phenomena be inhibited without adversely reducing the densification? The miniaturized testing of crystallographically textured structures is an area of interest. A future investigation may use a test technique which produces a more uniaxial stress state, such as a 4-point bend test to activate the slip systems with specific orientation relationships to the sample geometry.

REFERENCES CITED

1. C.G. McKamey, J.H. DeVan, P.F. Tortorelli and V.K. Sikka, "A Review of Recent Developments in Fe_3Al-based Alloys", *Journal Material Research*, Vol. 6, No. 8, Aug. 1991, pp.1779-1805.

2. M. Cohen, B.H. Kear, and R. Mehrabian, "Rapid Solidification Processing - An Outlook," *Rapid Solidification Processing: Principles and technologies II,* Claitor's Publishing, Baton Rouge, LA, 1980, pp. 1-23.

3. V.K. Sikka, R.H. Baldwin, C.R. Howell and J.H. Reinshagen, "Powder Production, Processing and Properties of Fe_3Al", *Advances in Powder Metallurgy and Particulate Materials*, Metal Powder Industries Federation, Princeton, NJ, Chicago, 199, pp. 343-356.

4. R.T. Fortnum and D.E. Mikkola, "Effects of Mo, Ti and Si Additions on the $DO_3 \rightarrow B2$ Transition Temperature for Alloys near Fe_3Al", *Materials Science and Engineering*, vol. 91, 1987, pp.223-231.

5. S.V. Thamboo, G.W. Powell and J.P. Hirth, "Microstructure-Property Correlations for Rapid-Solidification-Processed Fe-Si-Al Alloys," International Journal of Powder Metallurgy and Powder Technology, Vol. 21 No. 4, 1985, pp. 283-301.

6. W.E. Boggs, "The High Temperature Oxidation Resistance of Iron-Aluminum-Silicon Alloys", *Oxidation of Metals*, Vol. 10, No. 4, 1976, pp. 277-289.

7. C.G.McKamey and C.T. Liu, "Iron Aluminide alloys with improved Properties for High Temperature Applications," US patent 4,961,903, 1990.

8. C.T. Liu, C.G. McKamey and E.H. Lee, "Environmental Effects on Room Temperature Ductility and Fracture in Fe_3Al," *Scripta Metallurgica*, Vol. 24, 1990, pp. 385-390.

9. N.S. Stoloff, "Chapter 3: Fundamentals of Strengthening," *Superalloys II*, ed. C.T. Sims, N.S. Stoloff and W.C. Hagel, John Wiley & Sons, New York, NY, 1987, pp. 61-95. -

10. U. Kattner, "Volume 3: Alloy Phase Diagrams," *ASM Metals Handbook 10^{th} edition*, ASM International, Metals Park , OH, 1992, p. 244.

11. P.R. Swann, W.R. Duff, R.M. Fisher , "The Electron Metallography of Ordering Reactions in Fe-Al Alloys," *Metallurgical Transactions A*, Vol. 3, 1972, pp. 409-419.

12. A. Taylor and R.M. Jones, "Constitution and Magnetic Properties of Iron-rich Iron-Aluminum alloys", *Journal of Physics and Chemical Solids*, Vol. 6, 1958, pp. 16-37.

13. A. Lawley and R.W. Cahn, "A High Temperature X-ray study of Ordering in Iron-Aluminum alloys", *Journal of Physics and Chemical Solids*, Vol. 20, No. 3/4, 1961, pp. 204-221.

14. S.M. Allen and J.W. Cahn, "Coherent and Incoherent Equilibria in Iron-rich Iron Aluminum Alloys," *Acta Metallurgica*, Vol. 23, 1975, pp. 1017-1026.

15. B.D. Cullity, *Elements of X-ray Diffraction*, 2nd edition Addison Wesley, Reading, MA, 1978, pp. 121-126.

16. V.E. Polishchuk and Y.P. Selisskii, "Pseudo-binary Equilibrium Phase Diagram of Fe_3Al-Fe_3Si", *Ukralnskii Fizicheskii Zhurnal*, Vol.**14**, No. 10, 1969, pp. 1722-1724.

17. T. Miyazaki, T. Kozakai and T. Tsuzuki, "Phase decomposition of Fe-Si-Al ordered Alloys", *Journal of Material Science*, Vol. 21, 1986, pp. 2557-2564.

18. D.G. Morris and S. Gunther, "Order-Disorder Changes in Fe_3Al phased Alloys and the Development of an Iron-base α–α" Superalloy", *Acta Materiallurgica*, Vol. 44 No. 7, 1996, pp. 2847-2859.

19. J.W. Christian, "Keynote Lecture: Plastic Deformation of BCC Metals," Second International Conference on The Strength of Metals and Alloys, ASM, Metals Park, OH, 1970, pp. 31-70.

20. J.W. Christian, "Some Surprising Features of the Plastic Deformation of Body-Centered Cubic Metals and Alloys," *Metallurgical Transactions A*, Vol. 14A, 1983, pp. 1237-1256.

21. T.H. Courtney, *Mechanical Behavior of Materials*, McGraw Hill, New York, MA, 1990, pp. 178-191.

22. H.J. Leamy, "The Plastic Deformation of Long Range Ordered Iron-Aluminum Alloys", PhD. Thesis, Iowa State University, 1967.

23. N.S. Stoloff and R.G. Davies, "The Plastic Deformation of Ordered FeCo and Fe_3Al Alloys", Acta Metallurgica, Vol.12, May 1964, pp. 473-485.

24. C.G. McKamey, J.A. Horton, and C.T. Liu, "Effect of Aluminum Addition on Ductility and Yield Strength of Fe_3Al Alloys with 0.5wt% TiB_2", *High Temperature Ordered Intermetallics II*, ed. N.S. Stoloff, C.C. Koch, C.T. Liu, O. Izumi, Materials Research Society, Boston, MA, Vol. 81, pp. 321-327.

25. R.W. Armstrong, "Chapter 1: Strength Properties of Ultrafine-Grain Metals", *Ultrafine Grain Metals,* ed. JJ. Burke and V. Weiss, Syracuse Press, 1970, pp. 1-28.

26. Steven Reichman and David S. Chang, "Chapter 17: Powder Metallurgy," *Superalloys II*, ed. C.T. Sims, N.S. Stoloff and W. C. Hagel, John Wiley & Sons, New York, NY, 1987, p. 473.

27. C.S. Barret and L. H. Levinson, "Structure of Iron after Drawing, Swaging, and Elongating in Tension," *AIME Transactions*, Vol. 135, 1939, pp. 296-302.

28. S. Leber, "Cylindircal Textures in Tugsten and other Body Centered Cubic Metals," *Transaction of ASM*, vol. 53, 1961, pp. 697-713.

29. P.S. Khadkikar, G.M. Michel and K.V. Vedula, "Preferred Orientations in Extruded Nickel and Iron Aluminides", *Metallurgical Transactions A*, vol. 21A, 1990, pp.290-304.

30. J. Stout, "Texture and Bimodal Grain Growth in B2 FeAl Alloys," M.S. Thesis, Michigan State University, 1992.

31. D.J. Dingley, "Interpretation of Electron Backscatter Pattern," *Scanning Electron Microscopy*, 1981, pp. 273-279.

32. R.M. German, *Powder Metallurgy Science*, MPIF, Princeton, NJ, 1994, pp. 192-201.

33. Charles W. Finn, "Vacuum Binder Removal and Collection", *International Journal of Powder Metallurgy*, Vol. 27, No. 2, 1991, pp. 127-132.

34. R.L Mackey and R.B. Patterson, "The Effect of Particle Size and Volume Fraction on Powder Volume Concentration Powder Metallurgy Injection Molding Feedstock," *Progress in Powder Metallurgy,* Vol. 43, 1987, pp. 843-857.

35. R.M. German, *Sintering Theory and Practice,* John Wiley & Sons, New York, NY, 1995, p. 107.

36. J.D. Verhoeven, *Fundamentals of Physical Metallurgy*, John Wiley & Sons, New York, NY, 1975, p. 155.

37. P.G. Shewmon and W.M. Robertson, Chapter 3 - "Variation of Surface Tension with Orientation", *Metal Surfaces: Structure, Energetics and Kinetics*, ASM, Metals Park, OH, 1963, pp. 67-98.

38. B.E. Sundquist, "A Direct Determination of the Anisotropy of the Free Surface Energy of Solid Gold, Silver, Copper, Nickel, Alpha and Gamma Iron," *Acta Metallurgica*, vol. 12, 1964, p. 67.

39. R.M. German, *Sintering Theory and Practice,* John Wiley & Sons, New York, NY, 1995, pp. 95-125.

40. N.J. Shaw, "Densification and Coarsening During solid State Sintering of Ceramics: A review of the Models. III. Coarsening," *Powder Metallurgy International*, vol. 21., no. 6, pp. 25-29.

41. P.G. Shewmon, Chapter 5 - "Energy and Structure of Grain Boundaries", *Recrystallization, Grain Growth and Textures*, ASM, 1966, pp. 165-198.

42. T.H. Courtney, *Mechanical Behavior of Materials*, McGraw Hill, 1990, pp. 178-191.

43. M.A. Meyers and K.K. Chawla, *Mechanical Metallurgy: Principles and Applications*, Prentice-Hall, Princeton, NJ, 1984, pp. 338-341.

44. C.T. Liu, C.L. White, J.A. Horton, "Effect of boron on Grain-boundaries in Ni_3Al", *Acta Metallurgica*, Vol. 33, No. 2, 1985, pp.213-229.

45. P.S. Khadkikar, K.Vedula and B.S. Shabel, "The Role of Ductilizing Ni_3Al", *Metallurgical Transaction A*, Vol. 18A, 1987, pp. 425-428.

46. C. Ghandi and M.F. Ashby, "Fracture-Mechanism Maps for Materials which Cleave: FCC, BCC, and HCP Metals and Ceramics," *Acta Metallurgica*, Vol. 27, pp. 1565-1602.

47. N.S. Stoloff and C.T. Liu, "Review: Environmental Embrittlement of Iron Aluminides," *Intermetallics*, Vol. 2, 1994, pp. 75-87.

48. M.J. Marcinkowski, M.E. Taylor and F.X. Kayser, "Relationship between atomic ordering and fracture in Fe-Al Alloys," *Journal of Materials Science*, Vol. 10, 1975, pp. 406-414.

49. R.W. Hertzberg, "Chapter 8: Elements of Fracture Mechanics", *Deformation and Fracture Mechanics of Engineering Materials*, 4th ed, John Wiley & Sons, New York, NY, 1996, pp. 352-386.

50. A.S. Wagh, J.P. Singh, R.B. Poeppel, "Dependence of Ceramic Fracture Properties on Porosity," *Journal of Material Science*, Vol. 28, 1993, pp. 3589-3993.

51. R.O. Ritchie and A.W. Thompson, "On Macroscopic and Microscopic Analyses for Crack Initiation and Crack Growth Toughness in Ductile Alloys", *Metallurgical Transactions A*, Vol. 16A, February 1985, pp. 233-246.

52. P.D. Prichard, J. Kameda and I.E. Anderson, "The Structure-Property Relationship of Powder Processed Fe-Al-Si Alloys," *Advances in Powder Metallurgy and Particulate Materials - 1997*, Metal Powder Industries Federation, Princeton, NJ, 1997, pp. 7-162 to 7-177.

53. J. Kameda and X. Mao, " Small-Punch and TEM-disc Testing Technique and their Application to Characterization of Radiation Damage", *Journal of Material Science,* Vol. 27, 1992, pp. 983-989.

54. X. Mao and H. Takahashi, *Journal of Nuclear Materials*, Vol. 150, 1987, pp. 42-50.

55. G.E. Lucas, " Review of Small Specimen Test Techniques for Irradtiation Testing", *Metallurgical Transactions A,* vol. 21A, May 1990, pp. 1105-1119.

56. J.R. Foulds, P.J. Woytowitz, T.K. Parnell and C.W. Jewett, "Fracture Toughness by Small Punch Testing," *Journal of Testing and Evaluation*, Vol. 3, No. 1, 1995, pp. 3-10.

57. J. Kameda, "A Kinetic Model for Ductile-Brittle Fracture Mode Transition Behavior ," *Acta Metallurgica*, Vol. 34, No. 12, 1986, pp. 2391-2398.

58. J.P. Hirth, "The Influence of Grain Boundaries on Mechanical Properties," *Metallurgical Transactions*, Vol. 3, 1972, pp. 3047-3067.

ACKNOWLEDGEMENTS

I would like to thank the basic Energy Sciences division of the US Department of Energy for supporting this work under contract no. W-7405-Eng-82 thesis number IS-T 1832. I am grateful to Arne Swanson for conducting the punch testing, and Dr. Jun Kameda for his many discussions related to the merits and fallibility of the small punch test. I would like to thank Professor Scott Chumbley and Fran Laabs for their assistance with the transmission electron microscopy conducted on these materials. The wisdom and humor of Professor Otto Buck has been invaluable during this experience. I have a heartfelt appreciation for Professor Iver Anderson, who has extended great patience, encouragement and confidence in me during the progress of this research.

Report Number (14) FS-T--1838

Publ. Date (11) 19980223

Sponsor Code (18) DOE/ER, XF

UC Category (19) UC-400, DOE/ER

DOE